

UCLA

UCLA Electronic Theses and Dissertations

Title

Selective Area P-type Doping in Gallium Nitride Using Ion Implantation for High Power Applications

Permalink

<https://escholarship.org/uc/item/2fs0w7vt>

Author

Wang, Yekan

Publication Date

2022

Peer reviewed|Thesis/dissertation

UNIVERSITY OF CALIFORNIA

Los Angeles

Selective Area P-type Doping in Gallium Nitride Using Ion Implantation for High Power
Applications

A dissertation submitted in partial satisfaction of the
requirements for the degree Doctor of Philosophy in
Materials Science and Engineering

by

Yekan Wang

2022

© Copyright by

Yekan Wang

2022

ABSTRACT OF THE DISSERTATION

Selective Area P-type Doping in Gallium Nitride Using Ion Implantation for High Power Applications

by

Yekan Wang

Doctor of Philosophy in Materials Science and Engineering

University of California, Los Angeles, 2022

Professor Mark S. Goorsky, Chair

Magnesium ion implantation and subsequent activation annealing shows promise as an effective p-type doping method in Gallium Nitride (GaN). This dissertation relates implant-induced defects and the electrical performance. The implantation process introduces an elastic strain purely orthogonal to the (0001). Complete strain recovery is achieved by annealing at 1300 °C for 10 min (one GPa N₂ overpressure) for dose level up to 1×10^{15} cm⁻². However, extended defects such as stacking faults, dislocation loops, and inversion domains form during the anneal. Critical extended defects in the form of inversion domains were found to contain electrically inactive Mg after annealing at temperatures of 1300 °C (one GPa N₂ overpressure), which results in a low dopant

activation efficiency. A key finding of this work was to demonstrate that annealing at temperatures above 1300 °C eliminates the presence of the Mg-rich inversion domains. While other residual defects, such as dislocation loops, still exist after annealing at and above 1400 °C, chemical analysis shows no sign of Mg segregation at dislocation loops or other defects. Meanwhile, an overall decreasing trend in the dislocation loop size and density is observed after annealing at the higher temperatures and longer times. Electrical measurements show that annealing at 1400 °C leads to a dopant activation efficiency that is an order of magnitude higher than that observed at 1300 °C, which points to the benefits, in terms of defect density and p-type dopant activation, of using higher temperatures (≥ 1400 °C) annealing cycles to activate Mg acceptors. Novel characterization methods combining high resolution x-ray scattering and transmission electron microscopy were developed to understand the implant-induced strain recovery process and the evolution of extended defect structures after the dopant activation anneal. It was found that homoepitaxial GaN on high quality native substrates is necessary for clearly assessing the implant-induced defects by separating them from the pre-existing intrinsic defects. Results from this work are expected to bring the understanding of the key processing steps to achieve high activation efficiency selective area p-type doping for vertical GaN device structures in a scalable framework.

The dissertation of Yekan Wang is approved

Dwight Christopher Streit

Jaime Marian

Xiaochun Li

Mark S. Goorsky, Committee Chair

University of California, Los Angeles

2022

I would like to dedicate this work to my family

Table of Contents

List of Figures.....	viii
List of Tables.....	xiii
Chapter 1 Introduction.....	1
1.1 Introduction of Power Electronic Devices	1
1.2 Material Properties of GaN.....	2
1.3 Overview of GaN-Based High Power Electronic Devices.....	3
1.4 Development of Bulk GaN Substrate	5
1.5 Selective Area Doping Using Ion Implantation	8
1.6 Novel Dopant Activation Annealing Methods	9
1.7. Extended Defects Formation During Dopant Activation	11
1.8 Motivations	14
1.9 Dissertation Outline	14
Chapter 2 Characterization Methods	16
2.1 X-ray Scattering Techniques.....	16
2.1.1 Triple axis X-ray diffraction.....	16
2.1.2 Double Crystal X-ray Topography.....	20
2.2 Electron Microscopy Techniques.....	22
2.2.1 Transmission Electron Microscopy	23
2.2.2. Scanning Transmission Electron Microscopy.....	26
2.3 Electrical Characterization Techniques.....	28
2.3.1 Hall Effect Measurements.....	28
Chapter 3 Mg Implantation into Heteroepitaxial GaN with Activation Using Multi-Cycle Rapid Thermal Annealing.....	31
3.1 Motivation	31

3.2 Experimental Details.....	31
3.3 Results and discussion.....	32
3.4 Summary	45
Chapter 4 Strain Recovery and Defect Characterization in Mg Implanted Homoepitaxial GaN with Ultra-High-Pressure Annealing	47
4.1 Motivation	47
4.2 Experimental Details.....	47
4.3 Results and discussion.....	48
4.4 Summary	60
Chapter 5 Defects Evolution and Mg Segregation in Mg-implanted GaN with Ultra-High-Pressure Annealing.....	61
5.1 Motivation	61
5.2 Experimental Details.....	61
5.3 Results and discussions	63
Chapter 6 Conclusion and Future Work.....	76
6.1 Conclusions	76
6.2 Future Work	77
Bibliography	79

List of Figures

Figure 1-1 The overall performance of GaN-based power devices compared to traditional Si-based devices.	3
Figure 1-2 (a) device structure of a lateral GaN HEMT; (b) device structure of a vertical GaN p-i-n diode.	4
Figure 1-3 A schematic representing the ammonothermal bulk growth method	6
Figure 1-4 A comparison of TEM images between heteroepitaxial GaN grown on sapphire substrate and the homoepitaxial grown on ammonothermal GaN substrate.....	7
Figure 1-5 Temperature profile of the Multicycle Rapid Thermal Annealing (MRTA) method ³⁸	10
Figure 1-6 Temperature profile of the Ultra High-Pressure Annealing (UHPA) method.	11
Figure 1-7. The annealing of Boron in Si after implantation	13
Figure 2-1 System setup for triple-axis X-ray diffraction measurements.....	17
Figure 2-2 (0004) ω : 2θ scan for GaN before Mg implantation (red) and after Mg implantation (blue).	18
Figure 2-3 Reciprocal lattice points from GaN and two schematics showing both a pseudomorphic structure and a structure with in-plane relaxation.	20
Figure 2-4 . Schematics showing the double crystal x-ray topography setup and the single-exposure x-ray topography from an ideal wafer with no defects (a), and for real wafer with defects (b) and (c) exposed at different positions on the rocking curve.	21
Figure 2-5 Schematics showing the working principle of TEM (left) and STEM (right).	23
Figure 2-6 Example of an HRTEM and the corresponding filtered image showing the lattice distortions introduced by the extended defects such as dislocations.	25

Figure 2-7 STEM BF images with $g = \langle 0002 \rangle$ and $g = \langle 11\bar{2}0 \rangle$ from the Mg implanted GaN after annealing at 1300 °C for 10 minutes.	27
Figure 2-8 Schematic of the theory behind the Hall effect.	29
Figure 3-1 High-resolution x-ray diffraction $\omega:2\theta$ scan near the GaN (0004) peak for (a) the as implanted sample, (b) the sample $\mu 20$, and (c) the sample $\mu 40$. The as-implanted sample shows satellite peak corresponding to implant-induced strained layer.	33
Figure 3-2 X-ray reciprocal space map for the as-implanted sample showing (a) the GaN (0004) RELP, and (b) the (10 $\bar{1}$ 4) RELP.	34
Figure 3-3 (a) High-resolution x-ray diffraction $\omega:2\theta$ scan fitted with dynamical simulation software Bruker RADS. (b) Simulated strain profile plotted with SRIM ion concentration and recoil damage profiles. The ion concentration and recoil damage are normalized to the strain for convenience.	35
Figure 3-4 (a) RSM for as-implanted sample showing the (10 $\bar{1}$ 4) GaN RELP as well as the (22 $\bar{4}$ 6) sapphire RELP (b) RSM for sample $\mu 40$ showing the (10 $\bar{1}$ 4) RELP for GaN as well as the (22 $\bar{4}$ 6) RELP for sapphire.	37
Figure 3-5 Cross-section TEM two beam condition bright field images with different diffraction vectors, (a) sample $\mu 20$, $g = \langle 0002 \rangle$ (b) sample $\mu 40$, $g = \langle 0002 \rangle$, (c) sample $\mu 20$, $g = \langle 11\bar{2}0 \rangle$, (d) sample $\mu 40$, $g = \langle 11\bar{2}0 \rangle$	40
Figure 3-6 Cross-section STEM two beam condition bright field images taken near the implanted region, and the three depths indicate where the images in figure 3-8 are obtained, (a) sample $\mu 20$ with $g = \langle 0002 \rangle$, (b) sample $\mu 40$ with $g = \langle 0002 \rangle$	41
Figure 3-7 (a) High-Resolution TEM lattice image of the implanted region, (b) FFT of (a) before applying the mask (circles), (c) Inverse Fourier transform lattice image.	43

Figure 3-8 (0001) inverse Fourier transform TEM images revealing post-annealing extended defects at different depths for sample $\mu 20$, (a) inside the implantation zone (~ 200 nm), (b) the edge of the implantation zone (~ 500 nm), (c) outside the implantation zone (~ 800 nm) and for sample $\mu 40$, (d) inside the implantation zone (~ 200 nm), (e) the edge of the implantation zone (~ 500 nm), (f) outside the implantation zone (~ 800 nm). 44

Figure 4-1 X-ray reciprocal space map for the as-implanted sample showing (a) the GaN (0004) RELP, and (b) the (10 $\bar{1}$ 4) RELP. 49

Figure 4-2 (a) Triple axis XRD $\omega:2\theta$ scan of the as-implanted sample and simulated scan using RADS software. (b) Triple axis XRD $\omega:2\theta$ scans after annealing at 700 °C for 10 min and 100 min. (c) Triple axis XRD $\omega:2\theta$ scans after annealing at 1300 °C for 10 min and 100 min. (d) Simulated strain profile before and after annealing. No residue strain after annealing at 1300 °C for 10 min and 100 min. 50

Figure 4-3 (10 $\bar{1}$ 4) triple-axis XRD rocking curves for samples annealed at 1300 °C for 10 min and 100 min. 53

Figure 4-4 Synchrotron double crystal x-ray topography (11 $\bar{2}$ 4) images for (a) the unimplanted sample and (b) the as-implanted sample, both show a uniform contrast and the dot features corresponding to individual dislocations with a density of $\sim 10^6$ cm $^{-2}$; (c) the 1300 °C annealed for 100 min sample, shows large non-diffracting regions (arrows); the thin orthogonal lines and circles are from the metalization pattern on the sample surface. 54

Figure 4-5 Cross-section STEM two beam condition bright field images with different diffraction vectors: (a) 1300 °C annealed 10 min sample, $\mathbf{g} = \langle 11\bar{2}0 \rangle$ with the arrows showing the basal plane stacking faults; (b) 1300 °C annealed 10 min sample, $\mathbf{g} = \langle 0002 \rangle$; (c) 1300 °C annealed 100 min sample, $\mathbf{g} = \langle 11\bar{2}0 \rangle$; (d) 1300 °C annealed 100 min sample, $\mathbf{g} = \langle 0002 \rangle$; (e) as-

implanted sample, $\mathbf{g} = \langle 11\bar{2}0 \rangle$; (f) as-implanted sample, $\mathbf{g} = \langle 0002 \rangle$. In (c) and (d), the arrows show beam damage. 56

Figure 4-6 HRTEM image at the implanted region in 1300 °C 10 min sample. Magnification of the image shows the lattice fitted with ball and stick models and confirms a change in the stacking sequence in planes from ABAB (wurtzite) to ABCABC (zincblende). The two circles highlight regions with Moiré fringes. 57

Figure 5-1 (a) Triple axis X-ray $\omega:2\theta$ line scans near GaN (0004) peak for the samples showing the implant induced strain was fully relieved after annealing at 1300 °C for 10 minutes and annealing at temperatures ≥ 1400 °C has no further impact on the strain state; X-ray topography images exposed at a single point along a rocking curve for: (b) as-implanted; (c) annealed at 1300 °C for 10 minutes; (d) annealed at 1400 °C for 100 minutes, and (e) annealed at 1500 °C for 10 minutes. The white dots that appeared in all 4 images (b-e) are individual dislocations, and the densities are on the order of 10^4 cm^{-2} 65

Figure 5-2 Cross-section STEM two beam condition bright field images with diffraction vector $\mathbf{g} = \langle 0002 \rangle$, (a) 1300 °C annealed 10 min sample; (b) 1400 °C annealed 10 min sample; (c) 1400 °C annealed 100 min sample; (d) 1500 °C annealed 10 min sample; and diffraction vector $\mathbf{g} = \langle 11\bar{2}0 \rangle$; (e) 1300 °C annealed 10 min sample; (f) 1400 °C annealed 10 min sample; (g) 1400 °C annealed 100 min sample; (h) 1500 °C annealed 10 min sample. In (f), the arrows show examples of dislocation loops that are not parallel to the FIB cut. All images share the same scale bar shown in (a). 67

Figure 5-3 (a) STEM image of the 1300 °C 10 min sample showing examples of pyramidal inversion domain (circled in red) and trapezoidal inversion domain (boxed in blue); (b) HRTEM image of a pyramidal inversion domain showing the $\{11\bar{2}3\}$ facets (highlighted with dotted

white lines) and the extra layer of atoms near the base (boxed in green); (c) HAADF image of a pyramidal inversion domain; (d) EDX map showing the Mg segregation in the pyramidal inversion domain shown in c. (e) EDX line profile generated by integrating the intensity in the yellow box in Fig. 3d (the arrow shows the direction of the line profile, i.e. the start is at the bottom)..... 69

Figure 5-4 (a) HAADF image of a trapezoidal inversion domain with the edge also showing $\{11\bar{2}3\}$ facets (highlighted with a diagonal orange line); (b) EDX map showing the Mg segregation in the trapezoidal inversion domain shown in a. (c) EDX line profile generated by integrating the intensity in the yellow box in Fig. 4b (the arrow shows the direction of the line profile, i.e. the start is at the bottom). 70

Figure 5-5 Carrier concentration measured using hall measurements for Mg implanted GaN with UHPA at temperatures of 1300 °C and 1400 °C for 10 minutes ⁴⁴. 72

Figure 5-6 (a) HRTEM image of a small dislocation loop, fast Fourier transform pattern from three regions (three boxes) are shown in b-d; b) FFT outside of the loop showed pure hexagonal pattern (red circles); c) FFT close to the center of the loop show hexagonal GaN plus additional cubic GaN pattern (yellow circles); d) FFT on the edge of the loop also show a pure hexagonal pattern; (e) HAADF image of a small dislocation loop and the (f) the EDX map showing no signs of the Mg segregation in the loop. 74

Figure 6-1 SIMS Mg profiles before and after UHPA annealing at temperatures ≥ 1300 °C for 5 mins (left) ⁴³, and SIMS Mg profiles before and after MRTA annealing at a peak temperature <1400 °C for a total time of 5 mins (right) 78

List of Tables

Table 1. The key material properties considered in power applications: GaN vs Si.	2
Table 2 Typical dislocations in GaN and their Burgers vectors b	19
Table 3. FWHM/FW0.01M extracted from the triple-axis rocking curve results and the mobility measurement results from earlier studies ³⁸	38
Table 4. FW0.01M (FWHM) from the triple-axis rocking curve scans.	52

Acknowledgments

First and foremost, I would like to thank my advisor Prof. Mark Goorsky for his support, guidance and leadership throughout my graduate career. He is incredibly knowledgeable. Things I learned from him such as the attention to details and rigorous attitude in data analysis will benefit me in my future career. I also would like to thank my committee members, Prof. Dwight Streit, Prof. Jaime Marian and Prof. Xiaochun Li for sharing their knowledge and providing valuable suggestions for my research work.

Secondly, the work presented here would not be possible without the funding support from the Advanced Research Projects Agency-Energy (ARPA-E) PNDIODES program supervised by Dr. Isik Kizilyalli. I also received help from many excellent collaborators. I would like to thank Dr. James Tweedie, Dr. Pramod Reddy from the Adroit Materials, Dr. Mathew Hayden Breckenridge, Dr. Ramon Ramón Collazo, and Dr. Zlatko Sitar from the North Carolina State University for helping with sample preparation and providing necessary electrical measurements. I would also greatly thank Dr. Michal Bockowski from the Institute of High Pressure Physics, Polish Academy of Sciences, and Dr. Travis Anderson from the Naval Research Lab for helping with the post-implantation annealing experiments. During synchrotron measurements, the support from Dr. Xianrong Huang and Dr. Michael Wojcik from Advanced Photon Source, Argonne National Lab are also greatly appreciated.

I would like to thank the previous group members, Dr. Chao Li, and Dr. Tingyu Bai for training me with a lot of skills that help me with my research. A special thanks to the current group member Michael Liao and Kenny Huynh who worked together with me. We had a lot of great experiences and memories together. I also would like to thank other members in the electronic materials group, Brandon Carson, Lezli Matto, and Aviram Bhalla-levine for their support.

Finally, I would like to thank my family, my parents for their unconditional support and encouragement, and my wife Molly Qu for her unwavering love.

VITA

Education

- 2015 Bachelor of Science in Materials Science and Engineering
University of California, Los Angeles
Los Angeles, CA, USA
- 2017 Master of Science in Materials Science and Engineering
University of California, Los Angeles
Los Angeles, CA, USA

Honor

- 2014 Boeing Scholarship
University of California, Los Angeles
- 2015 Magna Cum Laude
University of California, Los Angeles
- 2017 Departmental Fellowship
University of California, Los Angeles
- 2020 Bruce Deal and Andy Grove Young Author Award
The Electrochemical Society

Selected Publications (5 out of 25)

1. Y. Wang, K. Huynh, M.E. Liao, J. Tweedie, P. Reddy, M.H. Breckenridge, R. Collazo, Z. Sitar, M. Bockowski, X. Huang, M. Wojcik, M.S. Goorsky, “Defects Evolution and Mg Segregation in Mg-implanted GaN with Ultra-High-Pressure Annealing.” *Journal of Applied Physics*, submitted (2022).
2. Y. Wang, M. Liao, K. Huynh, W. Olsen, J.C. Gallagher, T.J. Anderson, X. Huang, M. Wojcik, M.S. Goorsky, “Investigation of the Reverse Leakage Behavior and Substrate Defects in Vertical GaN Schottky and PIN Diodes.” *ECS Journal of Solid State Science and Technology*, in press (2022).
3. Y. Wang, M.E. Liao, K. Huynh, A.A. Allerman, M.S. Goorsky, “Structural Characterization of Dot-Core GaN Substrates with Annealing Under Growth-Like Conditions Using Synchrotron Monochromatic X-ray Topography.” *ECS Journal of Solid State Science and Technology*, 10, 4, 045010, (2021).
4. Y. Wang, K. Huynh, M.E. Liao, H. Yu, T. Bai, J. Tweedie, M.H. Breckenridge, R. Collazo, Z. Sitar, M. Bockowski, Y. Liu, M.S. Goorsky, “Strain Recovery and Defect Characterization in Mg Implanted Homoepitaxial GaN on High Quality GaN Substrates.” *Physic. Status Solidi B*, 257, 1900705, (2020).
5. Y. Wang, T. Bai, C. Li, M. J. Tadjer, T. J. Anderson, J. K. Hite, M. A. Mastro et al. et al, “Defect Characterization of Multicycle Rapid Thermal Annealing Processed p-GaN for Vertical Power Devices.” *ECS Journal of Solid State Science and Technology*, 8, 2, (2019).

Chapter 1 Introduction

1.1 Introduction of Power Electronic Devices

In modern society, the development of science and technology highly depends on the usage of fossil and renewable energy resources, which are converted into the most common energy source: electricity. According to the US Department of Energy, electricity accounted for ~40% of primary energy consumption in the United States in 2015¹. Power electronics devices that convert electricity into a form that is more useful to a given device, are projected to play a significant and growing role in the delivery of this electricity. It has been estimated that as much as 80% of electricity could pass through power electronics between generation and consumption by 2030. In contrast, just 30% of electrical energy passed through power electronics converters in 2005¹. Technical advances in power electronics promise enormous energy efficiency gains throughout the economy. Achieving high power conversion efficiency in these systems, however, requires low-loss power semiconductor switches.

Silicon, the most studied and developed in terms of mass production, has been the material of choice for power electronics ever since the 1960s. Several novel structures based on Silicon have been demonstrated and later commercialized in the power industry to enhance power conversion efficiency, such as Silicon controlled rectifier (SCR)^{2,3}, bipolar junction transistor (BJT)⁴, insulated gate bipolar transistors (IGBTs)^{5, 6}, and super-junction metal oxide semiconductor field effect transistors (MOSFETs)⁷. However, in the past two decades, the power demands are increasing drastically. Popular applications such as the electric automotive industry and giant data centers for cloud computing have advanced by leaps and bounds. The conventional Si-based devices are running into the material limits, resulting in the saturation trend of power density. To overcome the limits, wide bandgap semiconductor materials such as GaN have

emerged to be the successor of Si to enable higher voltage power devices with dramatically improved efficiency as well as reduced form factor.

1.2 Material Properties of GaN

GaN is a compound semiconductor material with a much larger bandgap (3.4 eV) than Si (1.12 eV). The key materials properties related to power device design of GaN compared to Si are shown below in Table 1. The Baliga's figure of merit (BFoM), for unipolar devices with a planar junction, is defined as the product of permittivity (ϵ_r), carrier mobility (mostly electrons), and the cube of the critical field ⁸. The resultant BFoM of GaN is more than 3 orders of magnitude higher than that of Si. Owing to the exceptional material properties, the power switches based on GaN offer noticeable advantages over Si and can be summarized in five main categories, as shown in Figure 1-1. Besides improving the breakdown field drastically, the large bandgap of GaN and high potential barrier also increased the allowable operating temperature of the GaN device (300-400 °C)⁹.

Properties	Silicon	GaN
Bandgap E_g (eV)	1.12	3.4
Critical Field E_{crit} (MV/cm)	0.23	3.3
Electron Mobility μ_n (cm ² /Vs)	1400	1500
Saturated Electron Velocity (10 ⁷ cm/s)	1	2.2
Permittivity ϵ_r	11.8	9
BFoM: $\epsilon_r \cdot \mu_n \cdot E_{crit}^3$ (Rel. to Si)	1	2400

Table 1. The key material properties considered in power applications: GaN vs Si.

On the other hand, due to high electric field and saturation velocity, the GaN-based switches can operate at a high frequency¹⁰. Taking advantage of these, GaN-based power switches are expected to deliver high efficiencies and very low losses.

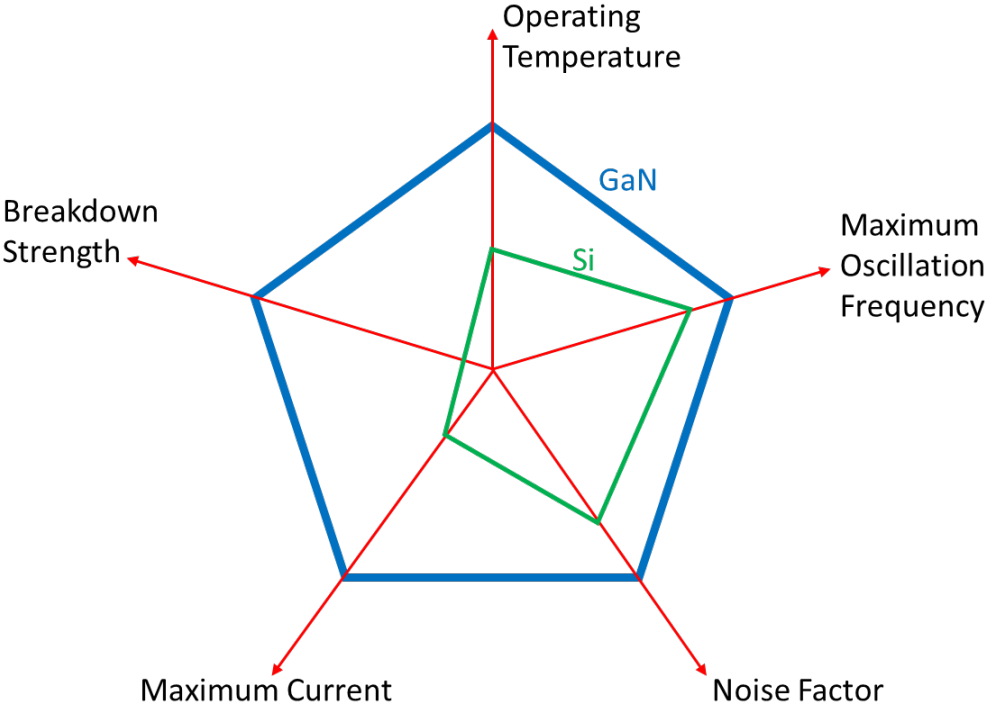


Figure 1-1 The overall performance of GaN-based power devices compared to traditional Si-based devices.

1.3 Overview of GaN-Based High Power Electronic Devices

In General, GaN power devices can be divided into two categories based on the device architecture: lateral devices and vertical devices. The most popular GaN device today is the lateral High Electron Mobility Transistor (HEMT). The development of HEMT started over 20 years ago^{11, 12}. GaN-based HEMT uses substrates such as Si or sapphire, and grow GaN and AlGaIn on top of these foreign substrates. A schematic showing the general structure of a HEMT is shown in

figure 1-2a. Due to spontaneous and piezoelectric polarization, electrons accumulate at the AlGa_N/Ga_N interface, forming a two-dimensional electron gas (2DEG) with high mobility ($> 1200 \text{ V/cm}^2$)^{13, 14}. The lateral HEMT devices have small on-resistance and small gate charge, which is beneficial to enhancing the switching frequency. The lateral Ga_N HEMT power switches have shown performance, in the low-medium voltage range ($< 600 \text{ V}$), that can rival traditional Si-based transistor switches such as IGBTs and MOSFETs¹⁵.

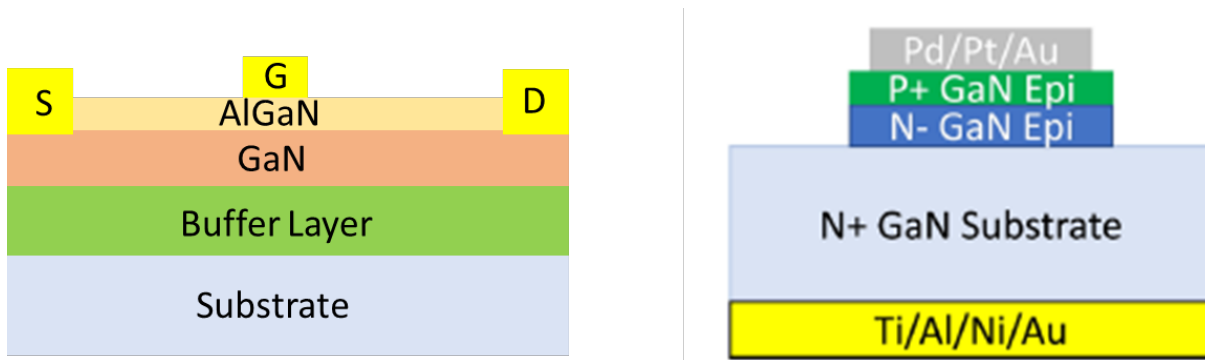


Figure 1-2 (a) device structure of a lateral Ga_N HEMT; (b) device structure of a vertical Ga_N p-i-n diode.

However, the lateral device architecture also has some limitations. Firstly, since it used heteroepitaxy on a foreign substrate, there are a relatively high amount ($>10^8 \text{ cm}^{-2}$) of defects existing in the Ga_N and the AlGa_N, which increases the chance of device failure under operation^{16, 17}. Secondly, to withstand a high voltage, lateral devices need careful management of the electric field. The lateral dimension (drain-source distance) of the lateral device has to be extended to allow high breakdown voltage¹⁸, which reduces the effective current density and increases footprints. Meanwhile, thermal management in lateral devices is complicated. The thermal conductivity of Ga_N ($1.3 \text{ W/cm}\cdot\text{K}$) is similar to that of Si ($1.5 \text{ W/cm}\cdot\text{K}$). However, the current flow in lateral devices is confined to the thin channel near the surface. Therefore, it is difficult to extract the heat

¹⁹. To overcome these limitations, and with the more readily available high-quality bulk GaN substrate, the vertical device architecture has attracted more attention in the past decade. For example, the device structure of a vertical GaN p-i-n diode ²⁰ is shown figure 1-2b. The vertical GaN device architecture allows current to flow vertically across the device and the electric field spreads more. On the other hand, device cooling is more straightforward as heat is transferred through a homoepitaxial system and directly to the package lead frame. Bulk GaN substrate also has low dislocation density ($<10^6 \text{ cm}^{-2}$) ^{21, 22} which should improve the long-term reliability of the vertical GaN devices. Lastly, the vertical structure can deliver higher breakdown voltage by increasing the thickness of the drift layer without increasing the footprints, which is particularly suitable for applications that require a high breakdown voltage ($> 1200 \text{ V}$) ²³.

1.4 Development of Bulk GaN Substrate

As discussed in the previous section, the development of vertical GaN power devices depends heavily on the availability of large size bulk GaN substrate. Due to the high melting point ($>2500 \text{ }^\circ\text{C}$) of GaN and high equilibrium nitrogen pressure necessary for congruent melting of GaN, it is difficult to grow GaN substrate from a melt-growth approach, such as the Czochralski method. Therefore, GaN substrate is grown by other techniques that require lower pressure and temperature. So far, the best quality GaN substrate is produced by using the ammonothermal method. The ammonothermal growth approach is an analog of the hydrothermal method, used in the industrial production of quartz. A schematic showing the growth setup is shown in figure 1-3 ²⁴. Briefly, during growth, GaN sources crystals are dissolved in supercritical ammonia in a reactor (hundreds of MPa). The solution is then transported to another chamber, where the solution is supersaturated and crystallization of GaN occurs on top of GaN seed crystals. To facilitate

ammonothermal growth, there needs to be an appropriate temperature gradient between the dissolution and crystallization zones. The typical growth temperature is in the range of 400–750 °C²². Some mineralizers are added to ammonia in the dissolution zone to enhance the solubility of GaN. Depending on the mineralizers, the growth can be proceeded in a different environment: basic^{25, 26} or acidic²⁷. The growth rate of ammonothermal GaN is on the order of tens of $\mu\text{m}/\text{day}$, which is relatively slow. However, it produces GaN substrate with the lowest defect density (on the order of 10^4 cm^{-4}) from any bulk GaN substrate²².

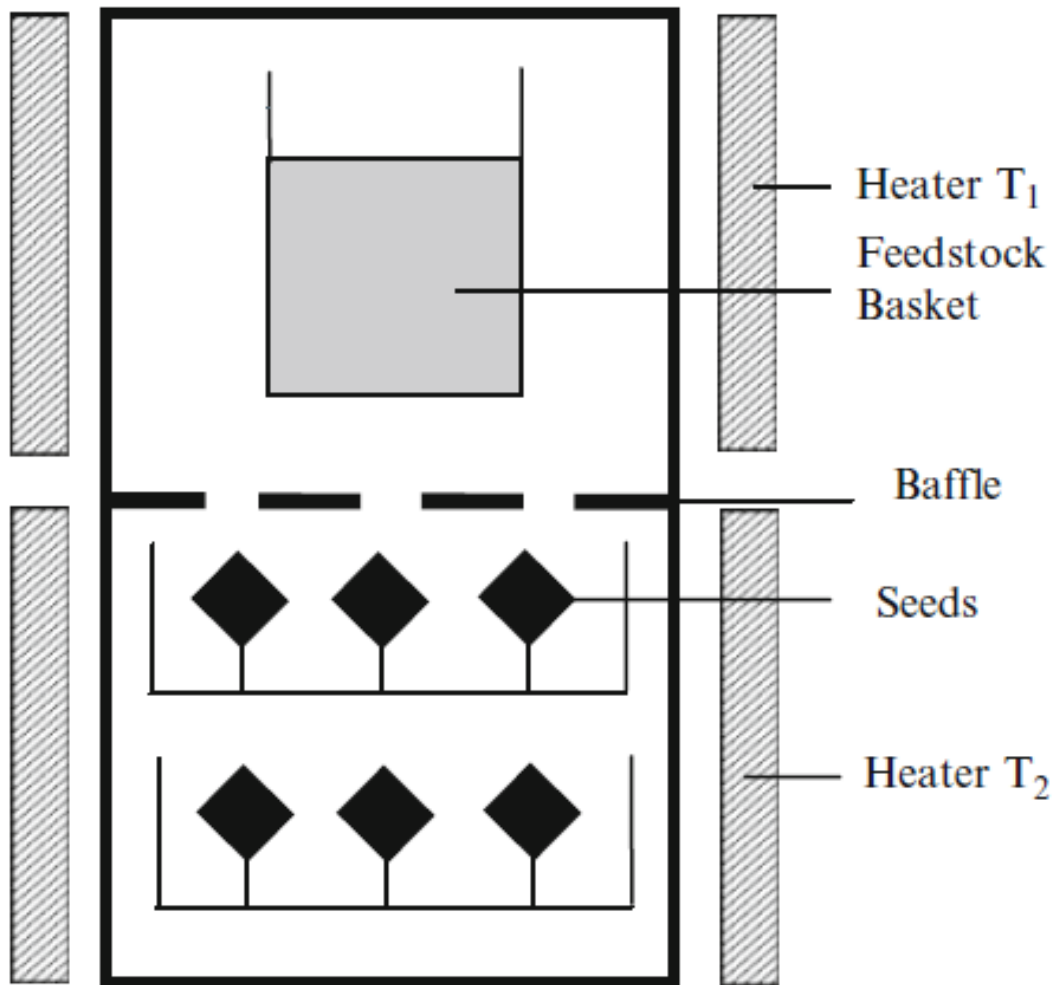


Figure 1-3 A schematic representing the ammonothermal bulk growth method²⁴.

Part of the work (Ch. 4 and Ch. 5) presented in this thesis takes advantage of the low defect density in ammonothermal GaN to get a high-quality homoepitaxial structure, to help separate the processing-induced (such as ion implantation and dopant activation anneal) defects, from the pre-existing intrinsic defects. Figure 1-4 shows a comparison of TEM images between heteroepitaxial GaN grown on sapphire and homoepitaxial GaN grown on ammonothermal GaN substrate. The GaN/sapphire interface is highly defective and quite a few threading dislocations propagate all the way to the surface. In comparison, the GaN/GaN interface is not visible under TEM (indicative of a high-quality interface) and no threading dislocation is observed under the same field of view.

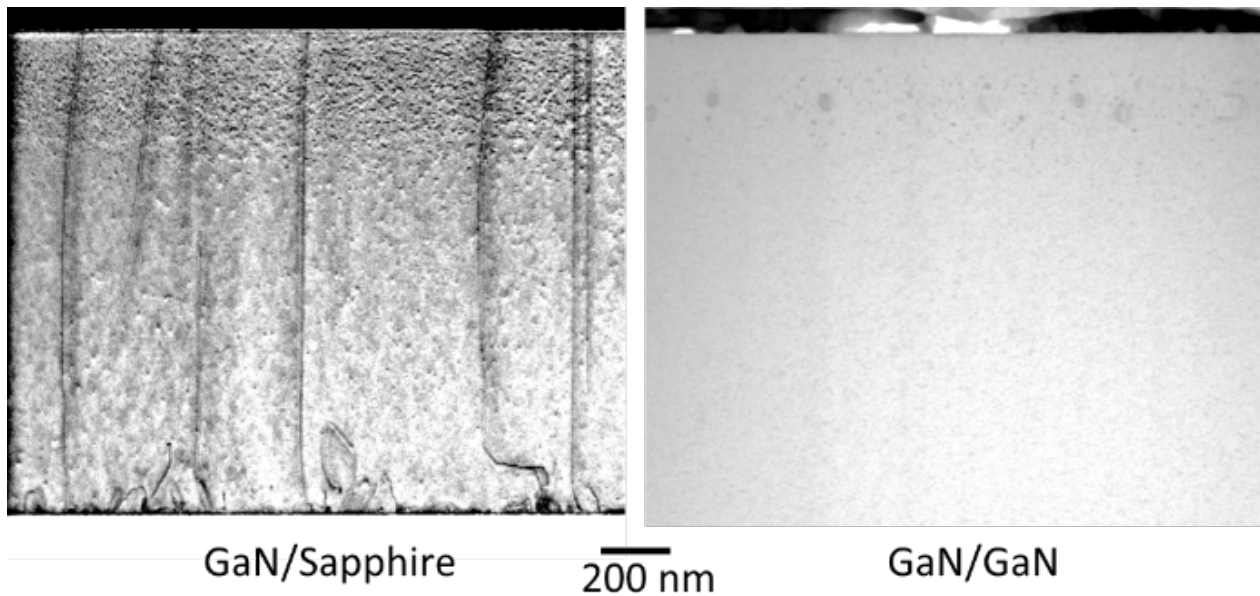


Figure 1-4 A comparison of TEM images between heteroepitaxial GaN grown on sapphire substrate and the homoepitaxial grown on ammonothermal GaN substrate.

1.5 Selective Area Doping Using Ion Implantation

Doping refers to the process of changing the electrical properties of semiconductor material by introducing impurities into the crystal lattice. Depending on the valence electron state of the impurities, the host semiconductor material can be doped to either n- (if the impurities have more valence electrons than the host) or p-type (if the impurities have fewer valence electrons than the host). The ability to create n- and p-type semiconductors is necessary for building a p-n junction, the fundamental chassis for most power electronic devices. Ion implantation is a universal method for doping semiconductors and has been widely used in the electronic industry for decades^{28, 29}. It uses accelerated charged particles (ionized dopant atoms) and physically embed them into the semiconductor (target). Ion implantation can provide precise control of the dopant profile (depth and concentration) and achieve selective doping at the interested area with appropriate masking. However, the ion implantation process generally produces lattice point defects originating from the displacement of host atoms by direct collisions with the incident ions as well as secondary collisions with recoiling atoms. For dopant species to contribute to conduction, dopant activation involving both the removal of point defects and the movement of the dopant species onto proper substitutional lattice sites must occur. Thermal annealing is the most common method used to supply the energy necessary for dopant activation.

Ion implantation and subsequent activation annealing have shown promise in GaN, especially for n-type doping. Studies have shown that Si-doped GaN with appropriate annealing could achieve higher than 50% donor activation^{30,31}. However, on the other hand, p-type dopant activation remains a challenging task. One fundamental limitation is the lack of shallow acceptor in GaN. The ionization energy for p-type dopants in GaN is much higher than for Si and standard III-V materials. For example, ionization energies for acceptors in Si and GaAs are on the order of

30-40 meV. This means that nearly all (> 99% at room temperature) of the dopant atoms on substitutional sites will contribute holes and produce p-type material. In comparison, Mg is currently the most promising p-type implanted dopant with an ionization energy of ~200 meV. At a such deep level, the fraction of ionized acceptors is significantly less (~10% at room temperature) than the near unity values observed with other semiconductors. For example, using the Mg dopant, one needs to introduce a concentration on the order of 10^{18} cm^{-3} to achieve a carrier concentration of $\sim 10^{17} \text{ cm}^{-3}$. The amount of lattice distortion introduced is proportional to the dose, meaning that a much greater level of lattice distortion is introduced to produce a certain carrier concentration in GaN. This requires annealing at a higher temperature to remove the lattice distortions and activate the dopants.

1.6 Novel Dopant Activation Annealing Methods

The targeted annealing temperature for GaN, based on the experience from other semiconductors, is $\sim 2/3$ the melting point ($\sim 1500 \text{ }^\circ\text{C}$). An important issue in the post-implant annealing of GaN is that GaN decomposes at around $840 \text{ }^\circ\text{C}$ under room pressure³², which is well below the temperatures expected to be required to achieve high dopant activation. The GaN desorption increases N vacancies, which is a compensating donor and could reduce the free hole concentration³³. Methods have been developed to overcome the GaN decomposition issue. One approach is to deposit a capping material (such as AlN) to protect the surface^{34, 35, 36}. However, those caps typically only preserve the GaN surface for a short time (a few minutes) at elevated temperatures. Therefore, annealing must be done with a rapid heating-cooling recipe to keep the overall time at elevated temperature short. Niwa et al, used conventional rapid thermal annealing (RTA) to activate Mg acceptors after implantation and were able to achieve a maximum activation

efficiency of 2.3% at 1250 °C for a single annealing cycle of 20s ³⁷. It was speculated that if multiple annealing cycles were performed, an accumulation effect would result in higher dopant activation efficiency. Based on this idea, the U.S Navy Research Lab (NRL) has developed the Multicycle Rapid Thermal Annealing (MRTA) method ^{38, 39, 40}. The technique uses a thin (4 nm) AlN capping with a moderate N₂ overpressure (~20 Bar), and a fast ramp rate (500 °C/s) so that the effect of annealing is accumulated after each cycle while the total time at elevated temperature is kept low. An example of the temperature profile of MRTA is shown in figure 1-5. Anderson et.al showed that MRTA using a series of short time spike anneals at temperatures up to ~ 1400 °C can achieve ~8% doping activation (close to the 10% limit) ³⁸.

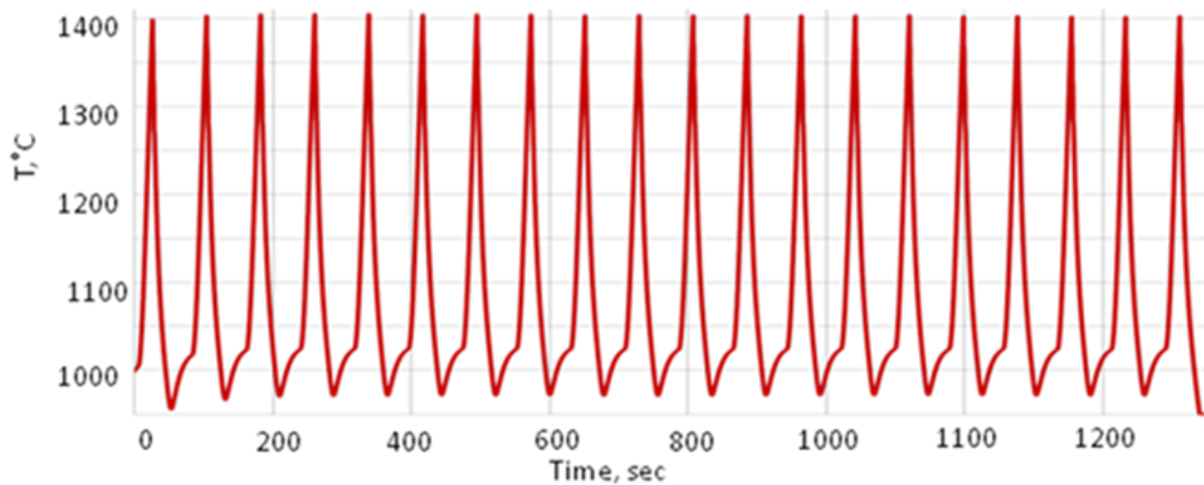


Figure 1-5 Temperature profile of the Multicycle Rapid Thermal Annealing (MRTA) method ³⁸.

An alternative solution is to perform ultra-high N₂ pressure post-implantation annealing (UHPA), which suppresses GaN decomposition even in the absence of a capping layer. It was found that by applying an ultra-high N₂ pressure of 1 GPa, the annealing temperature can be increased to 1500 °C without showing any sign of GaN decomposition ^{41, 42}. The temperature profile of UHPA is shown in figure 1-6. Since it is a conventional annealing with a slow ramp rate (40 °C/min), the total time at a high temperature can also be as long as ~hours under certain

conditions. Recently, Sakurai *et al* have demonstrated successful p-type acceptor formation (with over 50% activation at 500K) in Mg-ion implanted GaN using high pressure (N₂ 1 GPa, 1380 °C, 5 min) annealing ⁴³. Another study from Breckenridge *et al.* reported the electrical data showing that annealing at 1400 °C under similar conditions leads to even higher dopant activation, ~10% at room temperature, and ~100% at 500 °C ⁴⁴.

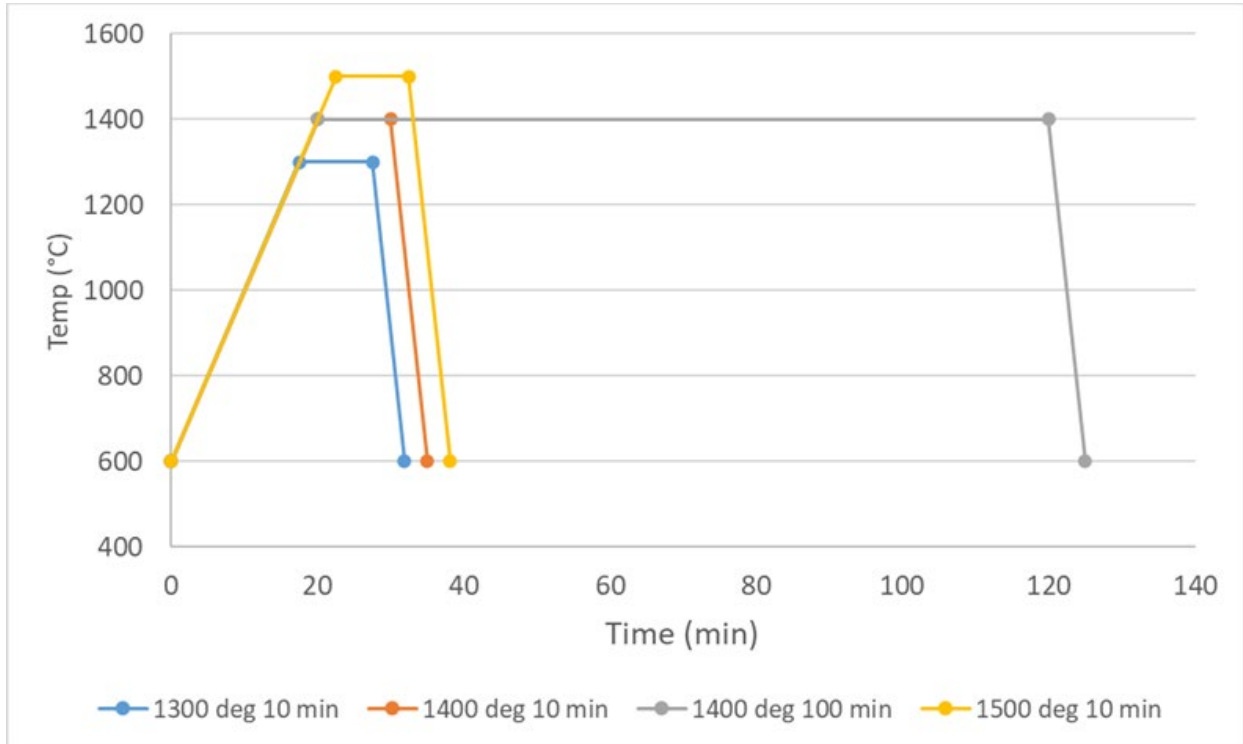


Figure 1-6 Temperature profile of the Ultra High-Pressure Annealing (UHPA) method.

1.7. Extended Defects Formation During Dopant Activation

Post-implantation annealing removes the lattice strain produced by recoil damage as well as promotes movement of the Mg dopants to lattice sites ⁴⁵. The lattice strain originates from the implanted species as well as the subsequent knock-on of host atoms. These species then intercalate into the lattice and cause lattice expansion. However, to be an active acceptor for conduction, Mg must replace Ga in the lattice. At elevated temperature, the relationship between the dopant

activation and defect evolution is not very well understood in GaN. It was found that, in many semiconductor systems, the implant-induced point defects might coalesce, and form extended defects such as stacking faults or dislocation loops ^{46,47,48}. With this coalescence, it becomes extremely difficult to remove the extended defects as they are somewhat stable against further annealing ^{49, 50}. This phenomenon has been previously noted for p-type dopant activation of GaAs ^{51, 52} as well as in earlier work on implantation in silicon ⁵³. Boron implant in Si has been well studied to show an anomalous characteristic, as shown in figure 1-7, with three stages. Stage I shows the annealing of point defect disorder and is accompanied by a rapid increase in activation. After that, extended defects start to form and dopant atoms are trapped in these defects, causing a decrease in activation. Eventually, after 700 °C, extended defects are removed, and B dopants are free to get back to substitutional for Si in the lattice and become active. On the other hand, for carbon implanted GaAs ^{51, 52}, triple axis x-ray scattering measurements showed that the initial implant produced an elastic strain in the lattice. After rapid thermal annealing, the implant-induced strain was relieved. However, the activation efficiency was initially below 40% at 700 °C. X-ray reciprocal space maps (RSM) showed broadening in the in-plane direction, indicating the formation of extended defects that introduce localized tilts in the lattice. After annealing at higher temperatures (> 1000 °C), not only is the elastic strain relieved, and the in-plane broadening is also minimized, indicating that the crystal shows no signs of the formation of extended defects. This was confirmed by a high activation efficiency (>95%). These earlier works in studying the p-type dopant activation in Si and GaAs provide a useful framework in understanding structural information during the post-implantation annealing.

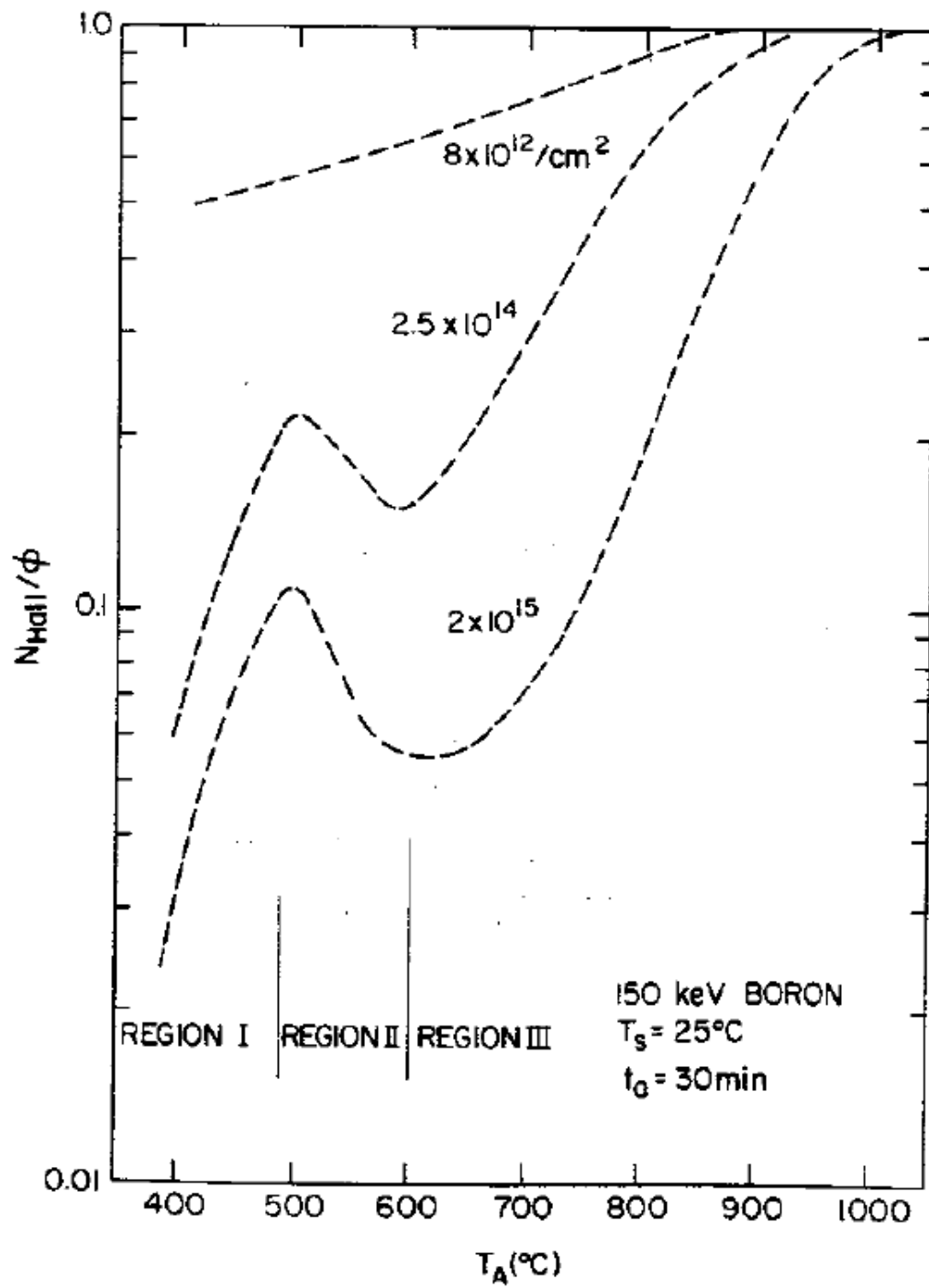


Figure 1-7. The annealing of Boron in Si after implantation ⁵³.

1.8 Motivations

The goal of this work is to provide a fundamental understanding that relates defects and performance. In the current literature, there remains a lack of understanding of the relationship between processing methods (such as annealing temperature and time), the nature of the extended defects formed after annealing, and their impacts on the ultimate dopant activation efficiency. Meanwhile, it remains a question whether Mg in GaN exhibits similar 3-stage characteristic like B in Si, nor do we know the exact time and temperature required to remove all the extended defect in GaN. Therefore, a systematic study that directly links the structural defects with the electrical performance is very demanding. The work presented in this dissertation can be very important in guiding the selection of optimal processing parameters for dopant activation annealing and improving the ultimate device performance.

1.9 Dissertation Outline

In this thesis, the introduction of GaN-based power devices and the general background of selective area doping using ion implantation are discussed first in Chapter 1. Chapter 2 presents the characterization techniques/methods used to understand the defect structures and electrical performance of devices fabricated using ion implantation of Mg into GaN. Chapter 3 shows the study of defect characterization in Multicycle Rapid Thermal Annealing processed heteroepitaxial GaN after Mg implantation. Chapter 4 focuses on implant-induced strain recovery and post-annealing defects in homoepitaxial GaN implanted with single-step Mg implant and annealed under ultra-high N_2 (one GPa) pressure at temperatures up to 1300 °C. Chapter 5 is an extension of chapter 4, using homoepitaxial GaN implanted with a multi-step box Mg profile and annealed

under ultra-high N₂ (one GPa) pressure at temperatures up to 1500 °C. In Chapter 7, the conclusions of this research and future work are provided.

Chapter 2 Characterization Methods

2.1 X-ray Scattering Techniques

X-ray scattering techniques have been widely used as an effective non-destructive characterization method for studying structure imperfections in semiconductor materials. The x-ray scattering techniques used in the dissertation can be split into two aspects: diffraction and imaging using topography. Both techniques are based on the fundamental Bragg's law,

$$\lambda = 2d \sin \theta \quad (1)$$

where λ is the wavelength of the radiation used, d is the plane spacing and θ is the Bragg angle. The wavelength of X-rays (for example, $\lambda_{\text{Cu K}\alpha 1} = 1.5406 \text{ \AA}$) is on the same order as the plane spacing. Therefore, the Bragg angle is very sensitive to the change in plane spacing d . Structure imperfections that distort the lattice structure of the crystal will have an impact on the Bragg angle and can be analyzed using x-ray scattering techniques. Details about each technique are described in the next couple of sections.

2.1.1 Triple axis X-ray diffraction

As discussed in the previous chapter, the developments of GaN bulk growth have drastically improved the crystalline quality of both the GaN substrate and homoepitaxial GaN films. To precisely characterize the defect structures, high resolution triple-axis X-ray diffraction (TAD) is employed. A schematic showing the setup of the TAD measurements is shown in Figure 2-1. After the X-ray comes out from the tube, it reaches a graded mirror to produce a parallel beam. The beam is further collimated by a two-bounce Si (220) channel cut monochromator before

hitting the sample. The diffracted beam passes through a two-bounce Si (220) analyzing crystal and finally is captured by the detector.

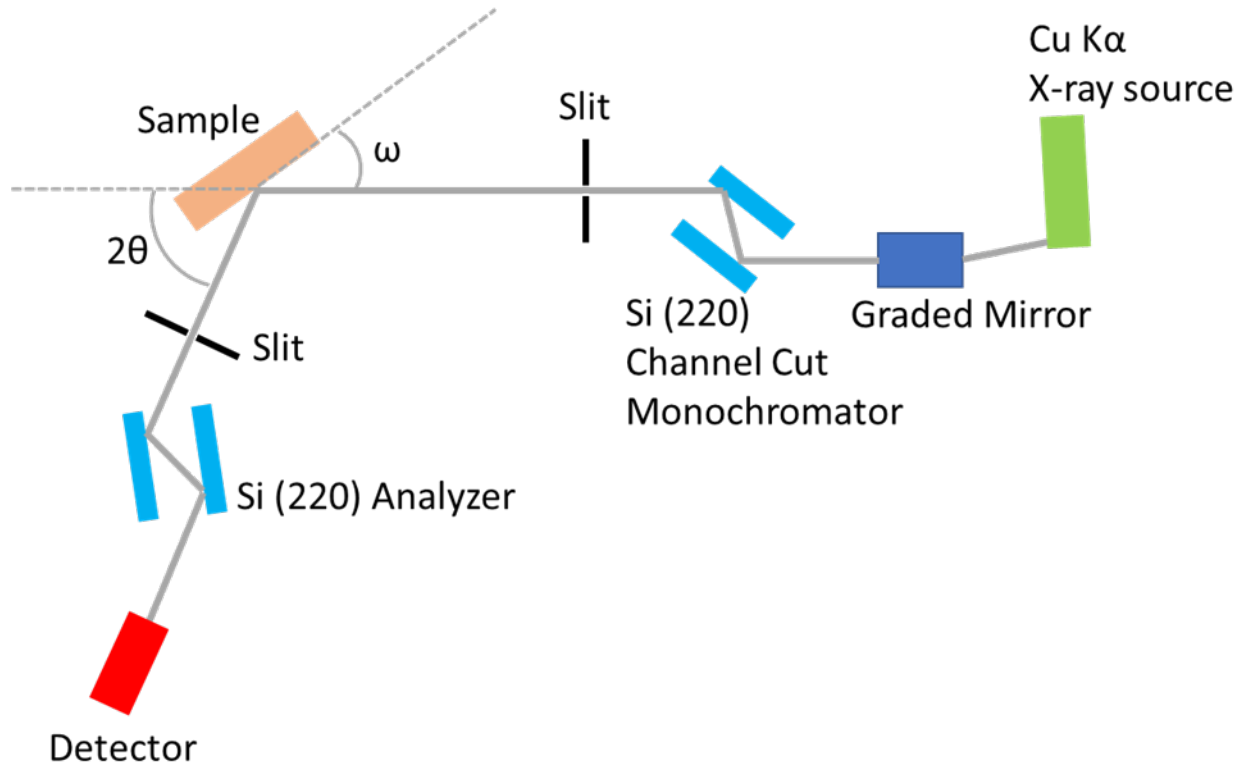


Figure 2-1 System setup for triple-axis X-ray diffraction measurements.

Both line scans and reciprocal space maps are measured using the triple-axis setup. TAD line scans are obtained in two scan directions. First is a coupled scan, $\omega:2\theta$ scan, in which the detector angle 2θ is moved at twice the rate as the rotation of the sample stage (ω). The two angles are labeled in figure 2-1. The $\omega:2\theta$ scan shows planes with different spacing (in other words, Bragg angle) but with the same amount of tilt. For implantation, $\omega:2\theta$ scan is very useful for studying the implant-induced strain. The implant species and the atoms knocked off stretch the lattice and result in a slight increase in the plane spacing in the implanted region. In the $\omega:2\theta$ scan, this is reflected by an excessive intensity (or sometimes a side peak) to the left of the main peak. An example is given

in figure 2-2 where the red scan shows (0004) $\omega:2\theta$ scan for GaN before Mg implantation and the blue scan corresponds to the same sample after Mg implantation without annealing.

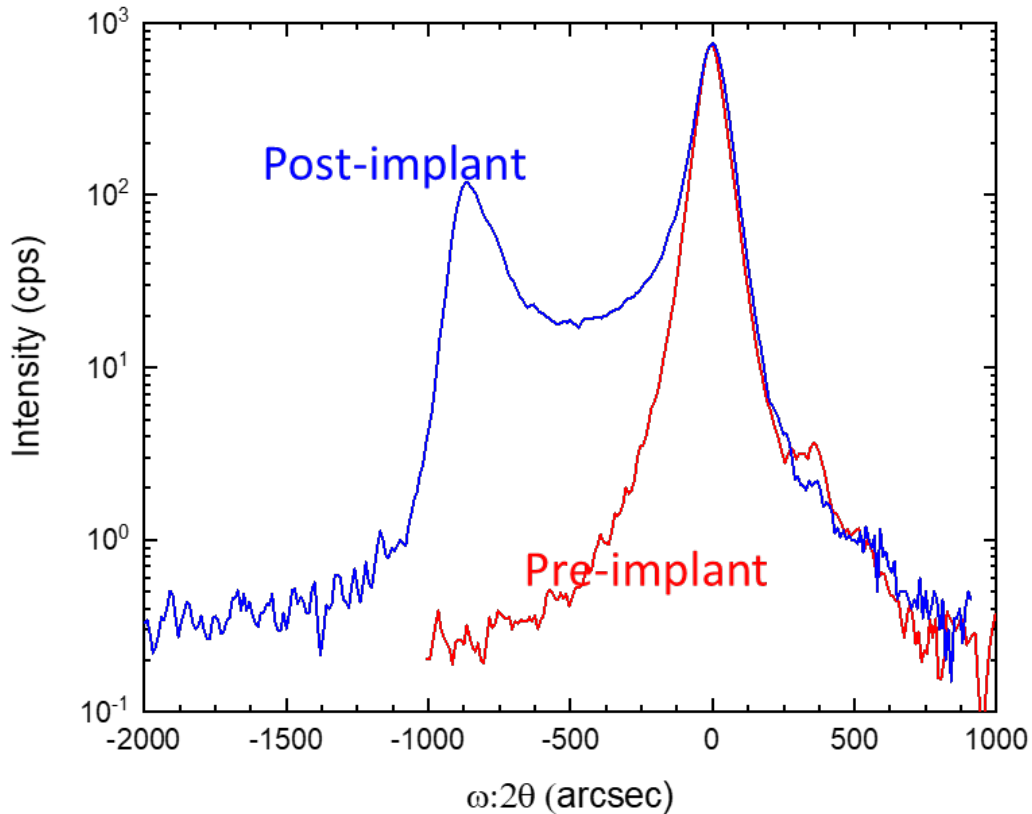


Figure 2-2 (0004) $\omega:2\theta$ scan for GaN before Mg implantation (red) and after Mg implantation (blue).

The second type of line scan is the rocking curve, in which the detector angle is fixed at the Bragg condition, and the sample stage rocks around ω as the scan goes. It measures the mosaicity and tilt in the material. Structural defects such as dislocations introduced local lattice tilt and will result in a broadening in the rocking curve. Both symmetric (0004) and asymmetric (10 $\bar{1}$ 4) rocking curves are measured to account for dislocations with different Burgers vectors. A list of typical

dislocations with their corresponding Burgers vectors is listed in table 3. For example, pure edge dislocations have Burgers vector of $\frac{1}{3}\langle 11\bar{2}0 \rangle$, which is perpendicular to the (0004) planes and therefore do not affect the (0004) rocking curve width. To observe the effect of such dislocations, an asymmetric rocking curve measurement is necessary.

Dislocation type	b	Bounds
Frank-Shockley partial	$\frac{1}{6}\langle 20\bar{2}3 \rangle$	l_1
Shockley partial	$\frac{1}{3}\langle 1\bar{1}00 \rangle$	l_2
Frank partial	$\frac{1}{2}\langle 0001 \rangle$	E
Pure (a type)	$\frac{1}{3}\langle 11\bar{2}0 \rangle$	None
Pure (a+c type)	$\frac{1}{3}\langle 11\bar{2}3 \rangle$	None
Pure (c type)	$\langle 0001 \rangle$	None

Table 2 Typical dislocations in GaN and their Burgers vectors **b** ⁵⁴.

The reciprocal space map collects a series of $\omega:2\theta$ scans with different ω offset and provides useful information about the strain direction and relaxation state. As shown in figure 2-3, in general, two reciprocal space maps are measured with a symmetric reflection (such as 0004) and an asymmetric reflection (such as $10\bar{1}4$). If the implant-induced strain is pseudomorphic (with respect to the unimplanted material), the reciprocal lattice point (REL P) from the unimplanted GaN and the REL P from the implant-induced strained layer will be aligned vertically (in the Qz direction) in both maps, indicating that both have the same in-plane lattice parameter. Otherwise, due to the in-plane relaxation and lattice mismatch, the RELPs from ($10\bar{1}4$) map from the unimplanted GaN and the implant-induced strained layer no longer align in the Qz direction. Schematics showing both a pseudomorphic structure and a structure with in-plane relaxation are shown in figure 2-3.

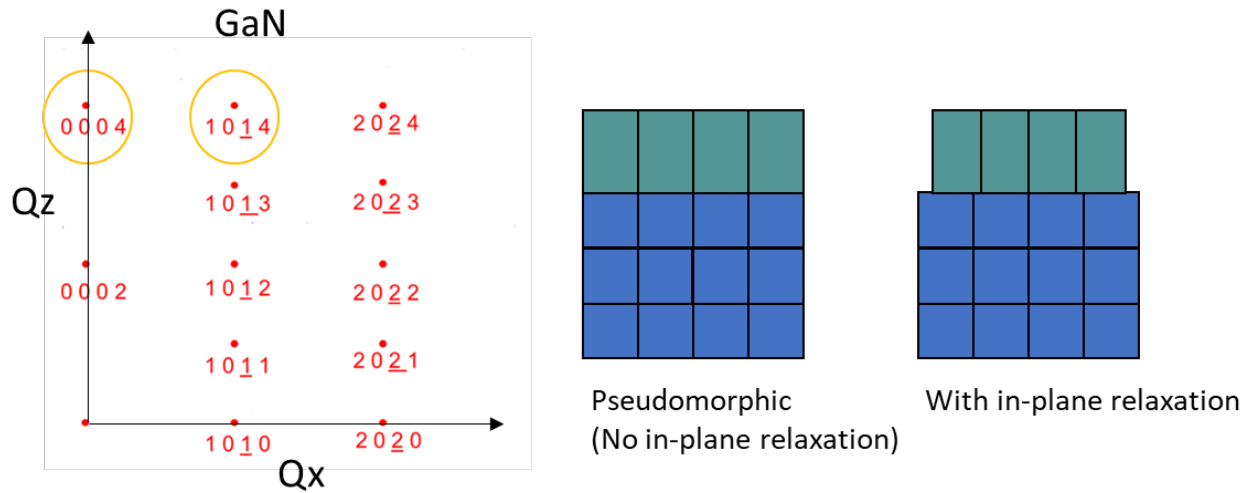


Figure 2-3 Reciprocal lattice points from GaN and two schematics showing both a pseudomorphic structure and a structure with in-plane relaxation.

2.1.2 Double Crystal X-ray Topography

X-ray topography (XRT) is a nondestructive characterization technique for imaging the defects and show contrast due to the long-range distortion fields and/or the strain fields associated with lattice deformations. XRT is a very powerful tool for characterizing crystal and thin-film growth and processing. Double crystal X-ray topography (DCXRT) setup uses reflection-diffraction geometry. A schematic showing the DCXRT setup is shown in figure 2-4. The incident X-ray beam, a synchrotron x-ray source with a photon energy of 8.05 keV, is expanded by a Si (333) first crystal. The sample (2nd crystal) was oriented for diffraction of the $(11\bar{2}4)$ reflection. XRT images were taken by exposing the Agfa Structurix D3 X-ray films at multiple positions on the rocking curve and recorded separately on different films (hereinafter referred to as single exposure images). For an ideal wafer, there is no defect and the radius of curvature is infinity. The $(11\bar{2}4)$

rocking curve for an ideal wafer is a sharp single peak. Single exposure XRT image will show the entire wafer, as shown in figure 2-4a.

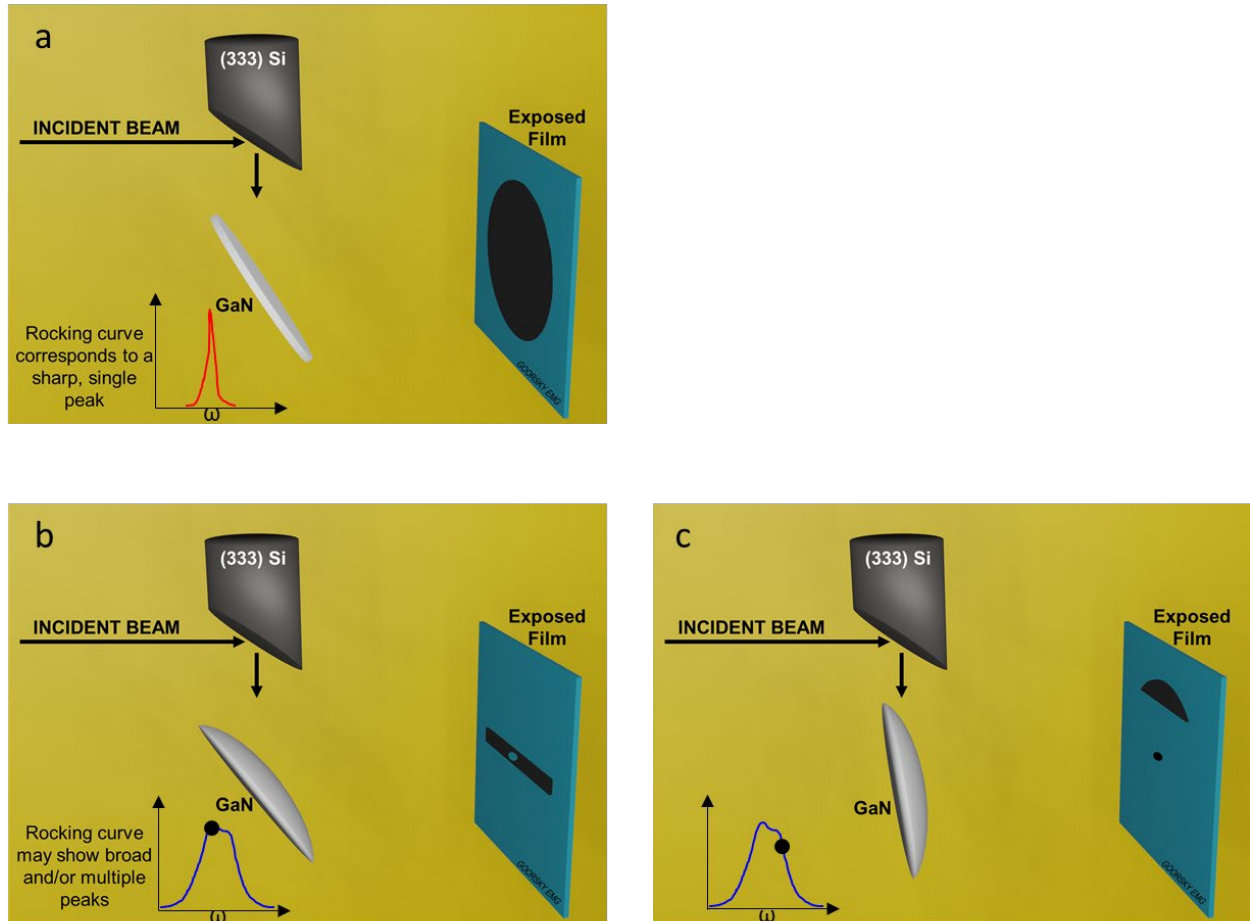


Figure 2-4 . Schematics showing the double crystal x-ray topography setup and the single-exposure x-ray topography from an ideal wafer with no defects (a), and for real wafer with defects (b) and (c) exposed at different positions on the rocking curve.

For a real wafer, due to the presence of finite lattice curvature and defects, the $(11\bar{2}4)$ rocking curve may show a broad peak or multiple peaks. As a result, diffraction is obtained only from a region or “stripe” of the wafer that satisfies the Bragg condition, as shown in figure 2-4b. A different stripe of the wafer is brought into diffraction conditions upon rotation of the crystal to a

different ω position. Also, there are some conditions where diffraction occurs outside the “stripe” as shown in figure 2-4c. These regions are typically materials that are misoriented (due to the presence of defects) with respect to a previous “stripe” but have similar orientation as the current “stripe”. The local misorientations can be quantified by knowing the rotation angle $\Delta\omega$ between the two exposures. Previous work that employed DCXRT to analyze a wide roster of materials such as Si^{55, 56}, SiC⁵⁷, and InP⁵⁸ have demonstrated that a lot of information can be extracted from X-ray topography images, which includes distinguishing tilt differences among misfit dislocations, quantifying the tilt magnitude in tilt boundaries/domains, and identifying whether the diffracted area shapes are due to tilt and/or strain. In this dissertation, DCXRT will be employed primarily to examine the defects before and after the dopant activation annealing in Mg implanted GaN.

2.2 Electron Microscopy Techniques

Post-implantation annealing is necessary to remove implant-induced lattice strain and promote dopant atoms to move to desired lattice site (for example, Mg on Ga site) to be active for conduction. This process, however, is accompanied by the formation of extended defects. Understanding the nature of these extended defects and how they affect dopant activation is critical for improving the ultimate performance of the devices. This cannot be achieved without using electron microscopy techniques. This work employed a number of different advanced electron microscopes to help understand the structural and chemical nature of the residual defects after different annealing conditions.

2.2.1 Transmission Electron Microscopy

Transmission electron microscopy (TEM) is a very powerful material characterization method for studying atomic structures and defects in semiconductor materials. It uses a beam of electrons that are generated by a field emission gun operated under high voltage (80-300 kV). A schematic showing the working principle of the TEM is shown in figure 2-5 on the left. The beam is focused with magnetic lens (condenser lens) before hitting the sample. TEM samples are typically less than 100 nm to allow electron to pass through. The transmitted beam is focused by the objective lens and an image is generated on a CCD camera.

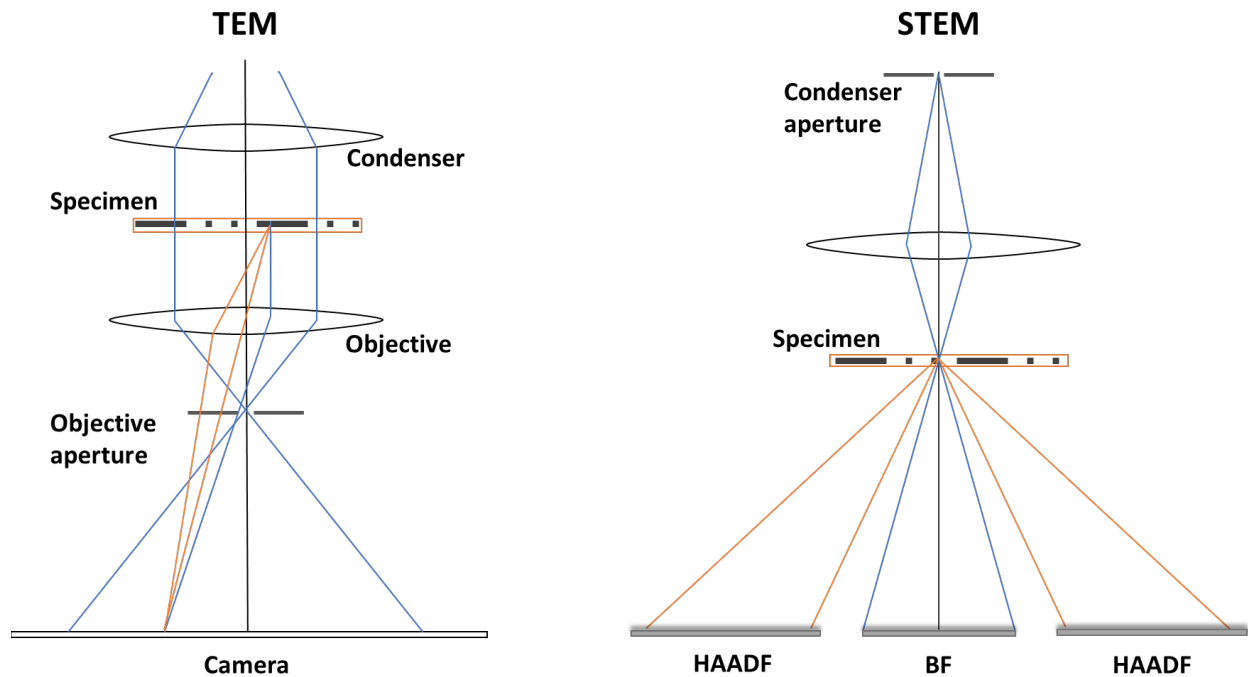


Figure 2-5 Schematics showing the working principle of TEM (left) and STEM (right).

When electrons penetrate through the thin sample, the scattering of the incident beam by the sample generates a series of contrasts. For example, thick layers/heavier materials scatter electrons more than thin layer/low mass materials. This type of contrast is often referred to as mass-thickness

contrast. The second type of contrast is diffraction contrast. For a single crystalline material, the lattice shows a specific crystallographic orientation. The atomic planes scatter electron at the angle that satisfies the Bragg condition. However, if the material is polycrystalline, electrons that are scattered by grains with different orientations show contrast differences. The third type of contrast is phase contrast, which is the primary contrast in high-resolution transmission electron microscopy (HRTEM). Phase contrast comes from the phase differences in electron waves. In general, for a single crystalline material, the periodic lattice generates phase difference between the transmitted beam and the diffracted beam. After passing the objective lens, these two beams interact and recombine to show interference pattern that reveals the periodic nature of the sample. The capability of resolving lattice structure and disorder makes HRTEM a popular method for studying material interfaces and defects. To order to better show the lattice distortions, special processing of the HRTEM image using inverse Fourier transform filtering can be used. Details of the filtering technique will be discussed later in chapter 3. Here, an example is given in figure 2-6. The original HRTEM image is given and a section from the HRTEM image (yellow box) shows clear lattice structure. Normally, images with clear lattice structure will be considered to represent materials with high crystalline quality. However, after applying the filtering process, the inverse Fourier transform filtered HRTEM image gives a better visualization of the lattice distortions that are otherwise difficult to see in the original image.

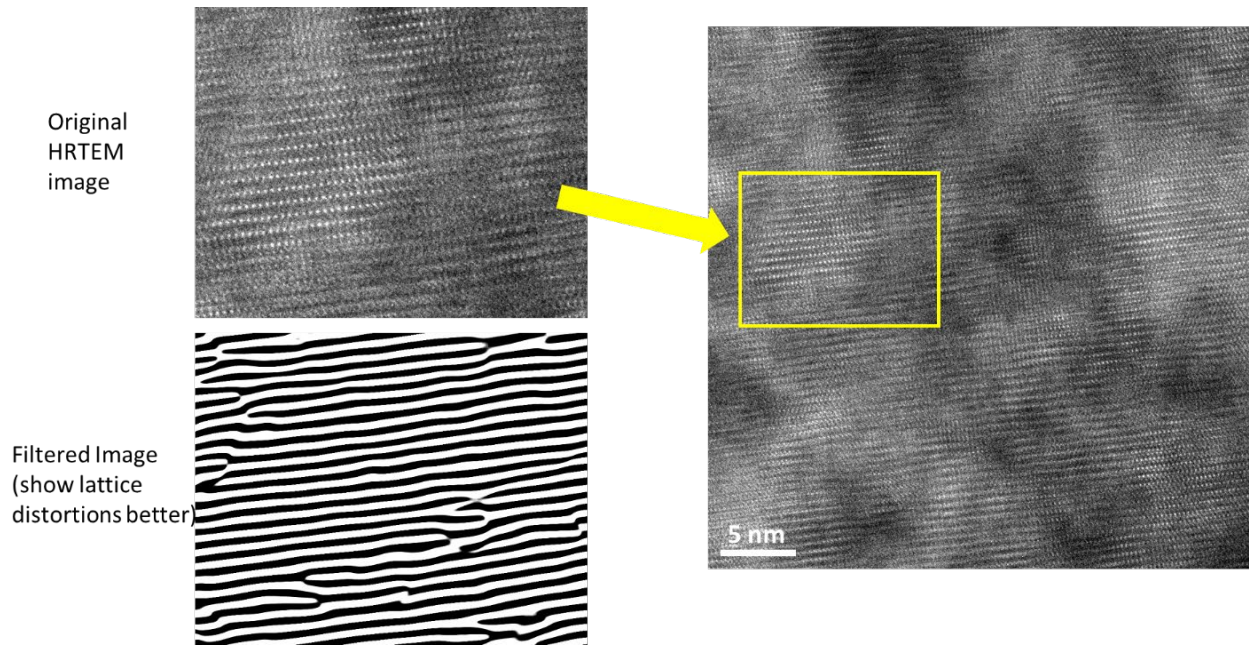


Figure 2-6 Example of an HRTEM and the corresponding filtered image showing the lattice distortions introduced by the extended defects such as dislocations.

Theoretically, the resolution of a TEM is related to the wavelength of the electron ($< 1 \text{ \AA}$). However, aberration factors limit the resolution (a few \AA) of TEM and result in image deterioration. The two types of aberrations that can affect TEM image quality are spherical aberrations and chromatic aberrations⁵⁹. Spherical aberration occurs due to the increased refraction at the edge of the lens versus the center and results in rays not converging on the same focal point. On the other hand, chromatic aberrations stem from the fact that the electron beam is not perfectly monochromatic. The degree to which the lens refracts the beam depends on the wavelength of the beam. It is difficult to make the beam converge at the same point. In this dissertation, the lattice structure of post-annealing extended defects is investigated by using the Argonne Chromatic Aberration-corrected (ACT) TEM, which is an FEI Titan TEM equipped with a CEOS Cc/Cs corrector on the imaging side of the column to correct both spherical and chromatic aberrations. The Cc/Cs

corrector provides greatly improved resolution and is extremely helpful for understanding the defect structures.

2.2.2. Scanning Transmission Electron Microscopy

Scanning Transmission Electron Microscopy (STEM) operates under a different mode compared to conventional TEM. As shown in figure 2-5 on the right, unlike the TEM where the electron beam exposes the whole sample, the electron beam in STEM is focused by the condenser lens to a small spot on the sample. The beam is then scanned across the sample, scattered, and detected by different detectors such as bright field (BF), and high angle annular dark field (HAADF). Previously, it is discussed that the diffraction contrast in TEM relies on the misorientation between grains. Similarly, defects such as dislocations in the sample also scatter electron more compared to the neighboring defect-free materials. Since the BF detector collects beams with a small scattering range, the defect-free materials will show bright contrast and the dislocations will show dark contrast in the STEM BF image. Based on the Burgers vectors, a specific dislocation will not show contrast in the STEM BF image if the sample is tilted to a certain diffraction condition. This phenomenon is known as the contrast invisibility criterion, where dislocations are completely invisible when the Burgers vector (\mathbf{b}) is orthogonal to the diffraction vector (\mathbf{g}) (i.e. $\mathbf{g} \cdot \mathbf{b} = 0$) [28]. For example, pure edge dislocations possess a Burgers vector of $1/3 \langle 11\bar{2}0 \rangle$ and would not show contrast if the diffraction vector \mathbf{g} equals $\langle 0002 \rangle$. While pure screw dislocations possess a Burgers vector of $\langle 0001 \rangle$ and would not show contrast if the diffraction vector \mathbf{g} equals $\langle 11\bar{2}0 \rangle$. Figure 2-7 shows an example of the STEM BF images with $\mathbf{g} = \langle 0002 \rangle$ and $\mathbf{g} = \langle 11\bar{2}0 \rangle$ from the Mg implanted GaN after annealing at 1300 °C for 10 minutes. The method of taking STEM images by tilting the sample to achieve a specific diffraction condition is

often referred to as two beam condition STEM imaging. In this dissertation, two beam condition STEM imaging is employed to categorize the post-annealing residual defects based on their nature of screw, edge, or mixed behavior.

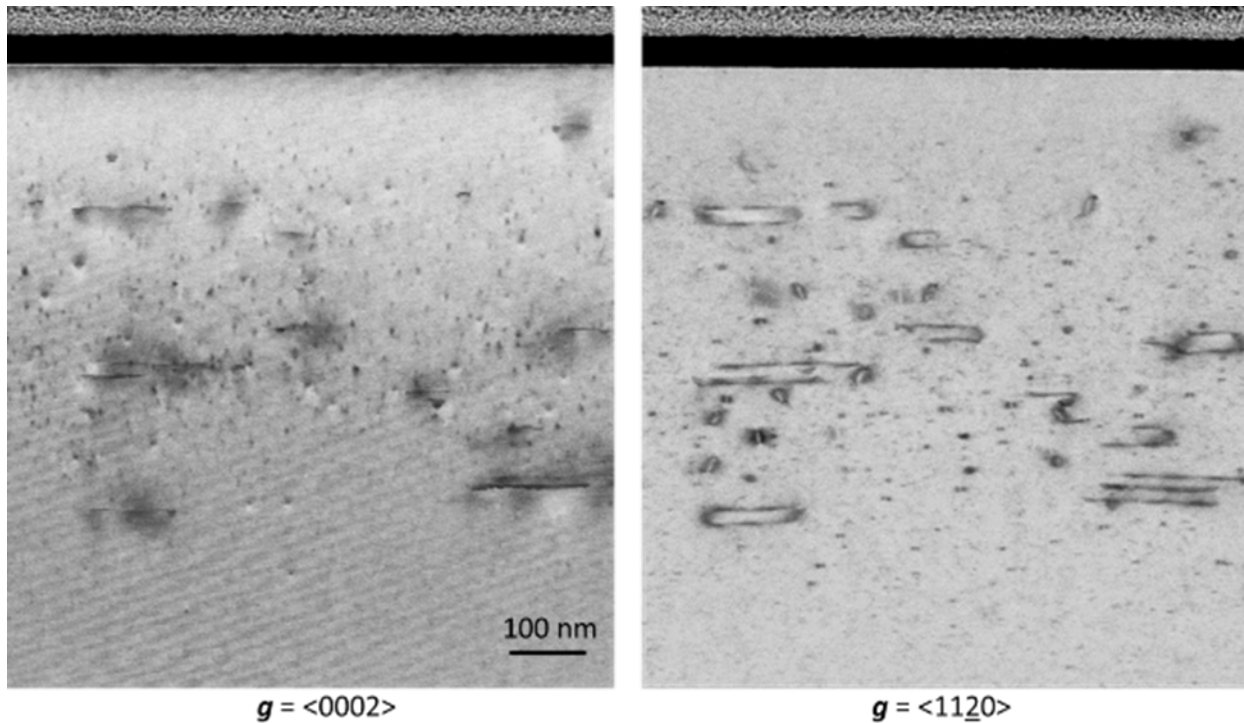


Figure 2-7 STEM BF images with $g = \langle 0002 \rangle$ and $g = \langle 11\bar{2}0 \rangle$ from the Mg implanted GaN after annealing at 1300 °C for 10 minutes.

On the other hand, STEM mode also allows chemical analysis as the microscope is usually equipped with energy dispersive X-ray spectroscopy (EDX). When the focus high-energy electron beam hits the sample, it ionizes the inner shell electron from the atoms in the sample and creates a vacancy. Since the inner shell is at a lower energy level compared to the outer shell, the high-energy electron on the outer shell tends to fill in the vacancy and release energy (emitting characteristic X-rays) as it relaxes. The energy of the emitted X-ray from the transition process is unique to each element and can be used to identify the elements that are present. In this dissertation,

EDX spectra is generated to understand the interaction between the Mg dopants and the post-annealing residual defects. Eliminating defects that passivate Mg from being electrical active is important for improving the dopant activation efficiency and ultimately the device performance.

2.3 Electrical Characterization Techniques

After Mg dopant activation, metal contacts are deposited on the samples to fabricate devices for electrical characterization.REF NRL For semiconductor devices, the device performance largely depends on properties such as resistance, carrier concentration, and mobility. These properties also help to justify the effectiveness of the doping process. The Hall effect measurements in combination with current-voltage (I-V) measurements are the most common way to accurately determine those properties and are also universally utilized in the semiconductor industry.

2.3.1 Hall Effect Measurements

To observe the Hall effect, a sample is subjected to a magnetic field that is orthogonal to its surface in z-direction, as illustrated in Figure 2-8. A current is applied to the sample perpendicular to the magnetic field and the charged carriers move in the x-direction. The moving charge carriers will deflect due to the magnetic field, which is along the y-direction.

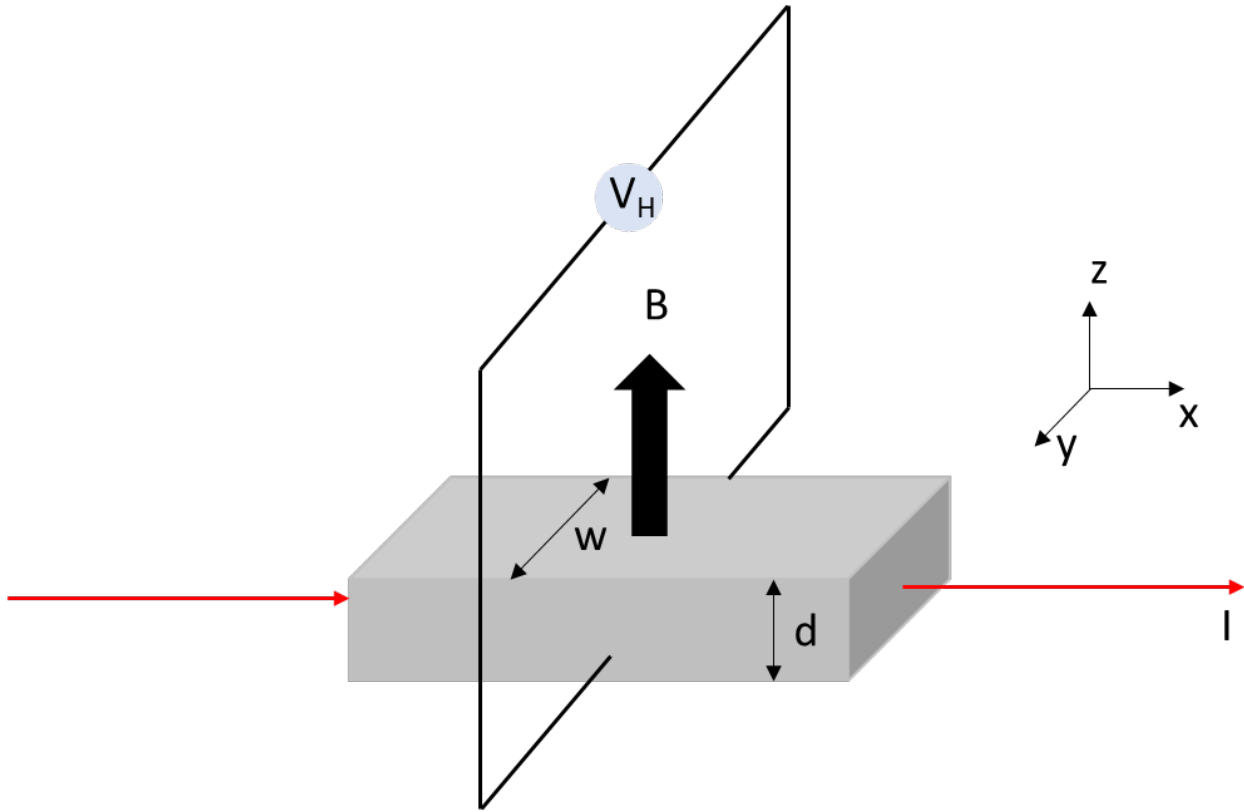


Figure 2-8 Schematic of the theory behind the Hall effect.

The moving charges will be deflected in opposite directions along the y-axis. Positively charged particles (holes) move to one edge, and the negatively charged particles (electrons) move to the opposite edge. An electric field (E) is created due to the charge separation and is inducing another force on the moving carriers in the direction opposite to the magnetic force. The net force experience by the charged carriers is Lorentz force (F), given by the following equation:

$$F = Eq + vq \times B \text{ eq. (2)}$$

Where v is the drift velocity of the charge carriers, B is the magnetic field and q is the elemental charge (1.6×10^{19} C). At equilibrium, Lorentz force is 0 so that:

$$E = -vB \rightarrow V_H = vBw \text{ (3)}$$

The current density J can be written as

$$J = nqv \quad (4)$$

Where n is the charge carrier density, q is the elemental charge and v is the drift velocity.

If one substitutes v with J into the previous equation, it will end up with:

$$E = -\frac{JB}{nq} \quad (5)$$

Finally, the Hall coefficient (R_H) is defined as:

$$R_H = \frac{1}{nq} = \frac{V_H d}{BI} \quad (6)$$

The magnitude of the Hall voltage is inversely proportional to the carrier concentration and the sign of this voltage indicates the dominant carrier type. For electron conductivity, the Hall coefficient is negative, and the coefficient is positive for hole conduction. The Hall coefficient, along with the resistivity ρ_s of the material, is needed to determine the carrier concentration (n) and mobility (μ):

$$n = \frac{1}{qR_H} \quad (7)$$

$$\mu = \frac{R_H}{\rho_s} \quad (8)$$

Chapter 3 Mg Implantation into Heteroepitaxial GaN with Activation Using Multi-Cycle Rapid Thermal Annealing

3.1 Motivation

This chapter provides an initial assessment of the defect evolution during the Multi-Cycle Rapid Thermal Annealing (MRTA) process, in order to understand the difference in carrier mobility found in electrical measurements from the two samples despite showing the same activation efficiency with different MRTA process parameters (cycle time, peak temperature etc.). A systematic characterization method with a combination of high-resolution x-ray scattering and transmission electron microscopy is developed. The presence of the extended defects after the MRTA sequence is revealed and their characteristics are analyzed. High-resolution x-ray diffraction together with dynamical simulation provides quantitative information on the implant-induced strain. X-ray-based reciprocal space map confirms that the elastic strain caused by implantation is purely along the implant direction ([0001] direction). Inverse Fourier transform images were used to provide direct visualization of extended defects at different depths from the two samples, which shows direct correlation with the difference in mobility observed in the electrical measurements.

3.2 Experimental Details

2- μm (0001) oriented unintentionally doped GaN layers were deposited on a-plane (11 $\bar{2}$ 0) sapphire. The GaN epi-wafers were capped with a thin MOCVD AlN layer. Multiple energy implants were chosen so that an approximately flat profile is generated over the depth of 0.4 μm with a total dose of $7 \times 10^{14} \text{ cm}^{-2}$. The intended Mg implant profile matches that from Stopping and

Range of ions in Matter (SRIM) ⁶⁰ implant simulation software. After implantation, wafers were annealed using two variations of the MRTA technique in N₂ at 20 bar. Two samples (μ 20 and μ 40, as related to the mobility achieved for each annealing condition) studied in this work were both initially annealed at 1000 °C for one hour, in order to remove a part of the implantation damage ³⁸. After that, sample μ 20 utilized MRTA with fifteen cycles of 3.87 s at a peak temperature of 1420 °C (total time 58.7 s above 1340 °C), while sample μ 40 was subjected to thirty cycles at 0.24 s each with a peak temperature of 1341 °C (total time of 7.2s above 1340 °C). Standard electrical measurements had previously been performed to assess the properties of the ion implanted and annealed layers ³⁸. As noted in that earlier study, both samples showed high activation efficiency (~8%) but sample μ 40 exhibited a mobility of 40 cm²/(V·s) while sample μ 20 exhibited a mobility of 20 cm²/(V·s). Here, the structural characterization was performed using high-resolution x-ray scattering and transmission electron microscopy (TEM). The triple-axis x-ray measurements used a Jordan Valley (Bruker) D1, with an incident beam mirror to produce a parallel beam (Cu $\kappa\alpha_1$ radiation) as well as a Si (220) channel cut collimator. The scattered beam optics included a Si (220) channel cut crystal. Cross section TEM samples were prepared using Focused Ion Beam (Nova 600 SEM/FIB). TEM/STEM images were produced using a Titan S/TEM (FEI) system at 300 kV.

3.3 Results and discussion

High-resolution x-ray diffraction was performed to non-destructively assess the defect evolution in the implanted samples. Figure 3-1 shows a triple-axis scan for the as-implanted sample and the annealed samples. The measurements were performed in the ω :2 θ mode tracing along the

c-axis perpendicular to GaN (0004) peak in reciprocal space. The peak to the left of the main peak in Figure 3-1a corresponds to a layer with a tensile elastic strain along the [0001] direction. This results from elastic lattice distortions induced by intercalation of the implanted Mg and target (Ga or N) atoms knocked off lattice sites by the high energy ion beam during implantation.

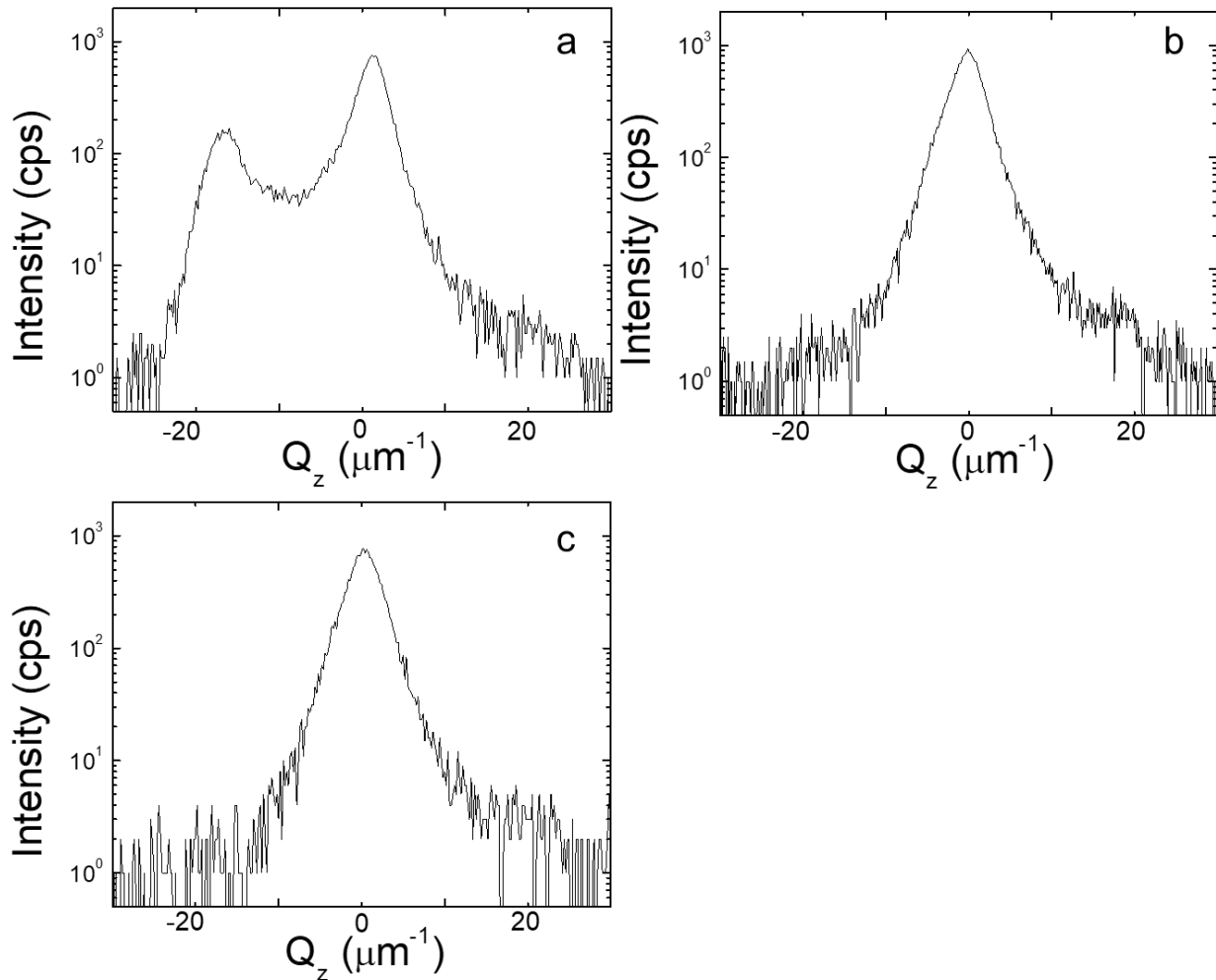


Figure 3-1 High-resolution x-ray diffraction $\omega:2\theta$ scan near the GaN (0004) peak for (a) the as implanted sample, (b) the sample $\mu 20$, and (c) the sample $\mu 40$. The as-implanted sample shows satellite peak corresponding to implant-induced strained layer.

The fact that no satellite peak is observed in Figure 3-1b and Figure 3-1c indicate that implant-induced elastic strain has been relieved after the MRTA processes. X-ray reciprocal space maps

were used to further confirm the extent of this lattice distortion. Figure 3-2a and 3-2b show the symmetric reciprocal space map of GaN (0004) and asymmetric reciprocal space map of GaN (10 $\bar{1}$ 4) respectively. In both maps, the point at (0, 0) corresponds to the GaN 0004 substrate reciprocal space lattice point (REL \bar{P}) and the point at around (-20, 0) is from the implant-induced strained layer. The two REL \bar{P} s are aligned vertically in both maps, indicating that both have the same in-plane lattice parameter, i.e., the strained layer is pseudomorphic with respect to the substrate within the resolution of these measurements - on the order of less than 0.04% difference in the in-plane lattice parameters of the implanted region and the underlying, unimplanted GaN.

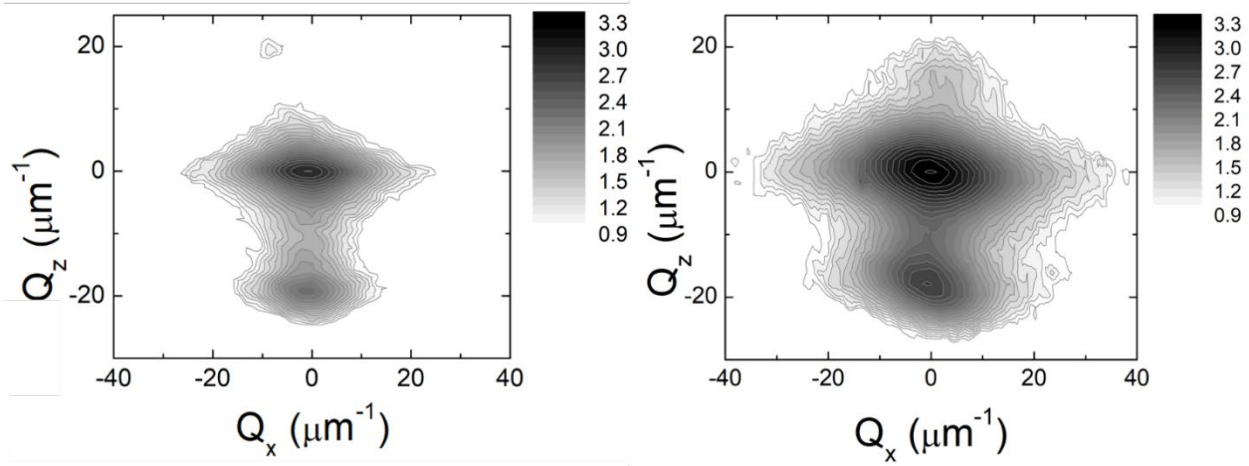


Figure 3-2 X-ray reciprocal space map for the as-implanted sample showing (a) the GaN (0004) REL \bar{P} , and (b) the (10 $\bar{1}$ 4) REL \bar{P} .

Therefore, it is concluded that the elastic strain is purely along the [0001] direction. In effect, the intercalated species expand the lattice, but the thick substrate (un-implanted GaN and the sapphire) constrains the implanted region such that there is only an out-of-plane, pseudomorphic deformation, in the same manner as an epitaxial layer is pseudomorphically strained with respect to the substrate with a different lattice parameter. X-ray dynamical simulations using Bruker RADS software provide quantitative information about the strain-inducing implant species and the elastic

deformation of the lattice during implantation. The experimental XRD data and the simulation from RADS are shown in Figure 3-3a. A good fit in the $\omega:2\theta$ scan was achieved and the elastic strain corresponding to the fit is plotted in Figure 3-3b together with the SRIM implantation recoil damage as well as the ion concentration as references. The strain distribution shows higher strain at above 2000 ppm in the first 300 nm but drops to below 500 ppm at a depth of 500 nm and closely follows the implant recoil damage profile, which supports the contention that the intercalated, implanted and knocked-on species are the primary contributors to the as-implanted strain formation.

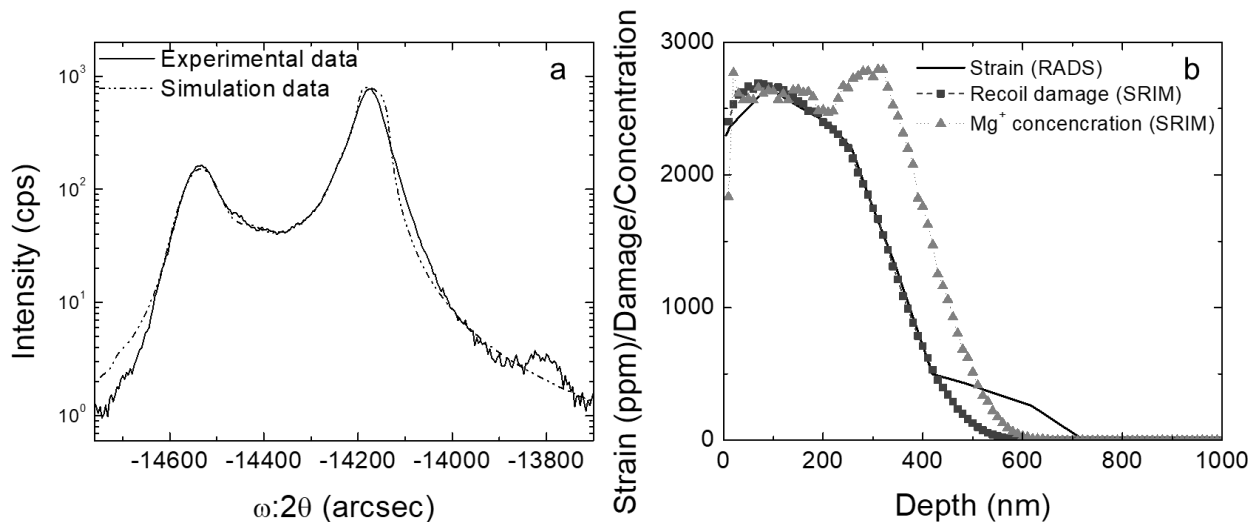


Figure 3-3 (a) High-resolution x-ray diffraction $\omega:2\theta$ scan fitted with dynamical simulation software Bruker RADS. (b) Simulated strain profile plotted with SRIM ion concentration and recoil damage profiles. The ion concentration and recoil damage are normalized to the strain for convenience.

The change in the implant-induced strain with the MRTA process is also demonstrated using reciprocal space maps. Figure 3-4a and 3-4b show the $(10\bar{1}4)$ reciprocal space maps for the as-implanted case and for $\mu 40$, including the sapphire $(22\bar{4}6)$ RELPs. Figure 3-4b, after the MRTA

annealing, shows the (1014) GaN reflection of $\mu 40$ with only the strain-free GaN remaining, the strain has been removed from the implanted region. This GaN peak is in the same location (with respect to the sapphire (2246)) as the unstrained portion of the GaN in the as-implanted case, confirming that the GaN lattice parameters have not changed with respect to the sapphire lattice due to the MRTA annealing process.

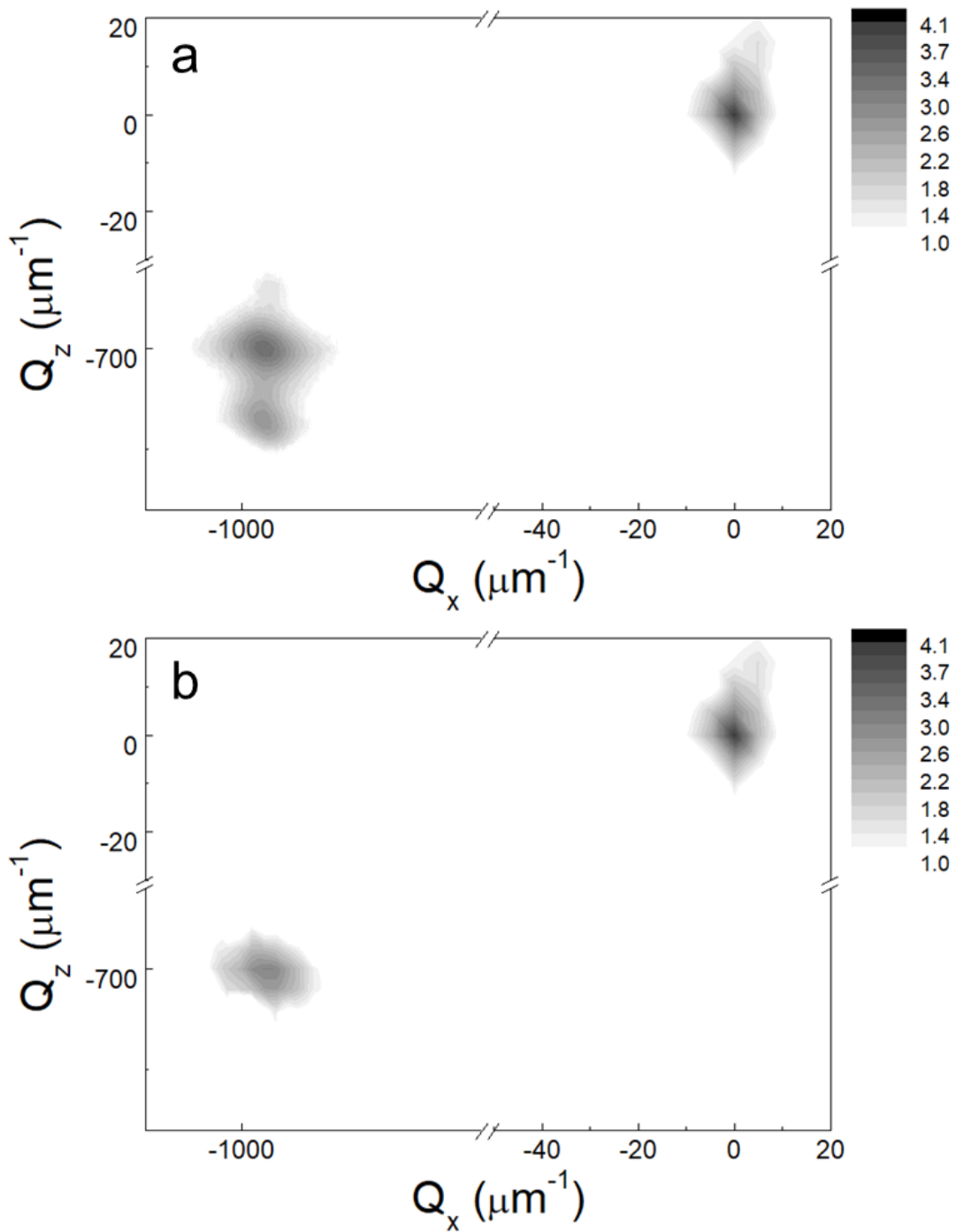


Figure 3-4 (a) RSM for as-implanted sample showing the $(10\bar{1}4)$ GaN RELP as well as the $(22\bar{4}6)$ sapphire RELP (b) RSM for sample $\mu 40$ showing the $(10\bar{1}4)$ RELP for GaN as well as the $(22\bar{4}6)$ RELP for sapphire.

X-ray rocking curves under triple-axis conditions were then obtained to provide information about the evolution of defects. The full width at half maximum (FWHM) as well as full width at 0.01 maximum (FW0.01M) is typically used as a measure of the defects in such structures^{51, 52}. As shown in Table 3, a decrease in both the FWHM and the FW0.01M is observed after the MRTA annealing process compared to implanted, un-annealed material (as well as non-implanted, non-annealed material which was the same as the as-implanted, un-annealed case). It shows that the widths even after annealing is still broad. The difference between the as-implanted sample and the two annealed sample is within the step size of the measurement (40 arcsecs).

	FWHM (arcsec)	FW0.01M (arcsec)	Mobility (cm²/V·s)
As-implanted	329	1390	N/A
Sample μ20	303	1210	20
Sample μ40	298	1130	40

Table 3. FWHM/FW0.01M extracted from the triple-axis rocking curve results and the mobility measurement results from earlier studies³⁸.

Unfortunately, besides implant-related defects, the material system (GaN on sapphire) used here also possesses a great number of intrinsic defects that can also affect triple-axis rocking curve width. Implantation into high-quality substrates or homoepitaxial layers on such high-quality substrates would better distinguish the change due to implantation and annealing from that due to an initially high concentration of heteroepitaxial defects. The quality of free-standing GaN substrate has improved drastically over the past few years. Homoepitaxial film on high-quality GaN wafers contains much fewer intrinsic defects. Rocking curves from these structures are expected to show relatively narrow initial width. As a result, peak broadening due to the implant-induced defects can be better extracted and the effect of annealing on the crystalline quality is more

conspicuous. On the other hand, eliminating the heteroepitaxial defects is conducive to the reduction of post-annealing remnant defects and therefore, improving the mobility.

To better understand the microstructural evolution and assess whether there are quantitative defect differences in $\mu 20$ and $\mu 40$, transmission electron microscopy (TEM) is employed to determine the nature of the extended defects. In TEM, based on the contrast invisibility criterion, dislocations are completely invisible when the Burgers vector (\mathbf{b}) is orthogonal to the diffraction vector (\mathbf{g}) (i.e. $\mathbf{g} \cdot \mathbf{b} = 0$)³¹. Pure edge dislocations possess a Burgers vector of $1/3 \langle 11\bar{2}0 \rangle$, pure screw dislocations have a Burgers vector $[0001]$ and mixed dislocations exhibit a Burgers vector of $1/3 \langle 11\bar{2}3 \rangle$ ⁶¹. Figure 3-5 shows cross-section TEM bright field images with Figure 3-5a depicting $\mathbf{g} = \langle 0002 \rangle$ for $\mu 20$; Figure 3-5b shows $\mathbf{g} = \langle 0002 \rangle$ for $\mu 40$; Figure 3-5c is $\mathbf{g} = \langle 11\bar{2}0 \rangle$ for $\mu 20$ and Figure 3-5d has $\mathbf{g} = \langle 11\bar{2}0 \rangle$ for sample $\mu 40$. These images show two highly defective regions, one near the GaN/sapphire interface and the other one within the top 500 nm region, which corresponds to the implant recoil damage region. The GaN/sapphire interface shows a high density of dislocations to compensate for the lattice mismatch between those two during the MOCVD growth. A few inclined black features are observed which correspond to threading dislocations associated with the epitaxial GaN deposition. Figure 3-5a and 3-5b (0002) show circular features in the top 500 nm region in both sample $\mu 20$ and sample $\mu 40$. The depth of these features matches the depth of the Mg implant recoil damage region. These circular defects are not present in implanted, un-annealed structures; therefore, these are post-annealing extended defects. As reported by other groups, these extended defects are relatively stable and very difficult to remove^{49, 50}. In 5c and 5d ($11\bar{2}0$), however, the extended defects are not observed. For both samples, extended defects are observed when $\mathbf{g} = \langle 0002 \rangle$, but absent when $\mathbf{g} = \langle 11\bar{2}0 \rangle$. The invisibility of extended defects under $\mathbf{g} = \langle 11\bar{2}0 \rangle$ suggests that the Burgers vector for post-annealing extended

defects are orthogonal to $\langle 11\bar{2}0 \rangle$, indicating they have an observable screw component.

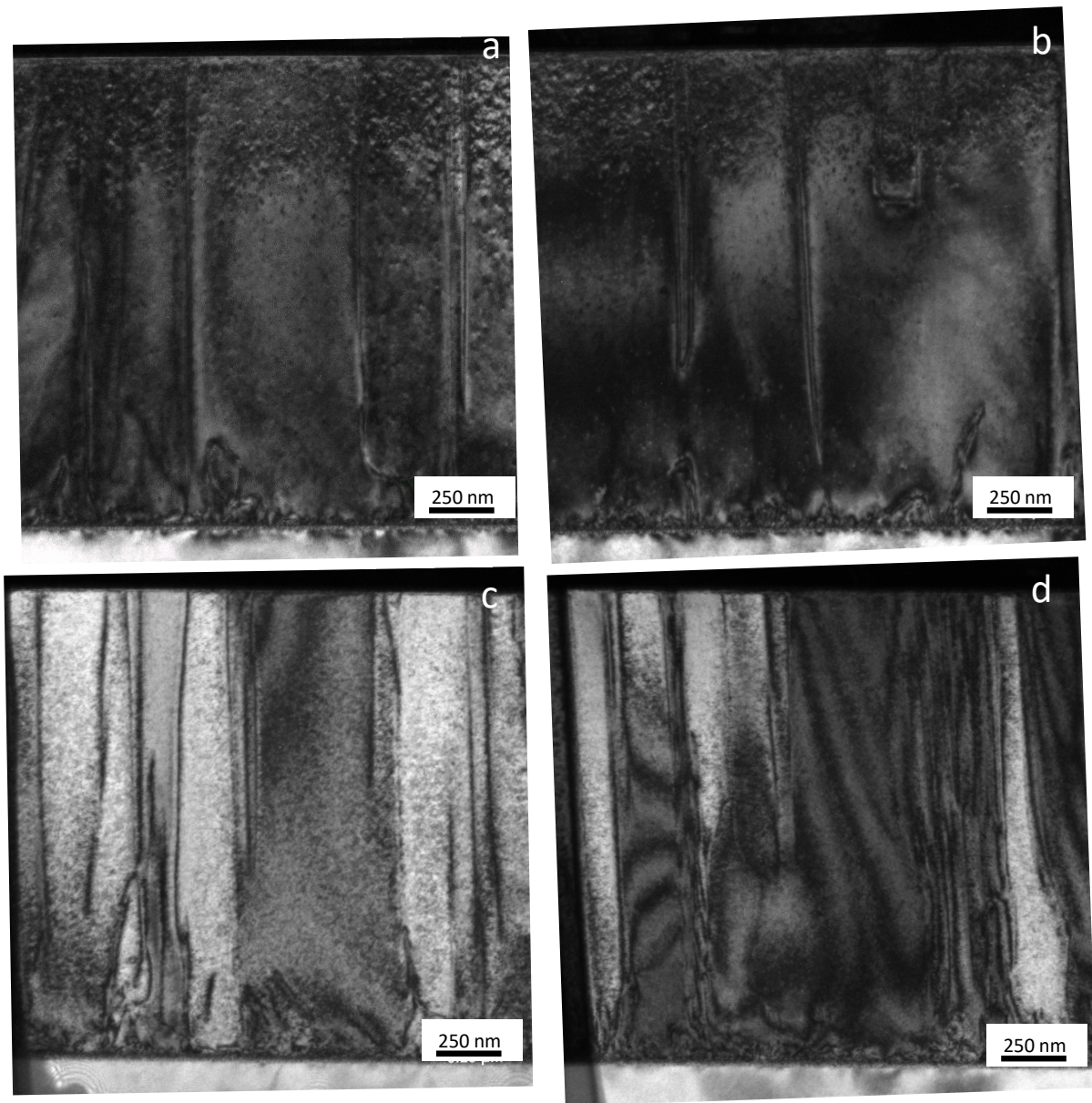


Figure 3-5 Cross-section TEM two beam condition bright field images with different diffraction vectors, (a) sample $\mu 20$, $g = \langle 0002 \rangle$ (b) sample $\mu 40$, $g = \langle 0002 \rangle$, (c) sample $\mu 20$, $g = \langle 11\bar{2}0 \rangle$, (d) sample $\mu 40$, $g = \langle 11\bar{2}0 \rangle$

To better quantify the residue defect concentration and reduce the sample bending contrast observed in the images in Figure 3-5, scanning transmission electron microscope (STEM) mode

was employed. The (0002) STEM images are shown in Figure 3-6 and these images were taken near the implantation region with the same diffraction vectors as above. The depths lines in figure 3-6a and 3-6b indicate 3 regions: the center of the implanted region (200 nm), the edge of the implanted region (500 nm), and the non-implanted region (800 nm). Localized defect information can be extracted with Fourier filtering technique (shown in figure 3-8). The defect density measurement was performed using the intersection method ⁶² with five different measurements for each sample. The defect densities of both samples are on the order of $10^{10}/\text{cm}^2$ but sample $\mu 20$ has an average concentration of $3.5 \times 10^{10} \text{ cm}^{-2}$ while $\mu 40$ has a lower content of approximately $2.6 \times 10^{10} \text{ cm}^{-2}$. This difference, albeit small, further supports the relationship among MRTA process conditions, defect densities, and p-type carrier mobility.

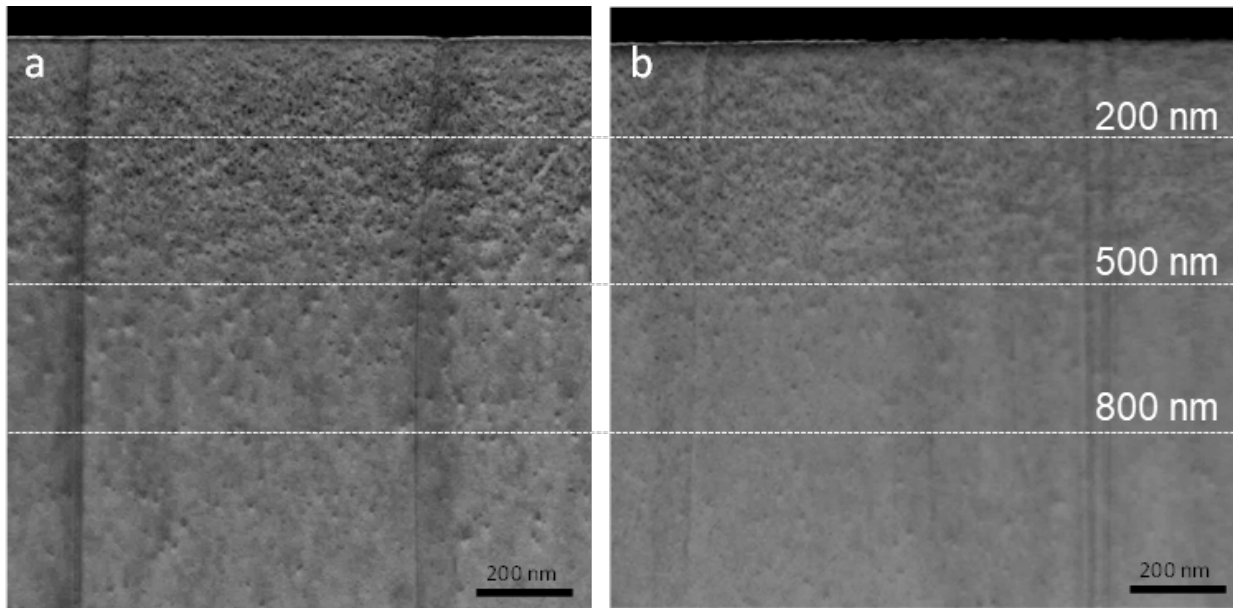


Figure 3-6 Cross-section STEM two beam condition bright field images taken near the implanted region, and the three depths indicate where the images in figure 3-8 are obtained, (a) sample $\mu 20$ with $g = \langle 0002 \rangle$, (b) sample $\mu 40$ with $g = \langle 0002 \rangle$

Another technique based on the electron microscopy measurements was employed to reveal

the presence of the defects at different depths. This technique utilizes inverse Fourier transform TEM images to help visualize the presence of remnant defects ⁶³. The process starts from a conventional high-resolution TEM lattice image (Figure 3-7a) to which a Fast Fourier Transform is applied (Figure 3-7b). Mask filtering technique is used to select certain spatial frequencies (circles in 3-7b) in reciprocal space before reconstructing a real space lattice image using the Inverse Fourier Transform (Figure 3-7c).

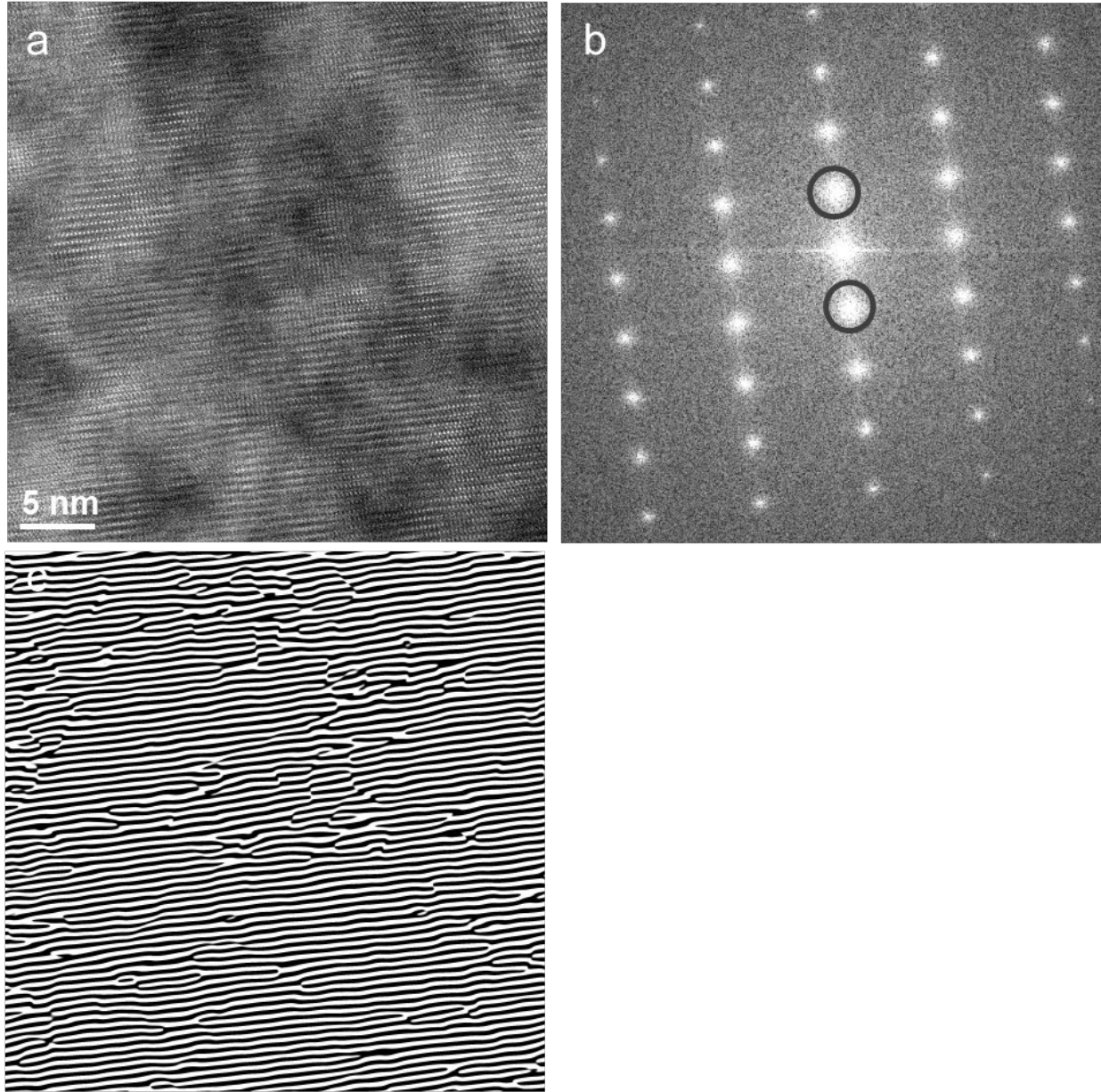


Figure 3-7 (a) High-Resolution TEM lattice image of the implanted region, (b) FFT of (a) before applying the mask (circles), (c) Inverse Fourier transform lattice image.

Figure 3-8 show residue defect characteristics using Fourier filtering in the 3 regions shown in figure 3-6a and 3-6b. The Figure 3-8a and 3-8d show the (0001) inverse Fourier transform images of sample $\mu 20$ and sample $\mu 40$ at the depth of ~ 200 nm. According to the TEM results, the area belongs to the implant-induced highly defective region. As a result, both samples show a large

number of extended defects. Figure 3-8b and 3-8e show the (0001) inverse Fourier transform images of sample $\mu 20$ and sample $\mu 40$ deeper into the sample at ~ 500 nm. According to the SRIM implantation profile and TEM images, the location is close to the edge of the implantation zone.

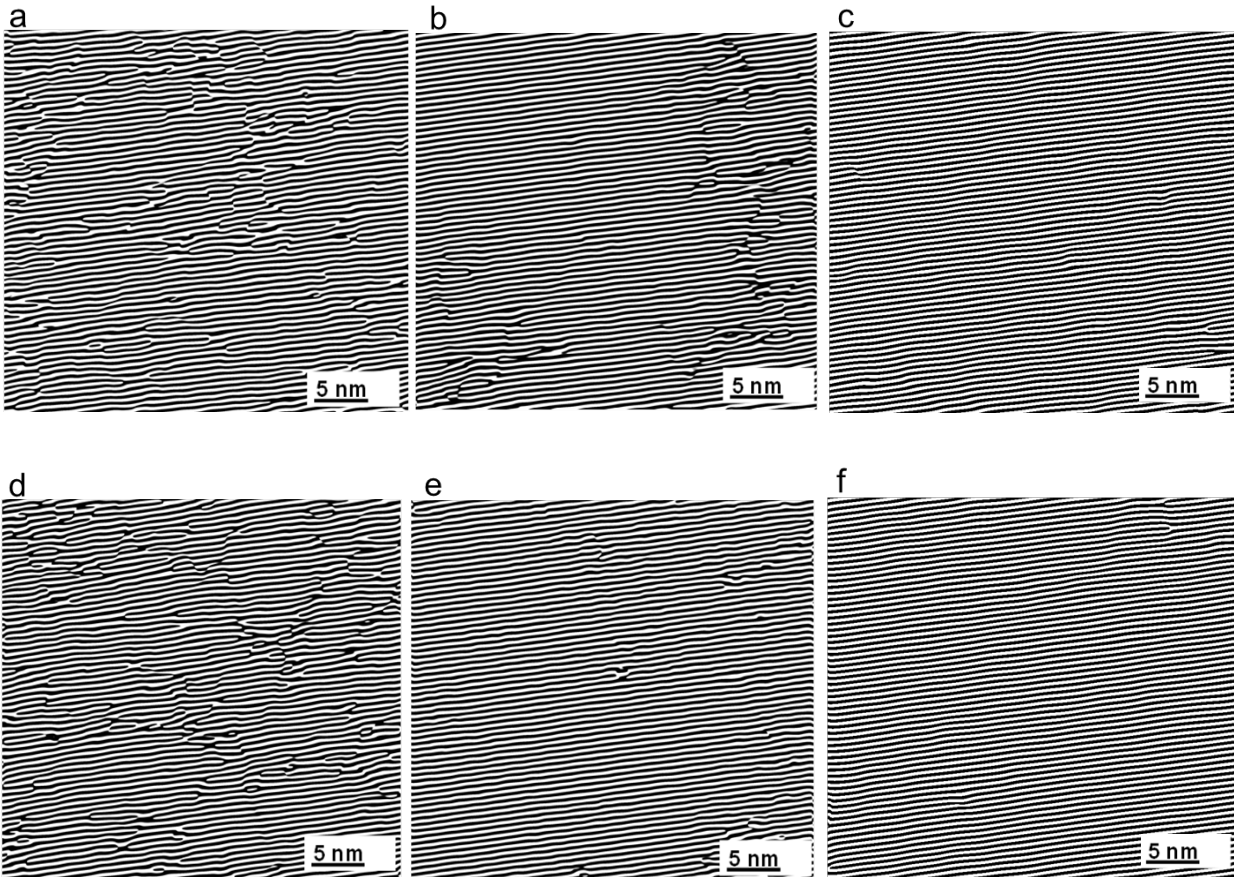


Figure 3-8 (0001) inverse Fourier transform TEM images revealing post-annealing extended defects at different depths for sample $\mu 20$, (a) inside the implantation zone (~ 200 nm), (b) the edge of the implantation zone (~ 500 nm), (c) outside the implantation zone (~ 800 nm) and for sample $\mu 40$, (d) inside the implantation zone (~ 200 nm), (e) the edge of the implantation zone (~ 500 nm), (f) outside the implantation zone (~ 800 nm).

In general, a clear decrease in defect density was observed. Both samples show lower defect density at 500 nm when compared to that at 200 nm depth. Furthermore, sample $\mu 20$ possesses a higher density of such extended defects than sample $\mu 40$ which is nearly defect-free at this depth.

Figure 3-8c and 3-8f show the (0001) inverse Fourier transform images outside the implantation zone, at ~800 nm for the two samples. They show there is no extended defect existing. The inverse Fourier transform images show clear differences near the edge of the implantation zone. The difference in defect density correlates to the XRD rocking curve results, confirming that sample $\mu 40$ shows better quality than $\mu 20$. Considering the two samples were annealed using very different recipes, the total time that sample $\mu 20$ was held at elevated temperature is much longer (58.7s vs 7.2s). It is speculated that this temperature difference promotes the coalescence of implanted point defects to form extended defects, which later impacts the hole mobility. Although the MRTA process achieved a high dopant activation efficiency, post-annealing extended defects still remain, indicating that further improvements in the MRTA parameter time distribution can be achieved. Both cycle period and peak temperature can be optimized to reduce the number of extended defects, which is expected to have a significant impact on further improving device performance.

3.4 Summary

In conclusion, x-ray scattering and electron scattering techniques are used to assess the implant-induced defects in GaN/sapphire heterostructure after the MRTA process. High-resolution x-ray diffraction together with dynamical simulation provides quantitative information on the implant-induced strain across the GaN thickness. X-ray-based reciprocal space map confirms the elastic strain caused by implantation is purely along the [0001] direction and is later removed during the MRTA process. Two beam condition TEM/STEM images reveal that the post-annealing extended defects are circular defects with an observable screw component. Inverse Fourier transform images provide direct visualization of extended defects at different depths from HRTEM measurements and suggest the defect density is affected by the MRTA cycle parameters. Even

given the high activation efficiency achieved, extended defects are still present after the MRTA process. Further study on reducing the extended defects through MRTA optimization is expected to further improve the p-type conductivity for the development of high-performance GaN p-n junction devices. To better understand the defect evolution during the dopant activation anneal, a high-quality homoepitaxial GaN structure is necessary.

Chapter 4 Strain Recovery and Defect Characterization in Mg Implanted Homoepitaxial GaN with Ultra-High-Pressure Annealing

4.1 Motivation

As discussed in the previous chapter, Mg implanted GaN/sapphire structures possess a high intrinsic defect density ($>10^8 \text{ cm}^{-2}$)^{64, 65}. Using high-quality GaN substrates can promote homoepitaxial GaN film growth with a much lower intrinsic defect concentration ($< 10^6 \text{ cm}^{-2}$) and is anticipated to further improve device performance as well as the ability to separate implant-induced defects from those in the pre-existing hetero-epitaxial structure. This chapter demonstrates the study of implant-induced strain recovery and post-annealing defect evolution in Mg implanted homoepitaxial GaN grown on high-quality ammonothermal GaN substrates with ultra high-pressure annealing (UHPA). The relaxation process of the implant-induced strain was investigated by quantifying the residual strain as a function of annealing temperature and annealing time. Post-annealing extended defects were further characterized. Understanding the nature of the extended defects as well as the change of their density and configurations due to the annealing process is expected to help improve the electrical performance.

4.2 Experimental Details

In this study, high-quality (0001) GaN substrates grown by the ammonothermal method were used. GaN epitaxy films with a thickness of $1.5 \mu\text{m}$ were grown via metal organic chemical vapor deposition (MOCVD) on high-quality ammonothermal GaN substrates. The magnesium ions ($2 \cdot 10^{14} \text{ cm}^{-2}$ dose) were implanted at room temperature at an angle of 7° and at an accelerating voltage of 100 keV. Using the SRIM simulation software⁶⁰, the peak concentration was calculated

to be $1.6 \cdot 10^{19} \text{ cm}^{-3}$ at a depth of $\sim 100 \text{ nm}$. Post-implantation annealing was performed at three different temperatures ($700 \text{ }^\circ\text{C}$, $1000 \text{ }^\circ\text{C}$, and $1300 \text{ }^\circ\text{C}$) for 10 min and 100 min. A high N_2 pressure of 1 GPa was applied to prevent GaN from decomposition without using a dielectric cap.

Structural characterization was performed by a combination of x-ray scattering and electron scattering techniques. The lattice distortions and crystalline quality were assessed by High-Resolution X-ray Diffraction (HRXRD) and X-ray topography (XRT). Triple axis X-ray measurements used a Jordan Valley (Bruker) D1 diffractometer, with an incident beam mirror to produce a parallel beam ($\text{Cu } \alpha_1$ radiation), followed by a Si (220) channel cut collimator. The scattered beam optics included a Si (220) channel cut crystal. Synchrotron double crystal x-ray topography measurements were performed at the 1-BM Beamline of the Advanced Photon Source, Argonne National Laboratory with a photon energy of 8.05 keV. The first crystal was a highly asymmetric Si (333) beam expander and the sample (2nd crystal) was oriented for diffraction of the (11 $\bar{2}$ 4) reflection. Detailed information of the post-annealing defects was obtained using Transmission Electron Microscope (TEM). TEM samples were prepared using Focused Ion Beam (Nova 600 SEM/FIB). Scanning Transmission Electron Microscope (STEM) images were taken using a Titan (FEI) system at UCLA. High-Resolution TEM images were taken using the Argonne chromatic aberration-corrected TEM at the Center for Nanoscale Materials, Argonne National Laboratory.

4.3 Results and discussion

X-ray reciprocal space maps (RSM) show that satellite peaks were observed at lower angles of the substrate GaN peak, indicating expansion perpendicular to the surface. Figures 4-1a and 4-

1b show the symmetric reciprocal space map measured near GaN (0004) reciprocal space lattice point (REL_P) and asymmetric RSM measured near GaN (10 $\bar{1}$ 4) REL_P.

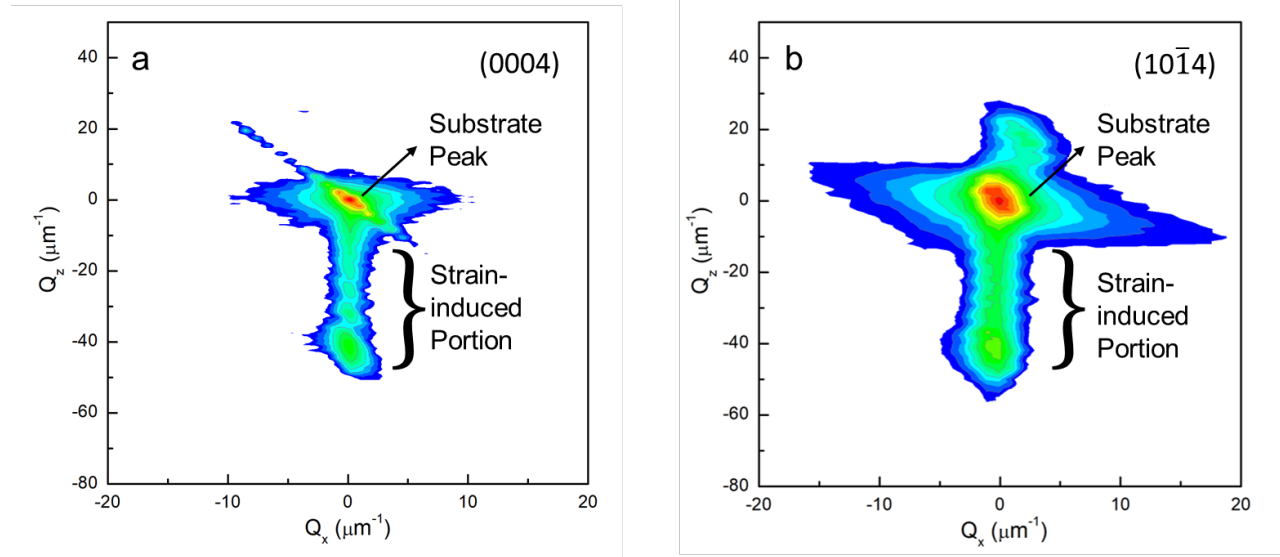


Figure 4-1 X-ray reciprocal space map for the as-implanted sample showing (a) the GaN (0004) REL_P, and (b) the (10 $\bar{1}$ 4) REL_P.

In both maps, the point (0, 0) corresponds to the position of the underlying, unimplanted GaN substrate REL_P. The implant-induced strained layer REL_Ps extend to (0, -50). The presence of the intensity at these lower angles is indicative of lattice distortion as a result of the implantation-induced strain^{66, 67, 68}. In both maps, REL_Ps of the implant-induced strained layer are aligned vertically with the REL_P of the underlying unimplanted GaN. This confirms that the implant-induced strain is only along the vertical ([0001] direction) and the strained layer has a larger c-lattice parameter than bulk GaN. This is due to the intercalation of implants and target atoms knocked off lattice sites expanding the lattice. However, the a-lattice parameter is constrained by the thick unimplanted GaN; therefore the implant-induced strain is pseudomorphic. The results are consistent with the study of Mg implanted GaN on sapphire shown in chapter 3⁶⁵, as well as the earlier studies on implanted GaAs^{51, 52}. To quantify the elastic strain, Bruker RADS software⁶⁹ is

employed to model the strain profile. The triple-axis $\omega:2\theta$ line scan near GaN (0004) peak of the as-implanted sample is shown in Figure 4-2a. A simulated $\omega:2\theta$ scan is superimposed over the experimental result in Figure 4-2a. $\omega:2\theta$ scans from the 700 °C samples that were annealed for 10 min or 100 min are plotted together in Figure 4-2b (with the as-implanted sample included as a reference). After annealing at 700 °C for only 10 min, the position of the satellite peak shifts toward the main peak.

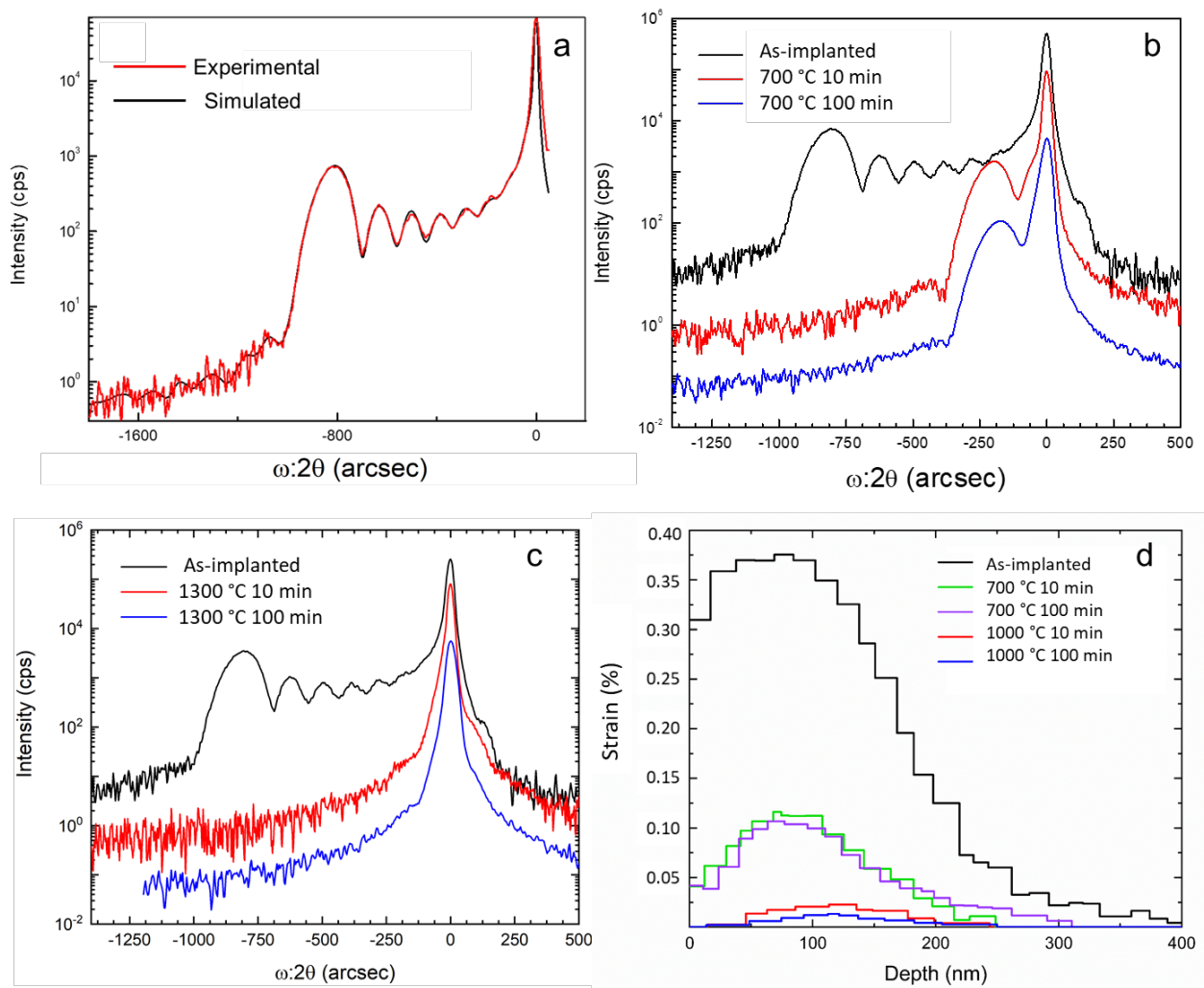


Figure 4-2 (a) Triple axis XRD $\omega:2\theta$ scan of the as-implanted sample and simulated scan using RADS software. (b) Triple axis XRD $\omega:2\theta$ scans after annealing at 700 °C for 10 min and 100 min.

(c) Triple axis XRD $\omega:2\theta$ scans after annealing at 1300 °C for 10 min and 100 min. (d) Simulated strain profile before and after annealing. No residue strain after annealing at 1300 °C for 10 min and 100 min.

Qualitatively, this indicates a significant reduction of the implant-induced elastic strain as the lattice parameter of the strained layer gets close to that of the unimplanted GaN. Quantitatively, it is observed that $\sim 2/3$ of the initial strain was recovered by ten minutes, as shown in Figure 4-2d with a reduction in the maximum strain from 0.375% to 0.116%. The strain profiles for simulations of all the annealed samples are also determined and shown in Figure 4-2d. The same process was applied to all the subsequently annealed samples to understand the influences of annealing temperature and time on the elastic strain recovery. However, annealing at 700 °C for a longer time (100 min) reduced the strain further by only a small additional amount. The strain profile shows an additional small amount (0.012%) of strain was recovered – about 0.104% remains, corresponding to the small additional shift in the satellite peak. This suggests that the point defect reconfiguration exhibits an initial fast transient, followed by a continued slower change in the implant-induced strain. A recent study suggested that using electrical measurements, annealing at 700 °C for a few minutes modified the electrical performance of their p-n diodes and suggested that this change was due to the reduction of implant-induced point defects⁷⁰. My results support the notion that some of the implant point defect concentration is reduced, but not all of it as some strain remains. Annealing at 1000 °C led to greater initial, but also not complete, elastic strain recovery. As shown in Figure 4-2d, approximately 0.023% and 0.0135% still remained after annealing for 10 min and 100 min. This is evidenced by the presence of the “shoulder” on the left side of the main peak in the $\omega:2\theta$ scans and again suggests a rapid initial strain recovery/defect reconfiguration with little additional change after a longer time. Complete recovery of the elastic

strain was observed both after annealing at 1300 °C for 10 min and 100 min, and only the (0004) GaN peak was observed, as shown in Figure 4-2c. This indicates the complete recovery of the strain, which corresponds to the displaced atoms moving back to their lattice sites or forming extended defects after annealing.

To assess the extent to which extended defects form due to annealing, triple-axis x-ray rocking curve measurements were performed using the (0004) and (10 $\bar{1}$ 4) reflections. The full width at half maximums (FWHM), as well as the full width at 0.01 maximum (FW0.01M) of the rocking curves, are summarized in Table 1.

FW0.01M (FWHM) [arcsec]	Unimplanted	700 °C 10 mins	1000 °C 10 mins	1300 °C 10 mins	1300 °C 100 mins
(0004)	46 (14)	51 (14)	61 (20)	74 (14)	74 (25)
(10$\bar{1}$4)	45 (12)	43 (14)	66 (14)	156 (71)	66 (15)

Table 4. FW0.01M (FWHM) from the triple-axis rocking curve scans.

These peak widths are typically used as a measure of the crystalline quality of the GaN. FWHM and FW0.01M both reflect the amount of distortion caused by lattice imperfections/defects in the materials. However, when assessing the crystalline quality for high-quality structures, the FWHMs can be indistinguishable while the FW0.01M differences are more profound, as demonstrated in an earlier study evolving hydrogen implanted Si⁷¹ as well as for misfit dislocations in InGaAs/GaAs structures⁷². The FWHM of both (0004) and (10 $\bar{1}$ 4) of the unimplanted sample is among the smallest that has been reported in the literature, showing the homoepitaxial GaN has very high crystalline quality. It should be noted that even after annealing at 1300 °C, the crystalline quality is still higher than what is observed in implanted and recovered heterostructures as the

FWHM/FW0.01M is an order of magnitude lower than the implanted and annealed GaN/sapphire heterostructures^[14]. On the other hand, a clear increase in FWHM/FW0.01M is noted in the (10 $\bar{1}4$) ω scans, particularly for the 1000 °C 10 min sample and the 1300 °C 10 min sample. This is indicative of an increasing amount of lattice distortion in the form of extended defects. Moreover, it is observed that the (10 $\bar{1}4$) FWHM and FW0.01M of the 1300 °C 100 min sample are much smaller than those of the 1300 °C 10 min sample. This is particularly interesting as it indicates an improvement in the crystalline quality after annealing at 1300 °C for an extended time. Wider range scans from these two samples are shown in Figure 4-3 for a detailed comparison.

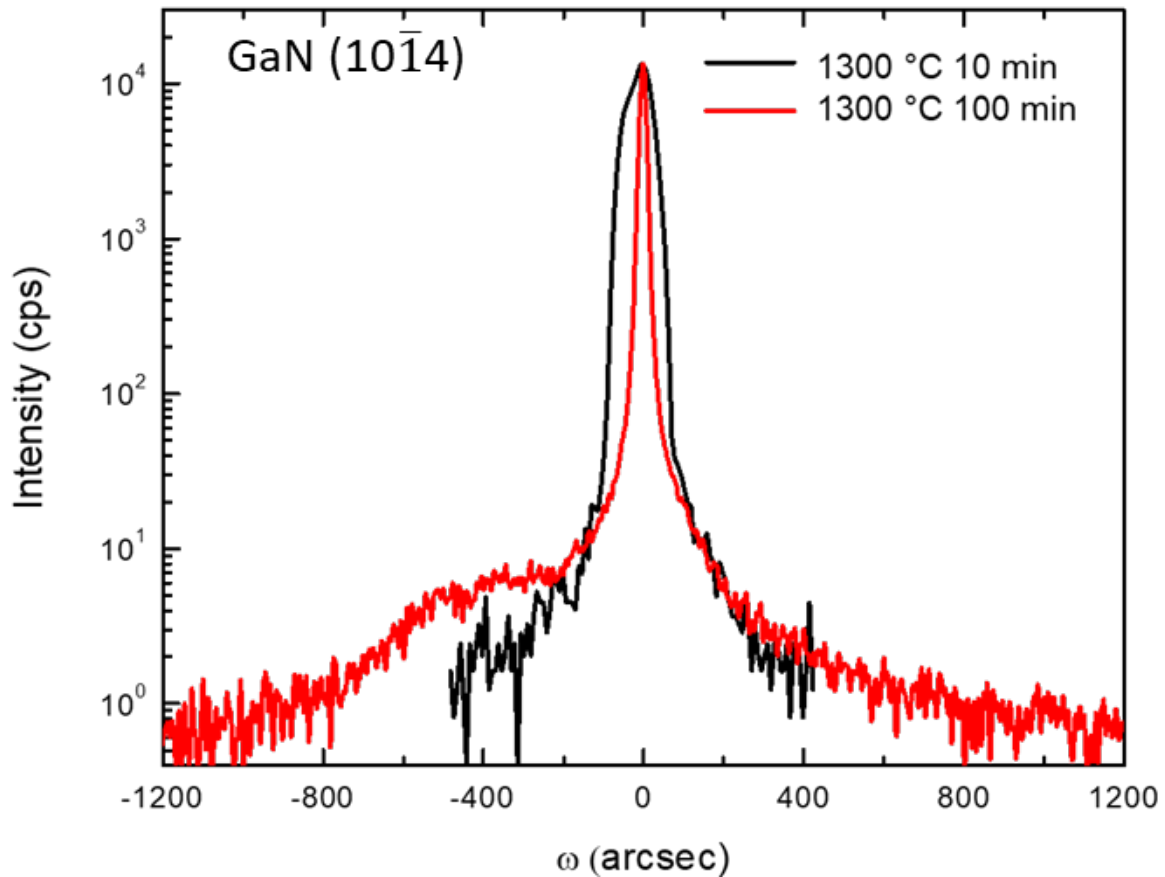


Figure 4-3 (10 $\bar{1}4$) triple-axis XRD rocking curves for samples annealed at 1300 °C for 10 min and 100 min.

For the 1300 °C, 100 min annealed sample, the main peak is narrower than the sample annealed for 10 min; however, a stronger diffuse scattering was found, particularly at ~400-800 arcsecs to the left of the peak. The differences are possibly due to continued evolution of the defect configurations such that there is a change in defect density and morphologies. To investigate this further, double crystal x-ray topography (XRT) – which is highly sensitive to lattice imperfections with an angular resolution on the order of arcsec was used ⁷³. Synchrotron double crystal XRT images at (11 $\bar{2}$ 4) reflection of the unimplanted sample, the as-implanted sample, and the 1300 °C 100 min sample are shown in Figure 4-4.

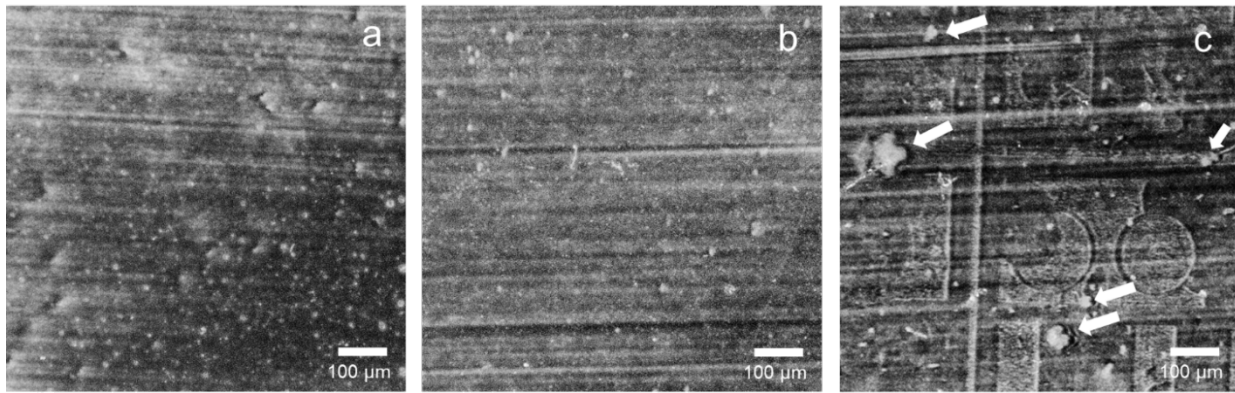


Figure 4-4 Synchrotron double crystal x-ray topography (11 $\bar{2}$ 4) images for (a) the unimplanted sample and (b) the as-implanted sample, both show a uniform contrast and the dot features corresponding to individual dislocations with a density of $\sim 10^6 \text{ cm}^{-2}$; (c) the 1300 °C annealed for 100 min sample, shows large non-diffracting regions (arrows); the thin orthogonal lines and circles are from the metalization pattern on the sample surface.

For a perfect crystal, the XRT would be uniformly grey across the whole image. However, individual dislocations induce local lattice distortions and result in small dot-like bright, non-diffracting features, as shown in Figure 4-4a and 4-4b. After annealing at 1300 °C for 100 min, the XRT image (Figure 4-4c) shows features that exhibit strong contrast and large (tens of microns)

non-diffracting regions were observed. Thus, these features are associated with extended defects formed after annealing. These extended defects cause a large amount of tilt/misorientation in the lattice such that Bragg condition was not satisfied over wide areas. Of course, the defects themselves may not be so large, but the distortions they create extend over length scales (tens of microns) far larger than the defects themselves. Similar concepts have been demonstrated in earlier studies on the misfit dislocations in Si using XRT^{55,56}. Note the presence of some orthogonal lines and circular features in Figure 4-4c, which are due to metallization on the sample surface.

Transmission Electron Microscope was employed to further investigate the nature of these extended defects. Two beam condition STEM bright field images with the diffraction vector \mathbf{g} equal to $\langle 11\bar{2}0 \rangle$ or $\langle 0002 \rangle$ are shown in Figure 4-5a and Figure 4-5b for the 1300 °C, 10 min sample. Extended defects were observed to a depth of ~ 200 nm (which corresponds to the straggle around the projected range) and consist of three different morphologies: lines, dots, and loops. Small line shape defects oriented parallel to the sample surface (highlighted with small arrows in Figure 4-5a) were identified to be basal plane stacking faults (BSFs). BSFs have a Burgers vector \mathbf{g} of $1/3 \langle 10\bar{1}0 \rangle$ and therefore is only visible under $\langle 11\bar{2}0 \rangle$ two beam condition. BSFs have been previously observed in implanted GaN as well as in other wurtzite III-V semiconductors^{74,75,76}. The formation of BSFs in GaN is equivalent to eliminating one basal plane, followed by a lattice translation along $1/3 \langle 10\bar{1}0 \rangle$. As a result, a strip of GaN with cubic stacking (ABCABC) is surrounded by the GaN with wurtzite stacking (ABAB)⁷⁷. High-resolution TEM image of the BSFs in 1300 °C, 10 min sample is shown in Figure 4-6 in which a cubic phase was observed within the hexagonal phase.

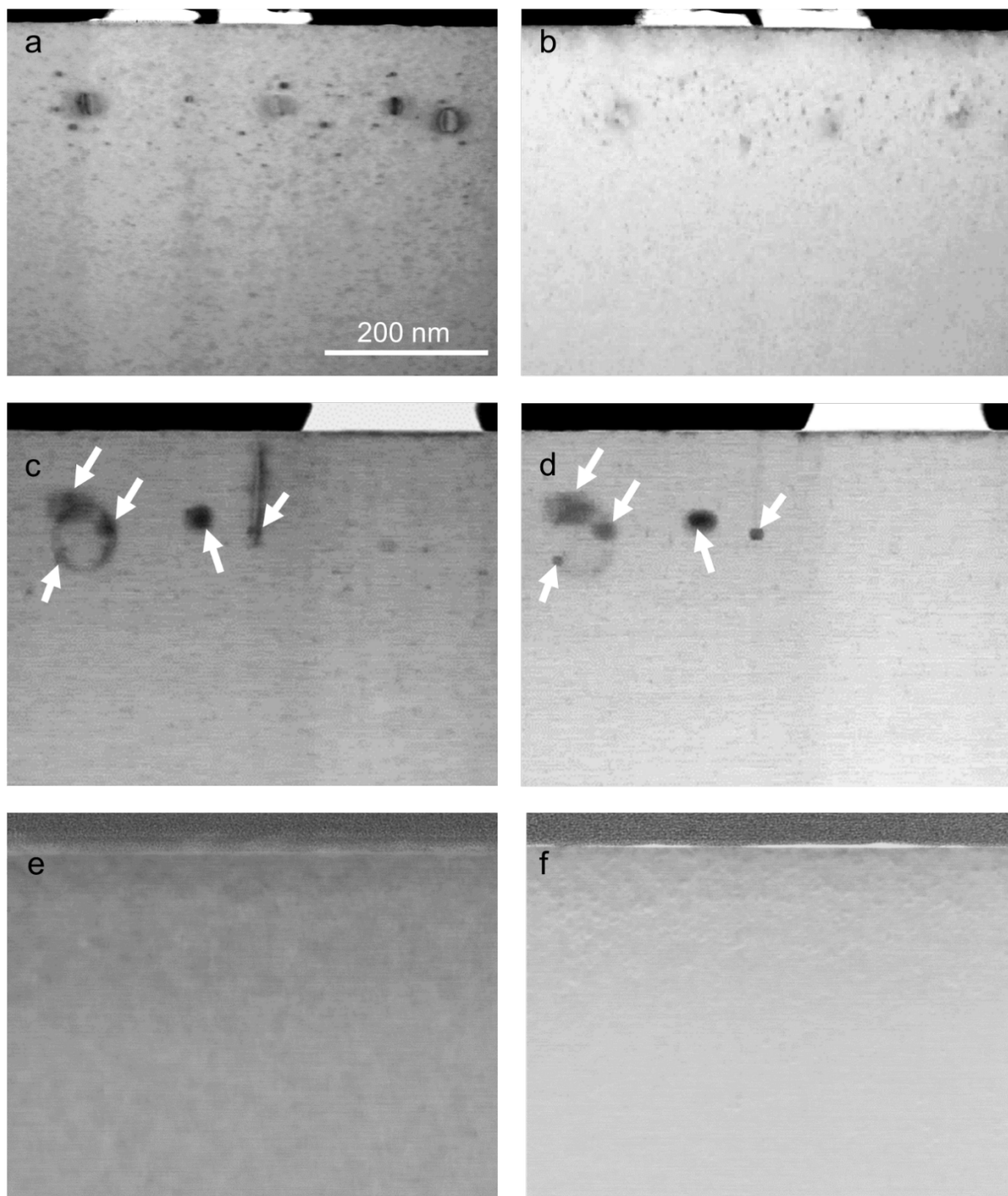


Figure 4-5 Cross-section STEM two beam condition bright field images with different diffraction vectors: (a) 1300 °C annealed 10 min sample, $\mathbf{g} = \langle 11\bar{2}0 \rangle$ with the arrows showing the basal plane stacking faults; (b) 1300 °C annealed 10 min sample, $\mathbf{g} = \langle 0002 \rangle$; (c) 1300 °C annealed 100 min

sample, $g = \langle 11\bar{2}0 \rangle$; (d) 1300 °C annealed 100 min sample, $g = \langle 0002 \rangle$; (e) as-implanted sample, $g = \langle 11\bar{2}0 \rangle$; (f) as-implanted sample, $g = \langle 0002 \rangle$. In (c) and (d), the arrows show beam damage.

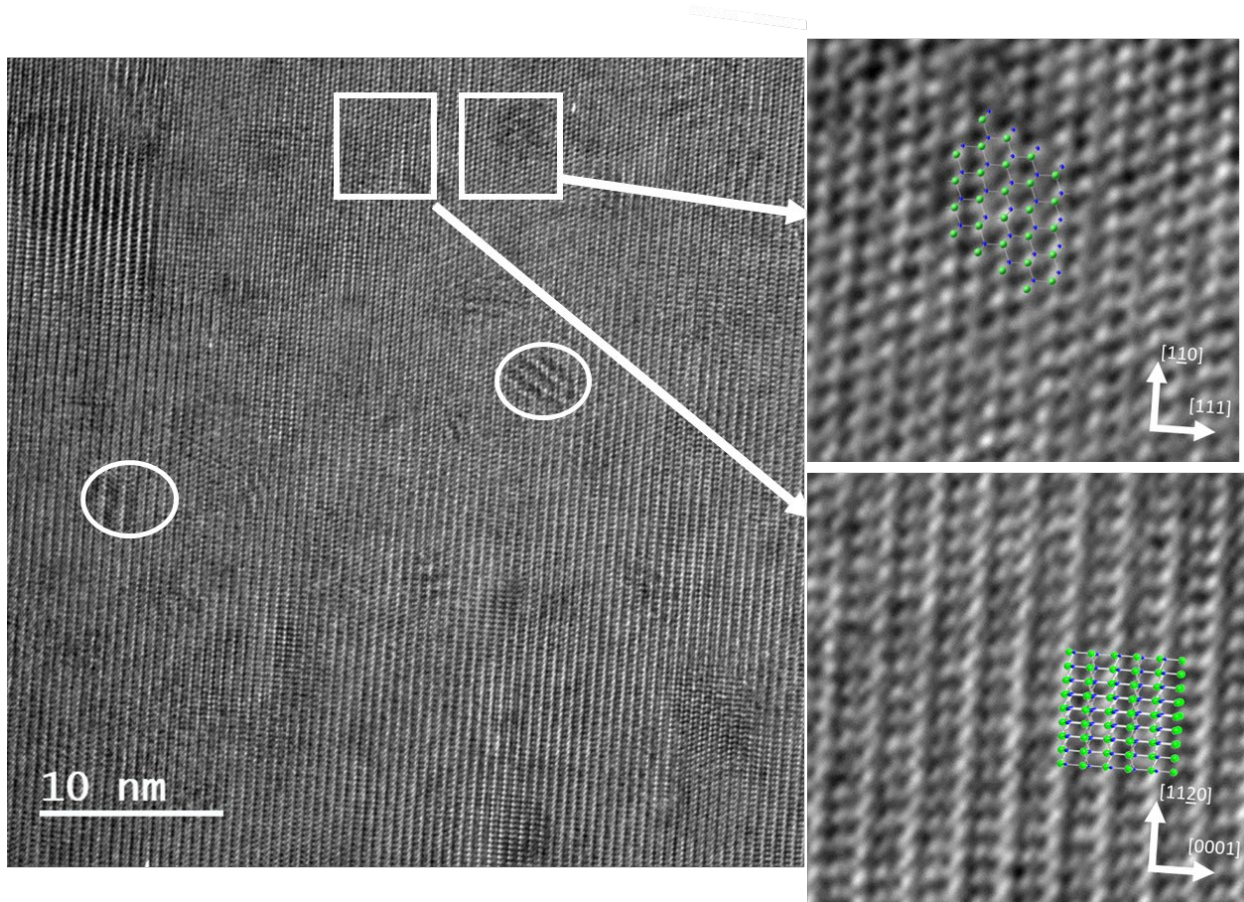


Figure 4-6 HRTEM image at the implanted region in 1300 °C 10 min sample. Magnification of the image shows the lattice fitted with ball and stick models and confirms a change in the stacking sequence in planes from ABAB (wurtzite) to ABCABC (zincblende). The two circles highlight regions with Moiré fringes.

Magnification of the images in these highlighted regions shows the lattice fitted with ball and stick models and confirms a change in the stacking sequence in planes from ABAB (wurtzite) to ABCABC (zincblende). The two phases are orientated such that the zinc blend [111] is parallel to the wurtzite [0001]. In fact, for SiC, the formation cubic phase inside hexagonal phase during the

post-implantation annealing had been investigated. Pezoldt *et al.* reported the formation of 3C-SiC clusters after annealing of 6H-SiC (implanted with Si) ⁷⁸. They concluded that lattice rearrangement such as the generation of partial dislocations and stacking faults can lead to formation of cubic phase SiC. This is consistent with my results suggesting that a similar process also exists in GaN. Apart from that, the high-resolution TEM image in Figure 4-6 also showed some Moiré fringes. They are formed by the superposition of two lattice planes that are similar in d-spacings but slightly misoriented ⁷⁹. In this sample, the fringes could be generated by other extended defects, such as dislocations, causing local distortions in the lattice. In addition, loop-shaped defects were also observed for the $\mathbf{g} = \langle 11\bar{2}0 \rangle$ diffraction conditions (Figure 4-5a), but not for the $\mathbf{g} = \langle 0002 \rangle$ condition (Figure 4-5b). These defects are identified to be dislocation loops on the prismatic planes. In the literature, prismatic loops are commonly found in hexagonal materials, for example, SiC ⁸⁰ and ZnO ^{81, 82}. The average diameter of the prismatic loops observed here is ~30 nm. For the small dots that have dark contrast in both Figure 4-5a and 4-5b, I consider these to be defect clusters as they were observed under both $\langle 0002 \rangle$ and $\langle 11\bar{2}0 \rangle$ diffraction conditions. For the 1300 °C, 100 min sample, the same set of STEM image conditions are shown in Figure 4-5c and 4-5d. Note that there are regions with uniform dark contrast (marked with arrows) which were caused by TEM beam damage. Interestingly, it was found that a reduction in the total number of extended defects compared to the case for annealing at 1300 °C; 10 min. The defect density was measured to be $3 \cdot 10^7 \text{ cm}^{-2}$ in the 1300 °C, 100 min sample, which is about an order of magnitude lower than the 1300 °C, 10 min sample ($4 \cdot 10^8 \text{ cm}^{-2}$). Also, the BSFs were absent, indicating that they were removed during the annealing from 10 min to 100 min. The prismatic loops are also fewer ($4 \cdot 10^6 \text{ cm}^{-2}$ for 100 min vs $1 \cdot 10^7 \text{ cm}^{-2}$ for 10 min), but the average diameter is larger (~60 nm). For comparison, the two beam condition STEM bright field images for the as-implanted

sample are shown in Figure 4-5e and 4-5f. No extended defect structures were observed. This is different from the two annealed samples where extended defects such as stacking faults or dislocation loops were observed under $g = \langle 11\bar{2}0 \rangle$ (5a, 5c). Therefore, the conclusion is that the extended defects were formed after annealing the implanted sample. The TEM results are in good agreement with the XRD rocking curve results, suggesting an evolution in the crystalline quality as the annealing time increases at 1300 °C, which would presumably extend up to 1400 °C and above. The decrease in FWHM/FW_{0.01M} is associated with the reduction in the overall extended defect density. However, the growth of the prismatic loops and the formation of new edge-type linear dislocations are likely related to the diffuse scattering observed in the (10 $\bar{1}$ 4) XRD rocking curve. Previous studies using heteroepitaxial GaN on sapphire structure showed there is a correlation between the remnant defect content and the device performance. A high remnant defect density would lead to reduced carrier mobility^[9, 14]. However, it had not been resolved in that case if the defects that contributed to the reduced mobility were implant-induced or related to the high initial mismatch between GaN and sapphire. Using high-quality homoepitaxial GaN eliminates the influence of mismatch, thus any remnant defects are dominated by the implantation/annealing process. The recent study on electrical properties which employed a similar annealing technique (1GPa N₂, 1380 °C, 5 mins) achieved p-type acceptor formation with over 50% activation at 500K using Mg implanted homoepitaxial GaN structures⁴³ (but only ~1.6% acceptor activation at room temperature) due to the deep acceptor level which is similar to previous reports^{38, 65}. The room temperature mobility reported is comparable to that of MOVPE p-GaN. Unfortunately, there was no structural analysis in that study. This work complements those electrical measurements by showing the defect evolution after the high-pressure annealing step and is expected to improve the performance of GaN-based vertical power devices.

4.4 Summary

Mg implanted homoepitaxial GaN grown on high-quality GaN substrates was annealed and characterized. The implantation process introduced an elastic strain along the [0001] direction. The strain recovery process was quantified and modeled as a function of annealing temperature and time. Complete strain recovery was observed after annealing at 1300 °C for 10 min. X-ray topography and (10 $\bar{1}$ 4) triple-axis rocking curve scans showed the lattice distortion/tilt caused by the formation of extended defects. STEM images revealed the nature of the extended defects after annealing at 1300 °C were basal plane stacking faults, prismatic loops, defect clusters and edge-type linear dislocations. A reduction of the extended defect density between 1300 °C for 10 min and 1300 °C for 100 min was observed and correlated with the decrease in triple-axis XRD rocking curve FW0.01M. The results suggested a significant amount of defect reconfiguration/rearrangement occurs at 1300 °C and likely at higher temperatures as well. Further reduction in the extended defect density by optimizing annealing temperature and annealing time is expected to have a significant impact on improving the performance of GaN-based vertical power devices.

Chapter 5 Defects Evolution and Mg Segregation in Mg-implanted GaN with Ultra-High-Pressure Annealing

5.1 Motivation

The previous chapter shows promising results of the evolution of defect structures observed after annealing at 1300 °C for a longer time in a Mg single implant sample. However, for real applications, the doping profile needs to be a box profile. Meanwhile, by applying an ultra-high N₂ pressure of one GPa, the annealing temperature can be further increased beyond 1300 °C to 1500 °C, which is close to the targeted annealing temperature (2/3 of the melting point of GaN) to activate the Mg acceptors. This chapter will focus on Mg implantation into GaN with a multi-step box profile and annealing at temperatures up to 1500 °C. It leverages the defect characterization method with X-ray scattering and electron microscopy techniques that were developed (through the studies shown in the previous two chapters) to assess (i) the key residual defects after annealing that have a significant impact on the dopant activation efficiency and (ii) how to remove them. These results in this chapter are anticipated to guide the key processing steps and requirements to achieve high activation efficiency p-type doping for vertical GaN devices.

5.2 Experimental Details

GaN epitaxy films with a thickness of 2.5 μm were grown via metal-organic chemical vapor deposition (MOCVD) on high-quality ammonothermal GaN substrates^{83, 44}. The magnesium ions with a box profile were implanted at room temperature using six different accelerating voltages (350 keV, 200 keV, 150 keV, 100 keV, 60 keV, and 25 keV) at a total dose level of 1×10^{15} cm⁻². Using the SRIM simulation software⁶⁰, the maximum concentration was

calculated to be $1.8 \times 10^{19} \text{ cm}^{-3}$ from the surface to a depth of $\sim 500 \text{ nm}$. Post-implantation annealing was performed on the implanted wafers at temperatures of $1300 \text{ }^\circ\text{C}$, $1400 \text{ }^\circ\text{C}$, and $1500 \text{ }^\circ\text{C}$ for a duration of either 10 minutes or 100 minutes and so will be referred to as, for example, the 1300°C ; 10 min., sample. An ultra-high N_2 pressure of one GPa was applied during the annealing sequence to prevent GaN from decomposition without using a cap^{44, 83}.

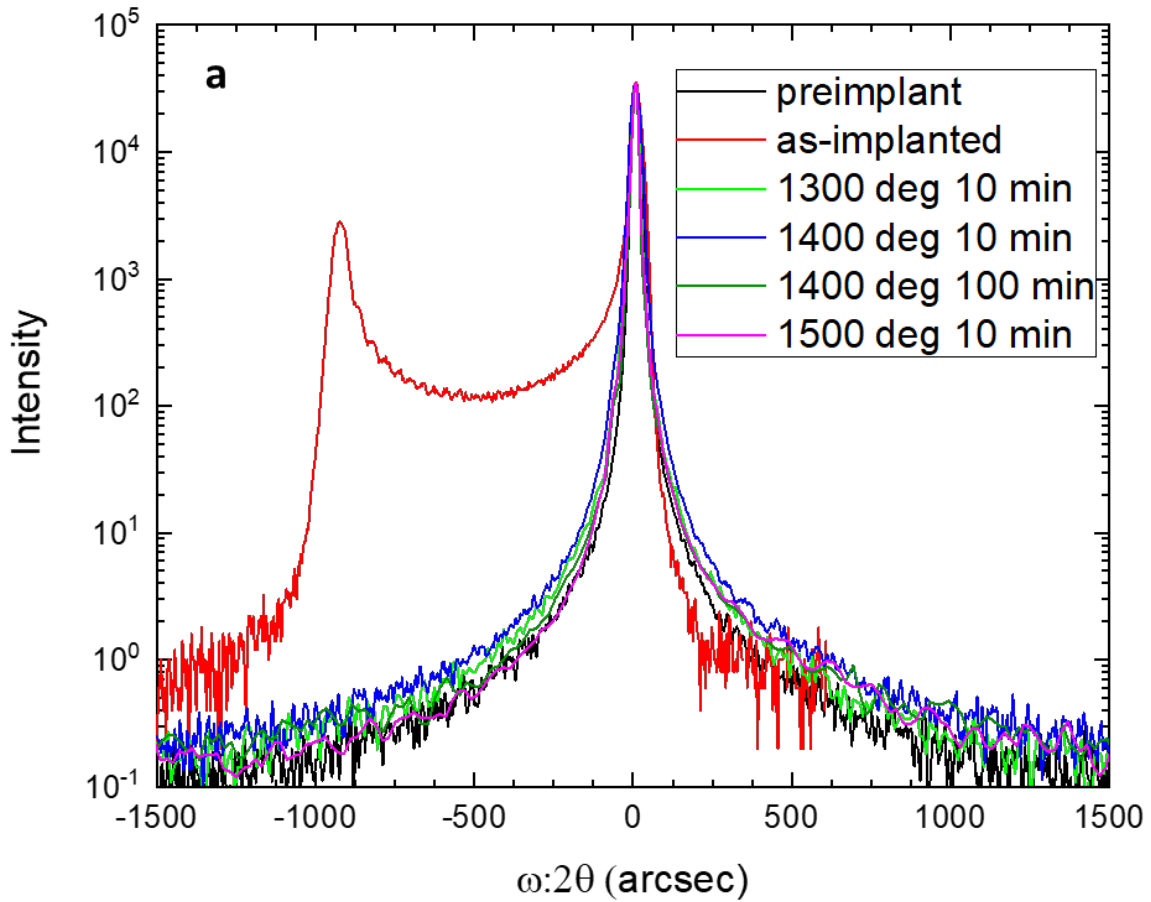
Structural characterization was performed by a combination of X-ray scattering and electron scattering techniques. The lattice distortions and crystalline quality were assessed by Triple-axis X-ray diffraction (TAXRD) and X-ray topography (XRT). TAXRD measurements were performed using a Jordan Valley (Bruker) D1 diffractometer, with an incident beam mirror to produce a parallel beam, followed by a Si (220) channel cut collimator ($\text{Cu K}\alpha_1$ radiation). The scattered beam optics included a Si (220) channel cut crystal^{65, 83, 84}. Synchrotron double crystal X-ray topography measurements were performed at the 1-BM Beamline of the Advanced Photon Source, Argonne National Laboratory with a photon energy of 8.05 keV . The first crystal was a highly asymmetric Si (333) beam expander and the sample was oriented for diffraction of the $(11\bar{2}4)$ reflection in the glancing incidence geometry^{85, 86}. Topography images were taken by exposing at different positions on the rocking curve and recorded separately on different films (hereinafter referred to as single exposure images). Information of the specific post-annealing defects was obtained using Transmission Electron Microscope (TEM). TEM samples roughly 100 nm thick were made using an FEI Nova 600 Dual Beam Focused Ion Beam (FIB) and further thinned by a gentle Ar^+ ion beam with 0.3 kV incident energy to remove any FIB induced damage layer. Scanning Transmission Electron Microscope (STEM) images using bright field (BF) or high-angle annular dark field (HAADF) detectors, and High-Resolution TEM images were taken

using the FEI Talos and Argonne Chromatic and Aberration-Corrected (ACAT) TEM respectively at the Center for Nanoscale Materials, Argonne National Laboratory ⁸⁷.

5.3 Results and discussions

The triple-axis X-ray ω :2 θ line scans near GaN (0004) peak of all the samples are shown in Figure 5-1a. The presence of the intensity with fringes to the left of the main peak in the as-implanted sample is due to lattice distortion as a result of the implant-induced point defect formation ^{67, 84, 88}. After annealing, in all cases, the implantation-induced strain is completely relieved. Previously, it was shown that annealing under a similar condition at 1300 °C for 10 min removed the implantation-induced strain for a single implant (Mg: 100 keV) at a dose level of $2 \times 10^{14} \text{ cm}^{-2}$ ⁸³. In this work, the dose level is five times of that of previous work, and the same annealing condition is still sufficient to relieve the strain. Meanwhile, annealing at higher temperatures and longer time does not have any further impact on the strain state. Thus in all cases, the point defects, which were responsible for the strain have reformed into more stable configurations that can include extended defects. The residual defect structures after annealing were first screened using X-ray topography. Figure 5-1 b-e show the single exposure curves X-ray topography images, taken at the peak of the (11 $\bar{2}$ 4) rocking curves, from the as-implanted sample and samples annealed at 1300 °C, 1400 °C, and 1500 °C. In all cases, dot-shape defects are observed, which correspond to individual threading dislocations. The dislocation density is on the order of 10^4 cm^{-2} , which is consistent with the dislocation density level in ammonothermal GaN reported in the current literature ⁸⁹. The as-implanted and the 1500 °C annealed samples show similar characteristics: only individual threading dislocations with no extended defects are present. The 1400 °C sample consists of isolated loop-shaped defects that do not diffract at the same angle

as the rest of the material. Separate images capture the loops diffracting at an angular difference of ~ 8 arcsec away from the bulk of the GaN, quantifying the small but measurable local lattice distortion at the loop defects.



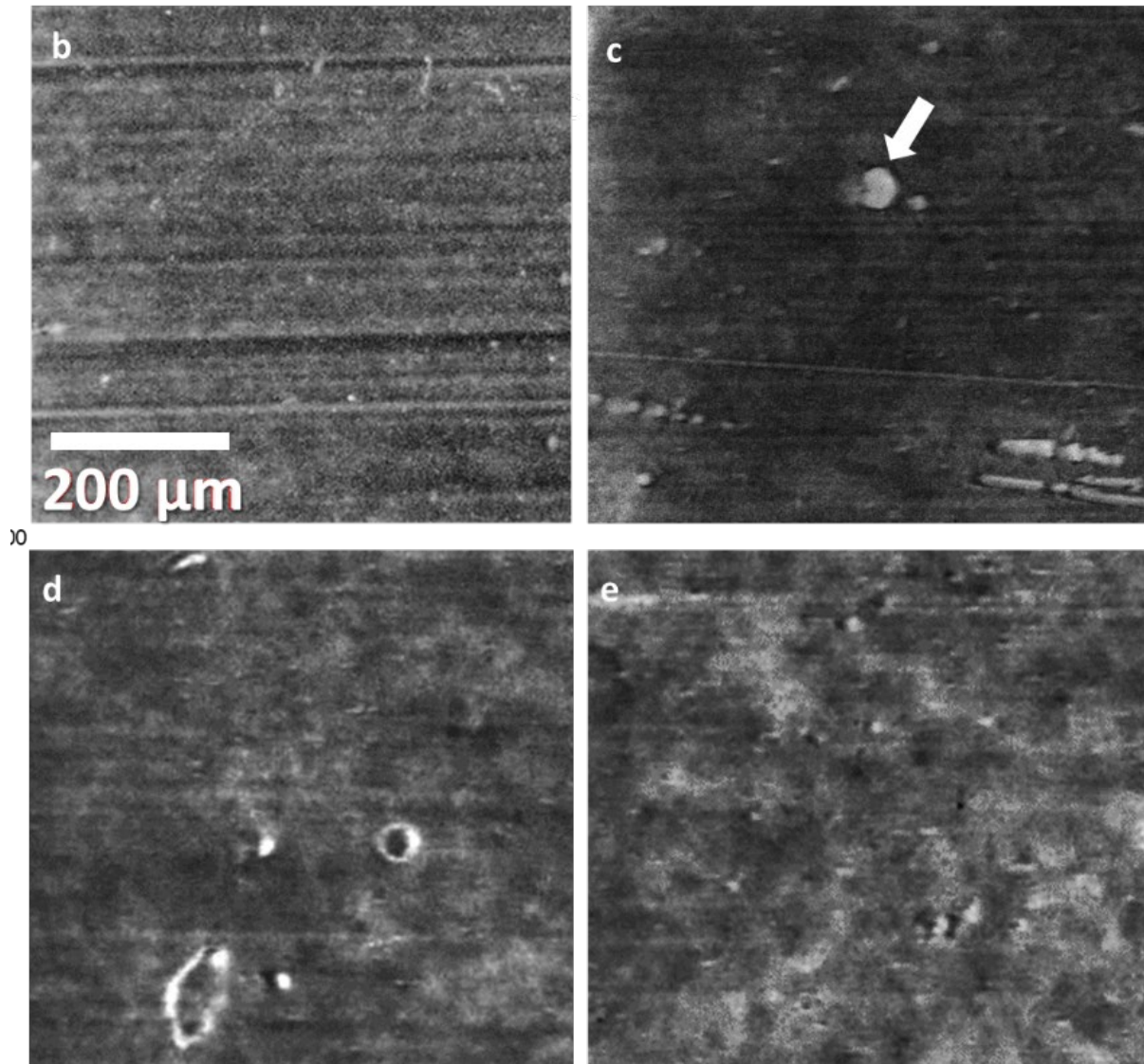


Figure 5-1 (a) Triple axis X-ray $\omega:2\theta$ line scans near GaN (0004) peak for the samples showing the implant induced strain was fully relieved after annealing at 1300 °C for 10 minutes and annealing at temperatures ≥ 1400 °C has no further impact on the strain state; X-ray topography images exposed at a single point along a rocking curve for: (b) as-implanted; (c) annealed at 1300 °C for 10 minutes; (d) annealed at 1400 °C for 100 minutes, and (e) annealed at 1500 °C for 10 minutes. The white dots that appeared in all 4 images (b-e) are individual dislocations, and the densities are on the order of 10^4 cm⁻².

The amount of the local lattice distortion here is comparable to an earlier work from our group, using laboratory XRT equipment, to determine the localized tilt (a few arcsecs) around micropipe defects in SiC substrates⁵⁷. The 1300 °C sample, on the other hand, exhibits large non-diffracting features that are not observed in the other samples; (arrow in figure 5-1c). Details of the extended defects were further characterized using TEM/STEM images. Figure 5-2 shows the STEM two-beam condition bright field images taken under different diffraction conditions. Figure 5-2 a-d are taken under $\mathbf{g} = \langle 0002 \rangle$ to show, for example, defects with a screw component and figure 5-2 e-h are taken under $\mathbf{g} = \langle 11\bar{2}0 \rangle$ to show defects with an edge component. The four samples can be divided into two groups based on the extended defects observed. The samples annealed at 1400 °C and 1500 °C showed very similar defect structures. The prominent residual defects after annealing at and above 1400 °C are dislocation loops. These dislocation loops are prismatic loops, dominated by edge characteristics, and therefore show strong contrast only under $\mathbf{g} = \langle 11\bar{2}0 \rangle$ (figure 5-2 f-h). Similar prismatic loops have been observed earlier in chapter 4 from the study focusing on Mg implanted GaN (single implantation at 100 keV) after UPHA at 1300 °C⁸³. Most of the loops are not completely visible. Because those loops lie on crystallographic planes that are not perfectly parallel to the sample orientation, i.e. $\{10\bar{1}0\}$, only a portion of the loop is oriented to show contrast, an example is given with a blue arrow in figure 5-2f. In the extreme case, when the loop is oriented perpendicular to the sample orientation, for example $\{11\bar{2}0\}$, it will show up as a bright line surrounded by sharp contrast on both sides, an example is given with a red arrow in figure 5-2f. The contrast is caused by lattice distortion near the dislocation loop.

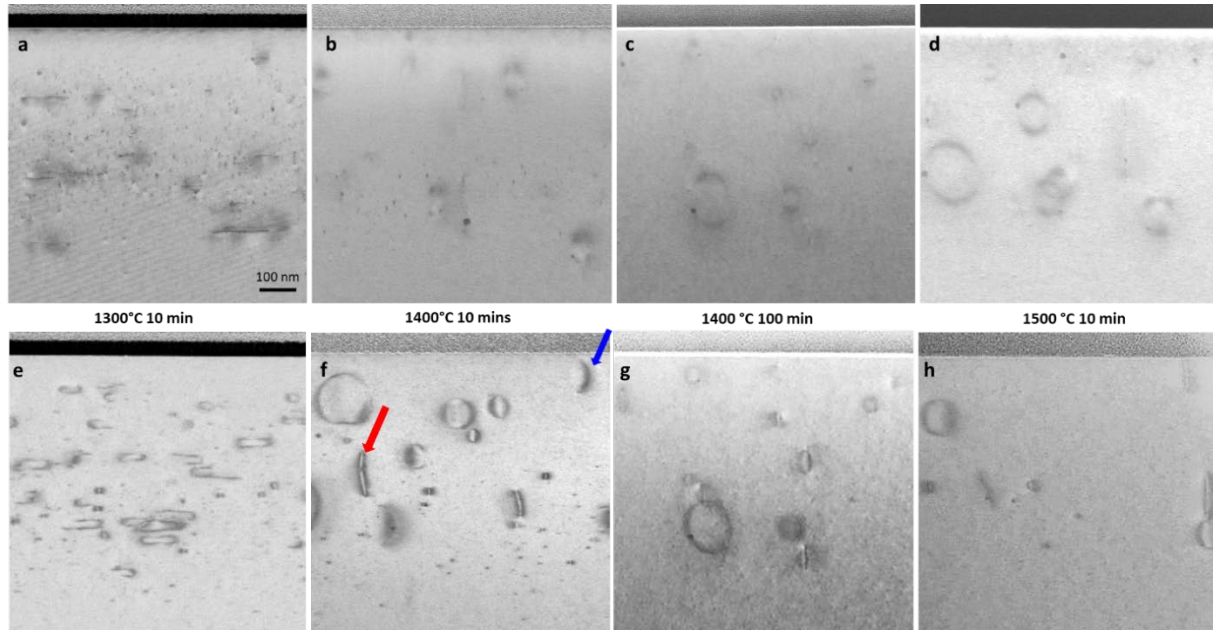


Figure 5-2 Cross-section STEM two beam condition bright field images with diffraction vector $\mathbf{g} = \langle 0002 \rangle$, (a) 1300 °C annealed 10 min sample; (b) 1400 °C annealed 10 min sample; (c) 1400 °C annealed 100 min sample; (d) 1500 °C annealed 10 min sample; and diffraction vector $\mathbf{g} = \langle 11\bar{2}0 \rangle$; (e) 1300 °C annealed 10 min sample; (f) 1400 °C annealed 10 min sample; (g) 1400 °C annealed 100 min sample; (h) 1500 °C annealed 10 min sample. In (f), the arrows show examples of dislocation loops that are not parallel to the FIB cut. All images share the same scale bar shown in (a).

The 1300 °C 10 min sample exhibits an additional, different defect structure than the others. Triangular and trapezoidal shape defects were observed under $\mathbf{g} = \langle 0002 \rangle$, these defects did not exist in the three samples annealed at higher temperatures. A magnified STEM bright field image taken under $\mathbf{g} = \langle 0002 \rangle$ for the 1300 °C 10 min sample is shown in figure 5-3a. Examples of the triangular and trapezoidal shape defects are circled in red and highlighted in the blue box. The triangular defects showed structural characteristics similar to those of pyramidal inversion domains (PIDs). The base of the PIDs is along the $\{0001\}$ plane and the sidewalls (highlighted with dotted

lines) are along the $\{11\bar{2}3\}$ planes, inclined at $\sim 47^\circ$, as shown by high-resolution TEM image in figure 5-3b. The lattice is distorted inside the PID when compared to the surrounding GaN matrix. An additional atomic layer (highlighted with a green box) was observed near the base of the pyramid (basal plane of GaN), causing lattice bending of the following ten layers. For an individual PID (the STEM HAADF image is shown in figure 5-3c), the Energy Dispersive X-Ray Analysis (EDX) map in figure 5-3d shows the Mg signal at the PID. A line profile is generated by integrating the intensity in the yellow box in figure 5-3d and shown in figure 5-3e. From the EDX map and the line profile, an increased Mg signal is observed at the base of the PID, where the extra layer of atoms is located, with a decrease in the Ga signal at the same position. This indicates that there is possibly a compound formation including the Mg and N in the PIDs.

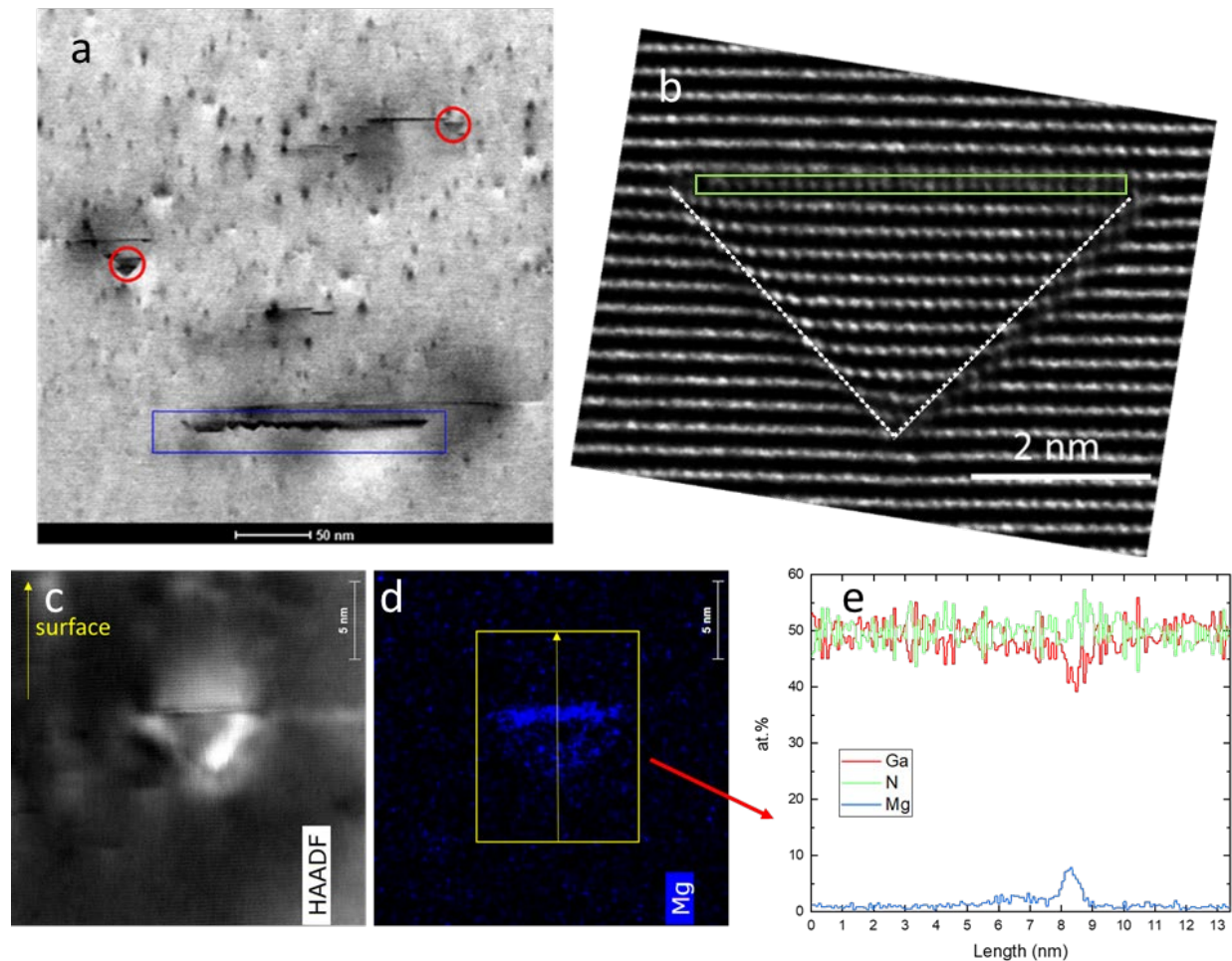


Figure 5-3 (a) STEM image of the 1300 °C 10 min sample showing examples of pyramidal inversion domain (circled in red) and trapezoidal inversion domain (boxed in blue); (b) HRTEM image of a pyramidal inversion domain showing the $\{11\bar{2}3\}$ facets (highlighted with dotted white lines) and the extra layer of atoms near the base (boxed in green); (c) HAADF image of a pyramidal inversion domain; (d) EDX map showing the Mg segregation in the pyramidal inversion domain shown in c. (e) EDX line profile generated by integrating the intensity in the yellow box in Fig. 3d (the arrow shows the direction of the line profile, i.e. the start is at the bottom).

For the trapezoidal shape defects, facets along the $\{11\bar{2}3\}$ planes on the edge were also observed, as shown in figure 5-4a (highlighted with orange lines). The EDX map and line profile from the

trapezoidal shape defects also show increased Mg signal and reduced Ga signal along the basal plane, shown in Figures 5-4b and 5-4c, which is similar to what was observed in the PIDs. Therefore, these trapezoidal shape defects were considered as trapezoidal inversion domains (TIDs). In fact, the center part of the largest TID consists of a series of small aligned pyramids, as shown in figure 5-3a. It is speculated that the TIDs are the initial stages of development and will eventually evolve into the PIDs. Thus, it appears that both the PIDs and TIDs defects contain electrically inactive Mg atoms and could be a cause of the reduction in Mg activation efficiency. In the current literature, PIDs with signs of Mg segregation have been observed in both highly Mg-doped epitaxial layers with Mg concentration above the 10^{19} cm^{-3} level^{90 91 92} as well as in Mg implanted GaN after annealing at 1350 °C⁹³. In MOVPE epitaxial Mg-doped p-GaN, Vennegues et al. hypothesized that introducing a higher level of Mg in GaN results in the formation of Mg_3N_2 where inactive Mg atoms do not substitute Ga sites but are accommodated into other sites⁹¹.

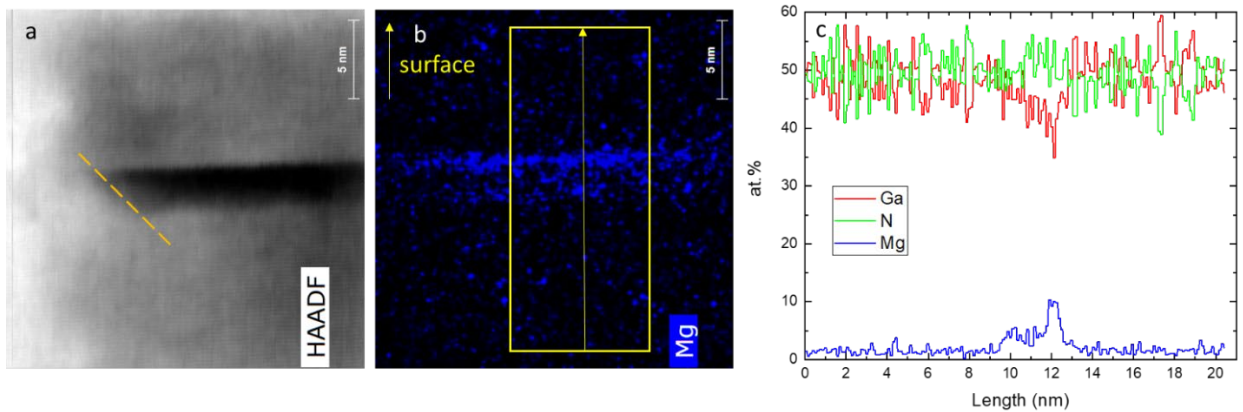


Figure 5-4 (a) HAADF image of a trapezoidal inversion domain with the edge also showing $\{11\bar{2}3\}$ facets (highlighted with a diagonal orange line); (b) EDX map showing the Mg segregation in the trapezoidal inversion domain shown in a. (c) EDX line profile generated by integrating the

intensity in the yellow box in Fig. 4b (the arrow shows the direction of the line profile, i.e. the start is at the bottom).

Another study from Remmele et al. further characterized the PIDs produced during epitaxy with TEM and modeled the domain boundary along the base to follow GaNMgNGa layers in an abcab stacking ⁹⁴. The ACAT TEM results are in good agreement with this model and show that a similar interaction between Mg and N occurred in Mg implanted GaN after annealing at 1300 °C. The base of PIDs contains a row of Mg atoms and thus prevents the Mg from becoming electrically active. However, in those epitaxially grown structures, it is difficult to remove the PIDs once they are formed. To suppress the formation of the PIDs, a low-temperature growth method is needed, such as metal-modulated epitaxy ⁹⁵. Unlike the case for annealing the ion implantation damage, the MOCVD growth temperature (~1150 °C) of highly Mg-doped epitaxial GaN is well below the temperature needed to deter inversion domain formation. In the case of Mg implanted GaN, the current literature has not shown how to remove or avoid the PIDs. However, the PIDs and TIDs are not observed in any of the samples annealed at and above 1400 °C in this work. This suggests that the PIDs and TIDs either do not form or are dissolved at high temperatures (≥ 1400 °C) and are formed only at temperatures ~ 1300 °C after implantation as presented here and also described in works by Kumar et al., ⁹⁶ for implantation (and in works by Vennegues et al., ^{90,91} for epitaxial structures in which high concentrations of Mg are present after epitaxial growth at ~1150 °C). This provides insight for improving dopant activation efficiency by annealing Mg-implanted GaN at temperatures above 1400 °C. Recently, Breckenridge et al ⁴⁴., reported the electrical data from a sister set of the samples annealed up to 1400 °C under similar conditions, shown in figure 5-5.

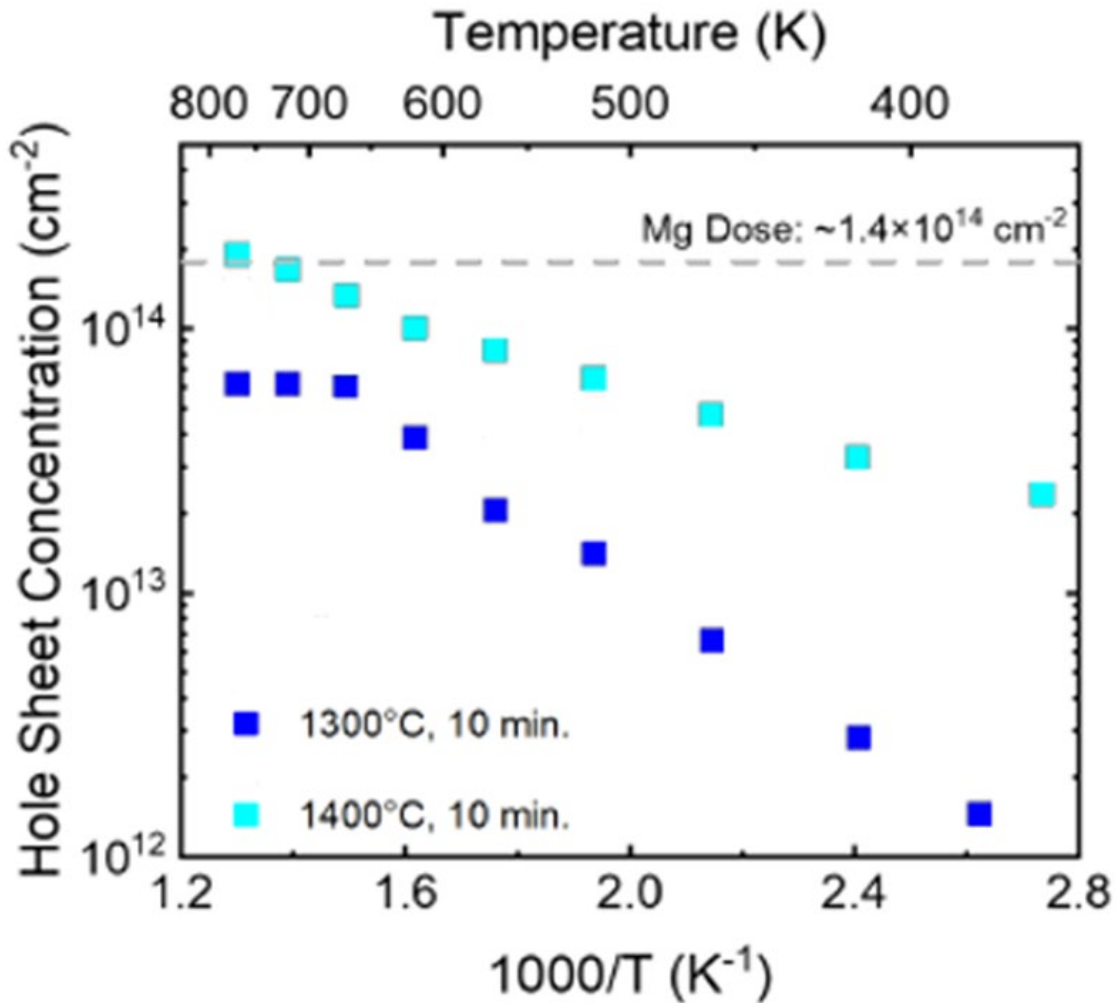


Figure 5-5 Carrier concentration measured using hall measurements for Mg implanted GaN with UHPA at temperatures of 1300 °C and 1400 °C for 10 minutes ⁴⁴.

The results showed that annealing at 1400 °C leads to higher dopant activation (~10% at room temperature, ~100% at 500 °C, because the Mg level is not that shallow – at $\sim E_v + 0.2$ eV), compared to annealing at 1300 °C (<1% at room temperature, ~40% at 500 °C). Based on the model from Remmele et al., the amount of Mg bound in the PIDs and TIDs is estimated to be 1.6×10^{18} cm⁻³, which is ~10% of the total Mg content ⁹⁴. This represents the lower bound of the Mg in PIDs and TIDs because the EDX clearly shows higher Mg concentrations within the entire

defects (for example figure 5-3d and 5-4b). The results here complement the earlier study from Breckenridge et al.,⁴⁴ by providing the structural analysis of the residual defects and showing the Mg segregation in PIDs and TIDs is a key mechanism for the reduction of dopant activation efficiency and can be avoided if the annealing temperature is ≥ 1400 °C.

As shown before, the prominent residual defects after annealing at and above 1400 °C are prismatic dislocation loops. High-resolution TEM image from one of the small loops in the 1400 °C 10 min sample is shown in figure 5-6a. Fast Fourier transform (FFT) patterns were obtained from three regions on the HRTEM image, outside of the loop (blue), near the center of the loop (orange), and on the edge of the loop (red), as shown in figure 5-6 b-d. FFT taken at regions outside of the loop (blue) and on the edge of the loop (red) show a pure hexagonal GaN pattern, highlighted with red circles. FFT near the center of the loop shows additional patterns, highlighted with yellow circles that correspond to cubic GaN, where $[110]_{\text{cubic}}$ is parallel to $[11\bar{2}0]_{\text{hexagonal}}$. Iwata et al., have reported similar dislocation loops in Mg implanted GaN and showed these loops are vacancy type dislocation loops⁹⁷. The study in chapter 4 showed that during post-implantation annealing, the removal of implant-induced strain is accompanied by lattice rearrangement such as the generation of stacking faults, which can lead to the formation of cubic phase⁸³. It is speculated that a similar process occurs during the formation of these dislocation loops. Lattice rearrangement disrupts the original hexagonal stacking and results in parts of the lattice exhibiting cubic stacking. On the other hand, there is an overall decreasing trend in the defect density after annealing at a higher temperature or for a longer time. The loop defect density was measured to be $3.8 \times 10^9 \text{ cm}^{-2}$ for 1400 °C 10 min case, $1.5 \times 10^9 \text{ cm}^{-2}$ for the 1400 °C 100 min case, and $1.1 \times 10^9 \text{ cm}^{-2}$ for 1500 °C 10 min case. Therefore, annealing at high temperature (\geq

1400 °C) showed no sign of Mg segregation and a decreasing trend in defect density, both of which are expected to improve device performance.

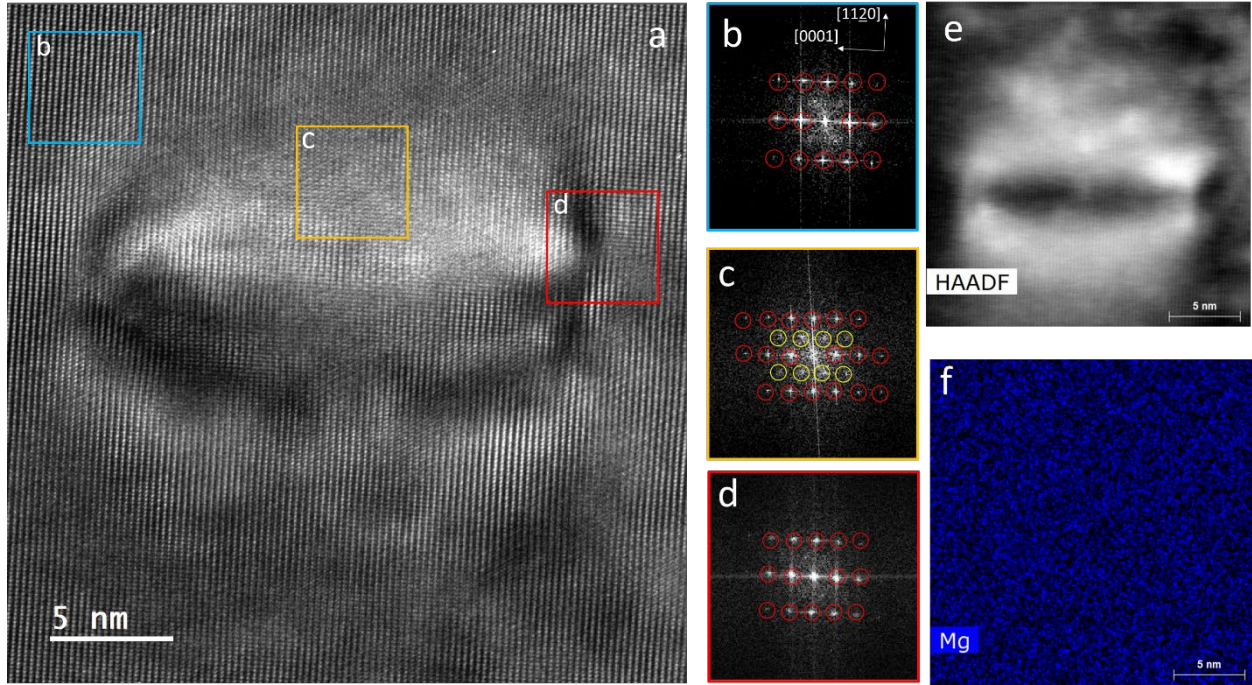


Figure 5-6 (a) HRTEM image of a small dislocation loop, fast Fourier transform pattern from three regions (three boxes) are shown in b-d; b) FFT outside of the loop showed pure hexagonal pattern (red circles); c) FFT close to the center of the loop show hexagonal GaN plus additional cubic GaN pattern (yellow circles); d) FFT on the edge of the loop also show a pure hexagonal pattern; (e) HAADF image of a small dislocation loop and the (f) the EDX map showing no signs of the Mg segregation in the loop.

5.4 Summary

The defect characteristics in magnesium implanted homoepitaxial GaN with ultra-high N₂ pressure annealing were investigated. Annealing of Mg implanted GaN with one GPa N₂ pressure

at 1300 °C for 10 minutes completely removed the implant-induced strain. Extended defects remain after annealing with both pyramidal and trapezoidal inversion domains, as well as prismatic dislocation loops. The inversion domains show clear Mg segregation and produce electrically inactive Mg that limits the dopant activation efficiency. Increasing the annealing temperature ≥ 1400 °C under the same condition results in a decrease in residual loop defect density with no sign of Mg segregation at these defects. Pyramidal and trapezoidal inversion domains also do not exist with annealing temperatures ≥ 1400 °C. This study provides the structural analysis of the residual defects, showing Mg segregation in PIDs and TIDs is one of the mechanisms for inactive Mg and can be avoided if the post-implant annealing temperature is ≥ 1400 °C. This work complements an earlier study with dopant activation efficiency data showing that annealing at 1400 °C leads to higher dopant activation compared to annealing at 1300 °C. Results from this work are expected to help achieve higher activation efficiency of p-type doping for devices including vertical GaN device structures.

Chapter 6 Conclusion and Future Work

6.1 Conclusions

This work provided a fundamental understanding of the implant-induced defects in Mg implanted GaN and their impacts on the electrical performance. It started by developing a methodology to study the structural defects associated with Mg implanted heteroepitaxial GaN on sapphire substrates with MRTA annealing. The implant-induced strain was quantified, and the direction of the strain was determined using x-ray diffraction techniques. The post-annealing defect characteristic was analyzed using TEM and it was found that improvements in mobility correlate with defect reduction in the implanted layer. However, the high intrinsic defect density ($> 10^8 \text{ cm}^{-2}$) that existed in the heteroepitaxial GaN makes it difficult to separate implant-induced defects from the pre-existing intrinsic defects. The rocking curve widths are still broad even after the MRTA annealing.

Homoepitaxial GaN on high-quality ammonothermal substrate possesses low intrinsic defect density ($\sim 10^4 \text{ cm}^{-2}$) and was ideal for studying the strain relaxation and defect evolution in Mg implanted GaN (single energy implant 100 keV) with UHPA annealing at temperatures from 700 °C to 1300 °C. High initial point defect ‘relaxation’ was observed at all temperatures. A substantial amount of strain relaxation occurs within 10 minutes. An additional 90 minutes of subsequent anneal results only in small addition displacement reconfiguration. A complete strain removal (displacement reconfiguration) was achieved by annealing at 1300 °C for 10 min using UHPA. A significant amount of lattice rearrangement was observed after annealing at 1300 °C for a longer time (10 min vs 100 min) evidenced by the reduction in both the rocking curve width as well as the extended defect density after annealing at 1300 °C for a longer time.

Building upon all the valuable information obtained, this work proceeds to understand defect evolution at temperature ≥ 1300 °C and their impacts on the electrical performance in Mg implanted GaN with a box profile (more practical in real applications). Annealing Mg-implanted homoepitaxial GaN at temperatures at or above 1400 °C eliminates the formation of inversion domains and leads to improved dopant activation efficiency. Extended defects in the form of inversion domains contain electrically inactive Mg after post-implantation annealing at temperatures as high as 1300 °C (UHPA), which results in a low dopant activation efficiency (<1% at room temperature, ~40% at 500 °C). However, annealing at temperatures of 1400 °C to 1500 °C (also one GPa N₂ overpressure) eliminates the presence of the inversion domains. While residual defects, such as dislocation loops, still exist after annealing at and above 1400 °C, chemical analysis at the dislocation loops shows no sign of Mg segregation. Meanwhile, an overall decreasing trend in the dislocation loop size and density is observed after annealing at higher temperatures and longer times. Electrical measurements show improved activation efficiency after annealing at 1400 °C (~10% at RT, ~100% at 500 °C). The results provide the structural analysis of the residual defects and show that Mg segregation in the inversion domain is a key mechanism for the reduction of dopant activation efficiency and can be avoided if the annealing temperature is ≥ 1400 °C. Results from this work are expected to help achieve higher activation efficiency of p-type doping for devices including vertical GaN device structures.

6.2 Future Work

The UHPA method is a conventional annealing method with a low ramp rate (40 °C/ min). The time it takes to reach elevated temperature (>1300 °C) is usually long and a significant amount of Mg diffusion would happen during ramp up as well as the dwell time. Sakurai et al. have shown

that a significant Mg diffusion occurs after UHPA (one GPa N₂) annealing at 1400 °C and above for only 5 mins⁴³. The post-annealing Mg extends over 500 nm deeper than the designed depth. As shown in figure 6-1 on the left, the SIMS data show the Mg peak concentration also dropped from $1 \times 10^{19} \text{ cm}^{-3}$ to $\sim 2 \times 10^{18} \text{ cm}^{-3}$. Future work to suppress the Mg diffusion effect during dopant activation annealing is needed to better control the doping profile. One potential approach is using MRTA instead of UHPA. Earlier results show that the SIMS Mg profiles before and after MRTA annealing at a peak temperature <1400 °C for a total time of 5 mins are identical (Figure 6-1 on the right)⁶⁴. Process development of using MRTA annealing at a peak temperature >1400 °C for a total time of a few minutes is expected to achieve good dopant activation with less Mg diffusion involved but requires a series of optimization in annealing pressure, cycle time, and AlN cap structures.

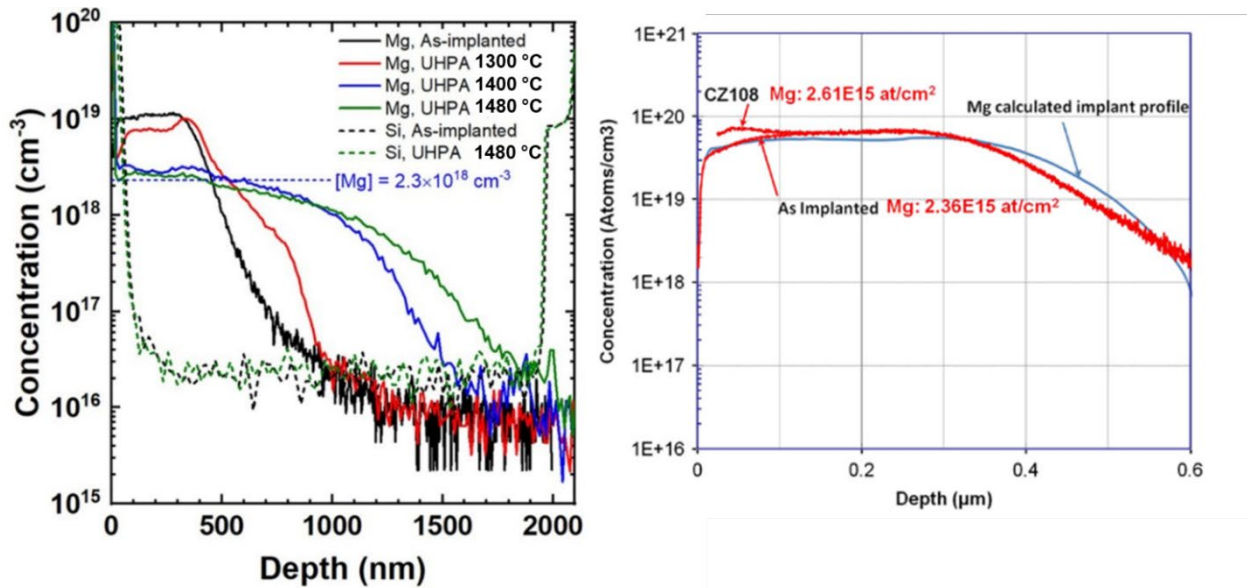


Figure 6-1 SIMS Mg profiles before and after UHPA annealing at temperatures $\geq 1300 \text{ }^\circ\text{C}$ for 5 mins (left)⁴³, and SIMS Mg profiles before and after MRTA annealing at a peak temperature <1400 °C for a total time of 5 mins (right)⁶⁴.

Bibliography

- ¹ ARPA-E PNDIODES Program, <https://arpa-e.energy.gov/technologies/programs/pndiodes>.
- ² W. McMurray and D. P. Shattuck, *IEEE Trans. Commun. Electron.*, **80**, pp. 531–542, (1961).
- ³ P.S. Raderecht, *Int. J. Electronics*, **31**, pp. 541-564, (1971).
- ⁴ S. C. Witzak, R. D. Schrimpf, K. F. Galloway, D. M. Fleetwood, R.L. Pease, J. M. Puhl, D. M. Schmidt, W. E. Combs, and J. S. Suehle, *IEEE Trans. Nucl. Sci.*, **43**, 6, pp. 3151–3160, (1996).
- ⁵ J. D. Plummer and B. W. Scharf, *IEEE Trans. Electron Devices*, **27**, 2, pp. 380–387, (1980).
- ⁶ B. J. Baliga, M. S. Adler, P. V. Gray, R. P. Love, and N. Zommer, *Proc. IEEE Int. Electron Devices Meeting*, pp. 264–267, (1982).
- ⁷ B.J. Baliga, *Advanced Power MOSFET Concepts*. New York, NY, USA:Springer Scientific, (2010).
- ⁸ B.J. Baliga, *IEEE Electron Device Lett.*, **10**, 10, pp. 455–457, (1989).
- ⁹ S.J. Pearton, F. Ren, *Adv. Mater.* **12**, 1571 (2000).
- ¹⁰ R. Sun, J. Lai, W. Chen, and B. Zhang, *IEEE Access* **8**, 15529 (2020).
- ¹¹ T. Mimura, S. Hiyamizu, T. Fujii, and K. Nanbu, *Jpn. J. Appl. Phys.*, **19**, 5, pp. L225–L227, (1980).
- ¹² T. Mimura, *IEEE Trans. Microwave Theory and Techniques*, **50**, 3, pp. 780-782, (2002).
- ¹³ U. K. Mishra, *Proc. IEEE*, **90**, 6, pp. 1022–1031, (2002).
- ¹⁴ N. Zhang, G. Parish, S. Heikman, *IEEE Electron Device Lett.* **21**, 3 (2000).
- ¹⁵ J. Wei, G. Tang, R. Xie, *Jpn. J. Appl. Phys.* **59** (2020).
- ¹⁶ M. Tapajna, S. W. Kaun, M. H. Wong, F. Gao, T. Palacios, U. K. Mishra, J. S. Speck, and M. Kuball, *Appl. Phys. Lett.* **99**, 223501 (2011).

- ¹⁷ S. W. Kaun, M. H. Wong, S. DasGupta, S. Choi, R. Chung, U. K. Mishra, and J. S. Speck, *Appl. Phys. Express* **4**, 024101 (2011).
- ¹⁸ J. A. del Alamo and J. Joh, *Microelectron Reliability*, **49**, 5, pp. 1200–1206, (2009).
- ¹⁹ Y. Won, J. Cho, D. Agonafer, M. Asheghi, and K. E. Goodson, *IEEE Transactions on Components, Packaging and Manufacturing Technology*, **5**, 737 (2015).
- ²⁰ J.C. Gallagher, T.J. Anderson, A.D. Koehler, M.A. Ebrish, G.M. Foster, M.A. Mastro, J.K. Hite, B.P. Gunning, R.J. Kaplar, K.D. Hobart and Francis J. Kub, *Journal of Electronic Materials.*, **50** 3013–3021 (2021).
- ²¹ K. Fujito, S. Kubo, H. Nagaoka, T. Mochizuki, H. Namita, and S. Nagao, *J. Cryst. Growth.*, **311**, 3011 (2009).
- ²² R. Kucharski, T. Sochacki, B. Lucznik, and M. Bockowski, *J. Appl. Phys.*, **128**, 050902 (2020).
- ²³ I. C. Kizilyalli, T. Prunty, O. Aktas, *Electron Device Letters IEEE.*, **36** 10 (2015).
- ²⁴ D. Ehrentraut, E. Meissner and M. Bockowski, “Technology of Gallium Nitride Crystal Growth”, Vol.133 of the Springer Series in Materials Science, pp. 140 (2010).
- ²⁵] R. Dwilinski, R. Doradzinski, J. Garczynski, L.P. Sierzputowski, A. Puchalski, Y. Kanbara, K. Yagi, H. Minakuchi, H. Hayashi, *J. Cryst. Growth*, **310**, 3911 (2008).
- ²⁶ R. Dwilinski, R. Doradzinski, J. Garczynski, L. Sierzputowski, R. Kucharski, M. Zajac, M. Rudzinski, R. Kudrawiec, W. Strupinski, J. Misiewicz, *Phys. Status Solidi (A)*, **208**, pp. 1489–1493 (2011).
- ²⁷ Y. Mikawa, T. Ishinabe, S. Kawabata, T. Mochuzuki, A. Kojima, Y. Kagamitani, H. Fujisawa, *Proc. SPIE*, **9363**, 936302 (2015).

- ²⁸ R.L. Kubena, C.L. Anderson, R.L. Selinger, R.A. Jul-lens and E.H. Stevens, *J. Vat. Sci. Technol.*, **19** (1981).
- ²⁹ D. P. Lecrosnier and G. P. Pelous, *IEEE Trans. Electron Devices*, **21**, pp 113-118, (1974).
- ³⁰ Y. Irokawa, O. Fujishima, T. Kachi, Y. Nakano, *Journal of Applied Physics.*, **97**, 083505 (2005).
- ³¹ A.J. Fellows, Y.K. Yeo, M.-Y. Ryu, R.L. Hengehold, *Journal of Electronic Materials.*, **34** (2005).
- ³² A. Rebey, T. Boufaden, B. El Jani, *J. Crystal Growth* **203** 12 (1999).
- ³³ G, Miceli, and A. Pasquarello, *Phys. Rev. B* **93**, 165207 (2016).
- ³⁴ J. D. Greenlee, T. J. Anderson, B. N. Feigelson, J. K. Hite, and K. M. Bussmann, *Applied Physics Express.*, **7** (12), 121003 (2014).
- ³⁵ J. D. Greenlee, B. N. Feigelson, T. J. Anderson, M. J. Tadjer, J. K. Hite, M. A. Mastro, C. R. Eddy, Jr., K. D. Hobart, and F. J. Kub, *J. Appl. Phys.*, **116**, 063502 (2014).
- ³⁶ J. D. Greenlee, T. J. Anderson, B. N. Feigelson, K. D. Hobart, and F. J. Kub, *Phys. Status Solidi A.*, **212**, 12 (2015).
- ³⁷ T. Niwa, T. Fujii, and T. Oka, *Appl. Phys. Express.*, **10**, 091002 (2017).
- ³⁸ T. J. Anderson, B. N. Feigelson, F. J. Kub, M. J. Tadjer, K. D. Hobart, M. A. Mastro, J. K. Hite, and C. R. Eddy. *Electro. Lett.*, **50**, 3 197 (2014).
- ³⁹ T. J. Anderson, A. D. Koehler, B. Feigelson, K. D. Hobart, and F. J. Kub. *ECS Trans.*, **75**(12), 93 (2016).
- ⁴⁰ T. J. Anderson, J. D. Greenlee, B. N. Feigelson, J. K. Hite, K. D. Hobart, and F. J. Kub. *IEEE Trans. Semi. Manufacturing.*, **29**(4) 343 (2016).

- ⁴¹ M. Kuball, J. M. Hayes, T. Suski, J. Jun, M. Leszczynski, J. Domagala, H. H. Tan, J. S. Williams, and C. Jagadish, *J. Appl. Phys.*, **87**, 2736-2741 (2000).
- ⁴² S. Porowski, I. Grzegory, D. Kolesnikov, W. Lojkowski, V. Jager, W. Jager, V. Bogdanov, T. Suski, and S. Krukowski, *J. Phys.: Condens. Matter*. **14**, 11097 (2002).
- ⁴³ H. Sakurai, M. Omori, S. Yamada, Y. Furukawa, H. Suzuki, T. Narita, K. Kataoka, M. Horita, M. Bockowski, J. Suda, T. Kachi, *Appl. Phys. Lett.* **115**, 142104 (2019).
- ⁴⁴ M.H. Breckenridge, J. Tweedie, P. Reddy, Y. Guan, P. Bagheri, D. Szymanski, S. Mita, K. Sierakowski, M. Bockowski, R. Collazo, and Z.Sitar. *Appl. Phys. Lett.* **118**, 022101 (2021).
- ⁴⁵ T. Oikawa, Y. Saijo, S. Kato, T. Mishima, and T. Nakamura, *Nucl. Instrum. Methods Phys. Res.*, B 365, 168 (2015).
- ⁴⁶ O. Contreras, F. Ponce, J. Christen, A. Dadgar, A. Krost, *Appl. Phys. Lett.*, **81** (2002).
- ⁴⁷ Pezoldt, A. A. Kalnin, D. R. Moskwin, and W. D. Savelyev, *Nucl. Instrum. Methods B*. **80**, 943-948 (1993).
- ⁴⁸ Liliental-Weber, M. Benamara, W. Swider, J. Washburn, I. Grzegory, S. Porowski, D. J. H. Lambert, C. J. Eiting, and R. D. Dupuis, *Appl. Phys. Lett.*, **75**, 4159 (1999).
- ⁴⁹ J.C. Zolper, H.H. Tan, J.S. Williams, J. Zou, D.J.H. Cockayne, S.J. Pearton, M. Hagerott Crawford, R.F. Karlicek, *Appl. Phys. Lett.*, **70**, 2729 (1997).
- ⁵⁰ W. Wesch, A. Heft, J. Heindl, H.P. Strunk, T. Bachmann, E. Glaser, E. Wendler, *Nucl. Instrum. Methods.*, B 106 (1995).
- ⁵¹ S. T. Horng, and M. S. Goorsky. *Appl. Phys. Lett.*, 68(11) 1537 (1996).
- ⁵² S. T. Horng, M. S. Goorsky, J. H. Madok, and N. M. Haegel, *J. Appl. Phys.*, **76**, 42066 (1994).
- ⁵³ T. E. Seidel and A.U. MacRae, *Journal of Radiation Effect*, **7**, (1971).

- ⁵⁴ M. A. Moram, C. F. Johnston, J. L. Hollander, M. J. Kappers, and C. J. Humphreys, *J. Appl. Phys.* **105**, 113501 (2009)
- ⁵⁵ P. Feichtinger, M. S. Goorsky, D. Oster, T. D'Silva, J. Moreland, *J. Electrochem. Soc.* **148**(7), 379-382 (2001).
- ⁵⁶ M. S. Goorsky, P. Feichtinger, H. Fukuto, G. U'Ren, *Philos. Trans. R. Soc., A* **357**, 2777 (1999).
- ⁵⁷ B. D. Poust, T. S. Koga, R. Sandhu, B. Heying, R. Hsing, M. Wojtowicz, A. Khan, and M. S. Goorsky, *J. Phys. D: Appl. Phys.*, **36**, A102 (2003).
- ⁵⁸ M.S. Goorsky, B. Poust, A. Noon, S. Hayashi, and R. Ho, Proceedings of the IEEE of the 16th International Conference on Indium Phosphide and Related Materials (2004).
- ⁵⁹ C. Hetherington *Mater Today*, **7** (2004).
- ⁶⁰ F. Ziegler, J. P. Biersacke, and U. Littmark, *The Stopping and Range of Ions in Solids*, vol 1 (Oxford, Pergamon), (1985).
- ⁶¹ A. Sakai, H. Sunakawa, A. Usui, *Appl. Phys. Lett.*, **71**, 2259 (1997).
- ⁶² I. Gutierrez-Urrutia, D. Raabe, *Scripta Mat.*, **66**, 12 (2012).
- ⁶³ Y. Kim, J. Jeong, J. Kim, Y. Kim, *J. Korean Phys. Soc.* **48**, 2 (2006).
- ⁶⁴ B.N. Feigelson, T.J. Anderson, M. Abraham, J.A. Freitas Jr, J.K. Hite, C.R. Eddy Jr, F.J. Kub, *J. Cryst. Growth*, **350**, 1, 21-26 (2012).
- ⁶⁵ Y. Wang, T. Bai, C. Li, M. Tadjer, T. Anderson, J. Hite, M. Mastro, C. Eddy, K. Hobart, B. Feigelson, M. Goorsky, *ECS JSST*, **8**(2), 70-76 (2019).
- ⁶⁶ D. Pribat, D. Dieumegard, M. Croset, C. Cohen, R. Nipoti, J. Siejka, G. G. Bentini, L. Corraera and M. Servidori, *Nucl. Instr. and Meth.* **209**, 737-742 (1983).

- ⁶⁷ S. Hayashi, M.S. Goorsky, A. Noori, and D. Bruno, *J. Electrochem. Soc.*, **153**(12), 1011-1014 (2006).
- ⁶⁸ C. Liu, B. Mensching, K. Volz, B. Rauschenbach. *Appl. Phys. Lett.* **1997**, *71*, 3448.
- ⁶⁹ RADS Software, Bruker Semiconductor, info.semi@bruker.com.
- ⁷⁰ M. Akazawa and K. Uetake, *Jpn. J. Appl. Phys.*, **58**, SCCB10 (2019).
- ⁷¹ C. Miclaus and M. S. Goorsky, *J. Phys. D: Appl. Phys.*, **36**, 177-180 (2003).
- ⁷² M. Meshkinpour, M. S. Goorsky, B. Jenichen, D. C. Streit, T. R. Block, *J. Appl. Phys.*, **81**, 3124–3128 (1997).
- ⁷³ J. Guo, Y. Yang, B. Raghothamachar, M. Dudley, and S. Stoupin. *J. Electron. Mater.*, **47**(2) 903-909 (2018).
- ⁷⁴ S. Leclerc, B. Lacroix, A. Declémy, K. Lorenz, and P. Ruterana. *J. Appl. Phys.* **112**, 073525 (2012).
- ⁷⁵ F. Gloux, P. Ruterana, T. Wojtowicz, K. Lorenz, E. Alves. *Superlattices and Microstructures*, **40**, 300–305 (2006).
- ⁷⁶ A. Turos, *Radiation Effects and Defects in Solids*, **2013**, 168, 6, pp. 431-441.
- ⁷⁷ C.M. Wang, W. Jiang, W.J. Weber, L.E. Thomas, *J. Mater. Res.* **2002**, *17*, 11, pp. 2945-2952.
- ⁷⁸ J. Pezoldt, A. A. Kalnin, D. R. Moskwina, and W. D. Savelyev, *Nucl. Instrum. Methods B.* **80**, 943-948 (1993).
- ⁷⁹ Y.G. Morozov, O.V. Belousova, M.V. Kuznetsov, D.Ortegabc, I. P. Parkind. *J. Mater. Chem.* **22**, 11214-11223, (2012).
- ⁸⁰ J. Wong-Leung, M. Janson, A. Kuznetsov, B. Svensson, M. Linnarsson, A. Hallen, C. Jagadish, and D. Cockayne, *Nucl. Instrum. Meth B.*, **266**(8), 1367-1372 (2008).

- ⁸¹ T. Yoshiie, H. Iwanaga, N. Shibata, K. Suzuki, and S. Takeuchi, *Philos. Mag A.* **41**(6), 935-942 (1980).
- ⁸² G. Perillat-Merceroz, P. Gergaud, P. Marotel, S. Brochen, P.-H. Jouneau, and G. Feuillet, *J. Appl. Phys.* **109**, 023513 (2011).
- ⁸³ Y. Wang, K. Huynh, M. E. Liao, H.-M. Yu, T. Bai, J. Tweedie, M. H. Breckenridge, R. Collazo, Z. Sitar, M. Bockowski, Y. Liu, and M. S. Goorsky, *Phys. Status Solidi B.*, **257**, 1900705 (2020).
- ⁸⁴ M. E. Liao, Y. Wang, T. Bai, and M. S. Goorsky, *ECS J. Solid State Sci. Technol.* **8**, 673 (2019).
- ⁸⁵ Y. Wang, M.E. Liao, K. Huynh, A.A. Allerman, M.S. Goorsky, *ECS J. Solid State Sci. Technol.* **10**(4), 045010 (2021).
- ⁸⁶ M.E. Liao, K. Huynh, Y. Wang, A.A. Allerman, M.S. Goorsky, *ECS trans*, **98**, 6 (2020).
- ⁸⁷ J. Wen, D. J. Miller, W. Chen, T. Xu, L. Yu, S. B. Darling and N. J. Zaluzec, *Microsc. Microanal.*, **20**, 1507 (2014).
- ⁸⁸ S. Hayashi, D. Bruno, and M. S. Goorsky, *Appl. Phys. Lett.*, **85**, 236 (2004).
- ⁸⁹ S. Suihkonen, S. Pimputkar, S. Sintonen, and F. Tuomisto, *Adv. Electron. Mater.* **3**, 1600496 (2017)
- ⁹⁰ P. Vennéguès, M. Benaissa, B. Beaumont, E. Feltin, P. De Mierry, S. Dalmaso, M. Leroux, and P. Gibart, *Appl. Phys. Lett.* **77**, 880 (2000).
- ⁹¹ P. Vennéguès, M. Leroux, S. Dalmaso, M. Benaissa, P. De Mierry, P. Lorenzini, B. Damilano, B. Beaumont, J. Massies, and P. Gibart, *Phys. Rev. B* **68**, 235214 (2003).
- ⁹² K. Iwata, T. Narita, M. Nagao, K. Tomita, K. Kataoka, T. Kachi, and N. Ikarashi, *Appl. Phys. Express* **12**, 031004 (2019).

⁹³ A. Kumar, K. Mitsuishi, T. Hara, K. Kimoto, Y. Irokawa, T. Nabatame, S. Takashima, K. Ueno, M. Edo, and Y. Koide, *Nanoscale Res. Lett.* 13, 403 (2018)

⁹⁴ T. Remmele, M. Albrecht, K. Irscher, R. Fornari, and M. Straßburg, *Appl. Phys. Lett.* 99, 141913 (2011).

⁹⁵ B. P. Gunning, C. A. M. Fabien, J. J. Merola, E. A. Clinton, W. A. Doolittle, S. Wang, A. M. Fischer, and F. A. Ponce, *J. Appl. Phys.* 117, 045710 (2015).

⁹⁶ A. Kumar, J. Uzuhashi, T. Ohkubo, R. Tanaka, S. Takashima, M. Edo, and K. Hono, *J. Appl. Phys.* 126, 235704 (2019).

⁹⁷ Iwata, H. Sakurai, S. Arai, T. Nakashima, T. Narita, K. Kataoka, M. Bockowski, M. Nagao, J. Suda, T. Kachi, and N. Ikarashi, *J. Appl. Phys.* 127, 105106 (2020)